Virtual Screening and Binding Free Energy Calculations of Sirtuin Inhibitors

Dissertation

zur Erlangung des akademischen Grades

Doctor rerum naturalium (Dr. rer. nat.)

vorgelegt der

Naturwissenschaftlichen Fakultät I

Biowissenschaften

der Martin-Luther-Universität Halle-Wittenberg

von Urszula Sylwia Uciechowska

geb. 12. Oktober 1981 in Kielce, Polen

Gutachter /in:

1. Prof. Dr. Wolfgang Sippl, Halle (Saale)

2. Prof. Dr. Gerhard Wolber, Berlin

3. Prof. Dr. Manfred Jung, Freiburg

Halle (Saale), den 13. Dezember 2010 (Tag der Verteidigung)

Acknowledgements

The present work was carried out at the Institute of Pharmaceutical Chemistry of Martin-Luther-University Halle-Wittenberg from 2006 to 2010. First, I would like to thank to my supervisor Prof. Dr. Wolfgang Sippl for giving me the opportunity to complete this research. His guidance and suggestions throughout the duration of my research and dissertation were invaluable.

I would also like to thank Ralf, Sonja, Marc, Kanin and all other members of the Medicinal Chemistry for creating a good working atmosphere and helpful discussions. Rene and German also helped me numerous times with computer-related problems.

I would like to thank to our collaborators Prof. Manfred Jung and his group from University of Freiburg. The biological data from his group were an integral component of my research.

I would like to thank Michael Lawson for his corrections and comments on the dissertation, and making it easier to understand.

I also appreciate the numerous contributions of my family and Krzysztof to this work, in both personal and financial support. Without you many things would not have been possible.

Finally, I offer my regards to all of those who supported me in any way during these years.

Table of Contents

iii

Chapter 1

Introduction

1.1 Epigenetic Regulation

In 1942, Conrad Waddington defined epigenetics "as a branch of biology which studies the casual interactions between genes and their products, which bring the phenotype into being" [1]. Today, epigenetics is the study of heritable changes in gene expression that occur without changes to the DNA sequence [2]. Genetic information is strictly regulated and organized such that it is possible to modify a cells phenotype without changing its genotype [3]. This process is in part controlled by epigenetic mechanisms, which modify gene functions without changing the nucleotide sequence of the gene. There are many implications for epigenetic research in important biological processes such as gene expression and silencing, apoptosis, aging and cancer [4].

Three classes of epigenetic modifications can affect gene expression. In DNA methylation, methyl groups are added and removed from DNA by DNA methyltransferases (DNMTs). Another modification involves microRNAs, which influence expression through interaction with mRNA [5]. Histone modifications influence chromatin structure though acetylation and methylation of N-terminal lysine residues.

Both the scientific and medicinal communities recognize the importance of epigenetic changes in cancer. It is known that epigenetic mechanisms are a critical component of carcinogenesis, and thus the study of epigenetics will contribute to the development of more effective tools for cancer diagnosis and treatment. Some evidence suggests that DNA methylation may result from adverse exposures to epimutagens [6]. Environmental factors have also been shown to influence histone modifications that subsequently could contribute to the development of human cancer [7].

1.2 Chromatin, DNA and Histones

Chromosomes are comprised of chromatin, which is a complex of DNA, RNA and proteins that provides a physical barrier to transcription. The functional unit of chromatin is the nucleosome, in which 146bp of DNA are wrapped around a histone core [8, 9] (Figure 1).
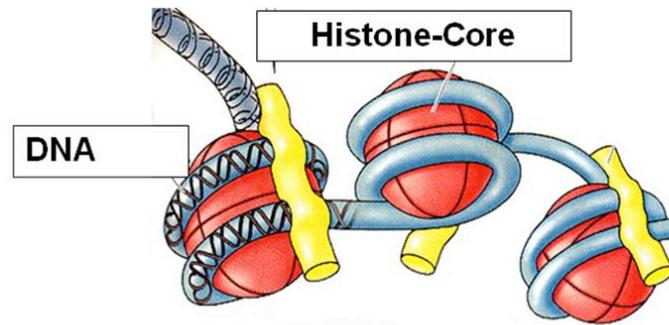
Figure 1: DNA wrapped around histone proteins, forming an organized structure called chromatin, which is folded to form the chromosomes (adapted from [10]).

Chromatin has a well-established repressive effect on the biochemistry of DNA, since it restricts access of enzymatic and regulatory complexes to DNA. In the case of heterochromatin, which is the more compact form of chromatin, transcription factors are unable to bind to DNA. Not surprisingly, the formation of heterochromatin is therefore correlated to the repression of gene transcription and arresting of cell division. Euchromatin is the more lightly packed form of chromatin, and is often under active transcription.

Histones are basic proteins that are rich in lysines and arginines and are highly conserved across eukaryotes. The histone tails sticks out from the nucleosome structure and can be modified through acetylation, methylation, phosphorylation, ubiquitination and sumoylation [11-12]. Small chemical compounds like methyl or acetyl groups can be covalently linked to lysines or arginines. These amino acids serve as interaction sites for other proteins that can recognize the histones and enable them to pack or unwrap. The modification of histones during cell division has also been shown to be integral to the process of differentiation [13].

1.3 Histone Modifications

The ability of epigenetic modifications to influence transcription and translation signifies these biological processes as potential drug targets. Additionally, epigenetic enzymes directly affect the activity of important proteins, such as the inactivation of the tumor suppressor p53 through deacetylation by human SIRT2 [14, 15-17]. Another modification is the

posttranslational cleavage of acetyl groups from ε-amino groups of lysine residues in histone tails by histone deacetylases (HDACs), which results in a free amino group in the lysine side chain. With opposing activity, histone acetyltransferases (HATs) transfer an acetyl moiety to lysine residues of histones (Figure 2) and ensure a balance between acetylation and deacetylation of chromatin. Acetylation of histones has been mostly correlated with an activation of gene expression, but repression has also been observed [18].
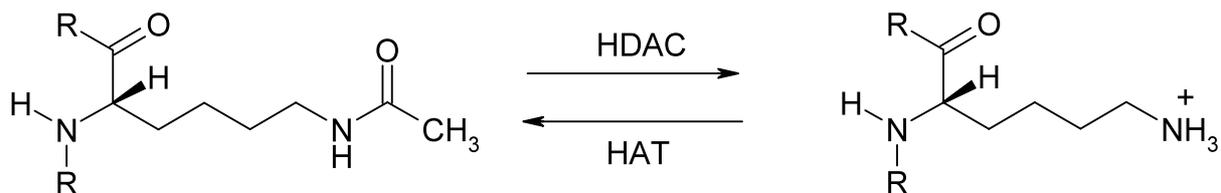
Figure 2: Histone acetylation and deacetylation.

1.4 Histone Deacetylases (HDACs) Class I, II and IV

Eighteen members of the HDAC protein family have been identified and classified based on their homology to yeast histone deacetylases [19]. Class I, II and IV represent the "classical" histone deacetylase operating by Zn^{2+} dependent mechanism. These proteins play crucial roles in the regulation of cellular metabolism, and are interesting drug targets for treatment of wide range of human diseases [20].

1.5 Histone Deacetylases - Class III Sirtuins

The nucleolar *S. cerevisiae* protein Sir2p was the first sirtuin protein found, and was shown to interact with histones and effect transcriptional silencing at telomeres [21-24]. The corresponding gene of MAR1 (for mating type regulator1) was discovered through random mutagenesis by Klar and colleagues [22] to cause sterility by relieving silencing at the mating-type loci HMR and HML. Random mutagenesis by Jasper Rine's group led to the discovery of three more genes with the sterile phenotype, and replaced the MAR nomenclature with *SIR* (*Silent Information Regulator*) [22].

Gottlieb and Esposito [25] demonstrated that SIR2 is the only SIR gene required to suppress recombination of ribosomal RNA. Gottschling and colleagues [26] found SIR2 to be a part of mechanism that silences genes near telomeres. Brachman [20] and Derbyshire [21] discovered four additional *S. cerevisiae* genes with high homology to SIR2 and named them HST (homologues of SIR2). HST genes were found to be involved in silencing at the mating-type loci and telomeres as well as cell-cycle progression and genomic integrity.

SIR2 homologues were found in organisms ranging from bacteria to plants and mammals, suggesting that SIR2 is a member of a large family called 'sirtuins'. The modern sirtuin family consist of seven members SIRT1-7, and mammalian sirtuins differ in their sub-cellular localization. SIRT1, SIRT6 and SIRT7 are predominately in the nucleus. SIRT1 is largely associated with euchromatin, whereas SIRT6 associates with heterochromatin [27, 28]. SIRT2 is located in the cytoplasm [29, 30], and SIRT3, SIRT4 and SIRT5 are localized to the mitochondria. With regard to activity, SIRT2 and SIRT3 have both deacetylase and mono-ADP-ribosyl transferase [29-32], whereas SIRT6 and SIRT4 are only mono-ADP-ribosyl transferase [31, 32].

1.5.1 Sirtuins Functions

Sirtuins are active on a wide variety of substrates and have been linked to a broad spectrum of cellular functions (Table 1). SIRT1 has been found to interact with several tumor suppressor proteins e.g (p53, Rb) and oncoproteins (BCL6), and regulates glucose homeostasis and aging [33, 34]. SIRT1 deacetylation of the DNA repair enzyme Ku70 upregulates DNA repair, and SIRT1 deacetylation of tumor suppressor protein p53 [35-39] enables apoptosis to occur in response to genotoxic stress. SIRT2 co-localizes with the microtubule network and deacetylates Lys40 of α-tubulin, which is a critical regulator of cell cycle progression [29]. The mammalian SIRT2 seems to suppress gliomas which are a type of brain tumor [28]. Not surprisingly, SIRT1 activators such as Reservatrol have shown usefulness as cancer therapeutics [40]. SIRT1 has also been linked to protection against Alzheimer's diseases (AD) in mouse models of (AD), likely by affecting pathways involving deacetylation of p53 and PGC-1α [41-45]. Although the role of the mammalian SIRT2 in lifespan expansion has not yet been determined, the orthologs of SIRT2 has been linked to lifespan extension through caloric restriction in *C.elegans, S. Cerevisiae,* and *D.melanogaster* [46-48]. SIRT2 has been shown to be up regulated in diabetic myocytes [49, 50]. SIRT2 was recently demonstrated as an inhibitor of oligodendroglial differentiation of the microtubule cytoskeleton [28]. Some of the effects of SIRT2 appear to be detrimental to neuronal health, *e.g.* SIRT2 may oppose resistance to axonal degeneration [51]. Outerio *et.al* [52] reported that small molecule inhibitiors of SIRT2 may provide therapeutic intervention in Parkinson's diseases (PD). The sirtuin inhibitor nicotinamide protects neurons against onoxic injury [53], and HDAC inhibitors have been shown to exhibit neuroprotective effects [54- 56].

Human SIRT3 is primarily located in the mitochondrial matrix [57, 58], and shows robust histone deacetylase activity on the histone H4 peptide *in vitro*. The absence of histones in mitochondria suggests that SIRT3 is active on non-histone targets [58]. SIRT7 expression levels were found to increase significantly in breast cancer, and SIRT7 and SIRT3 are both highly transcribed in lymph-node breast biopsies [59-62].

Table 1. Summary of known sirtuin enzymatic activities substrates and their biological functions [37] for SIRT1 [38-43], SIRT2 [43-45, 63], SIRT3 [53, 59, 64-66], SIRT4 [48, 32], SIRT5 [37], SIRT6 [61], and SIRT7 [51, 52, 62].

Sirtuin Human	Activity	Cellular localization	Targets	Biological Functions
SIRT1	deacetylase ADP-ribosyltransferase	nuclear	AceCS1,Atg5,Atg7,Atg8 BCL6, FOXO1 histone H3, (K9,K14) Ku70,LXR,MEF2 MyoD, p300, p53 p73, PCAF, Rb TAF$_1$68	metabolism regulation glucose homeostasis neuroprotection cardioprotection anti/pro cancer HIV transcription aging, cell survival
SIRT2	deacetylase ADP-ribosyltransferase	cytoplasmic	α- tubulin histone H3 histone H4 p53	miotic exit from cell cycle tumor suppression myelinogenesis regulation of cellular stress
SIRT3	deacetylase ADP-ribosyltransferase	mitochondrial	AceCS2 GDH histone H4	LYS deacetylation NAD$^+$(salvage) apoptosis, thermogenesis aging/cell survival
SIRT4	ADP-ribosyltransferase	mitochondrial	GDH BSA	regulation of insuline secretion NAD$^+$(salvage)
SIRT5	deacetylase	mitochondrial	cytochrome c, histone H4 p53	unknown aging
SIRT6	deacetylase ADP-ribosyltransferase	nuclear	histone H3	regulation of metabolism cell survival/aging telomere maintance
SIRT7	deacetylase	nuclear	p53	RNA polymerase I activation

				cell survival/aging

1.5.2 Overall Structure of Sirtuins

In contrast to the zinc-dependent deacetylation mechanism of class I, II and IV HDACs, sirtuins (class III HDACs) depend on NAD^+ to carry out catalytic reactions [67]. All published sirtuin structures contain a conserved 270 amino acid catalytic domain with variable N- and C-termini. Crystal structures for human SIRT2, SIRT3 and SIRT5 have also been solved (Figure 3), and possess a small zinc-binding domain and a large Rossmann fold that is characteristic of NAD-binding proteins. The two domains form a cleft in the middle where NAD^+ and the acetylated (Ac) peptides bind. Crystal structures for several bacterial Sir2 proteins were also resolved whereas no 3D structure is available for Sirt1 [51].
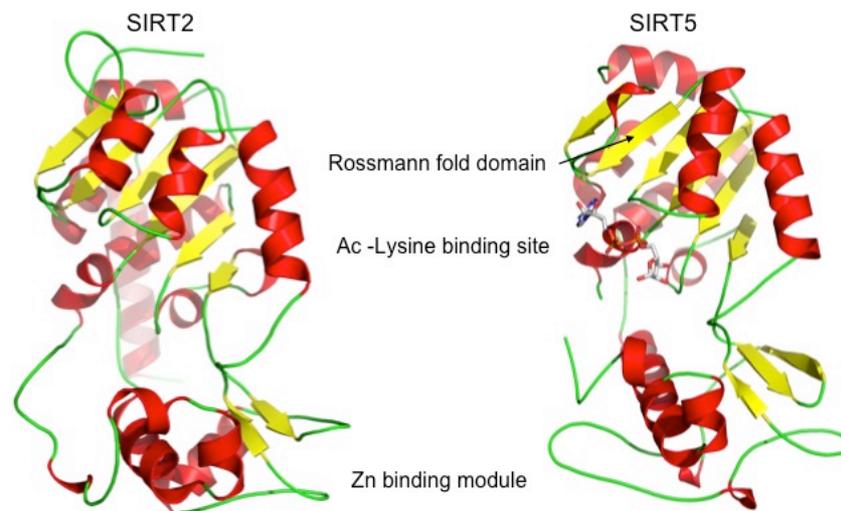
Figure 3: Crystal structure of the human sirtuins SIRT2 (pdb code 1J8F) and SIRT5 (pdb code 2B4Y). The secondary structure elements are colour coded: red = a-helices, yellow = b-strands, blue = turns, green = loop regions).

The only sirtuin X-ray structure that contains complete NAD^+ is the archaebacterial Sir2-Af1 (Figure 4A). The NAD^+ binds in a region at the interface of the larger and smaller domain [51]. Based on the X-ray structure it is possible to distinguish different regions of NAD^+ binding. The X-ray structure of *Archaeoglobus fulgidus* Sir2-Af2 was found by Wolberger *et al.* [68], and was resolved as a complex with an acetylated peptide from p53 (Figure 4 B). The p53 peptide is situated between the Rossmann-fold and the zinc-binding domain. As shown in Figure 4 B, the peptide interacts with two regions of Sir2-Af2 known as β-stable domain. The

acetyl-lysine was found to adopt an extended conformation that allows it to insert into a cleft and point toward the location of the cofactor [55]. It is suggested that the NAD$^+$ and substrate binding process shows a cooperative effect [51].
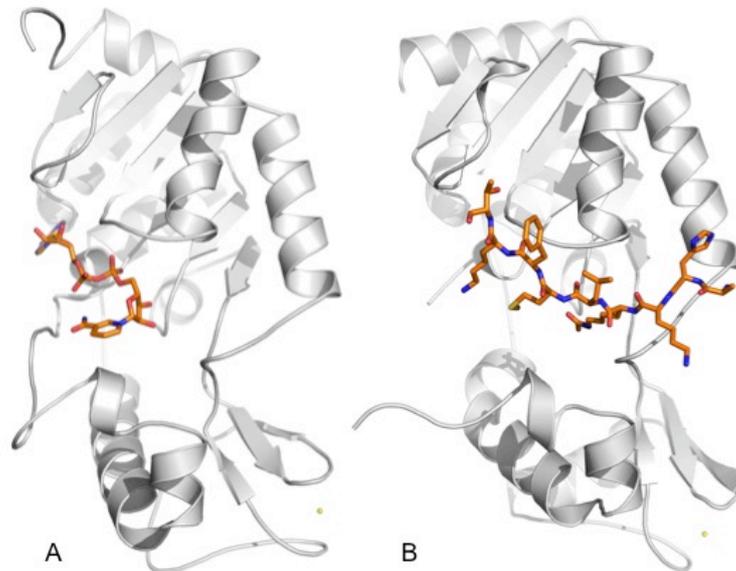
Figure 4: Crystal structures of, A Sir2-Af1 (pdb code 1ICI) in complex with NAD$^+$ in orange, B Sir2-Af2 (pdb code 1MA3) in complex with an acetylated p53 peptide, the Zinc $^{2+}$ atom is coloured in yellow.

1.5.3 The NAD$^+$ Binding Pocket

The NAD$^+$ binding pocket can be divided into three distinct regions A, B and C. This division is based on the interaction of adenine (A), ribose (B) and nicotinamide (C) which are parts of the cofactor (Figure 5). Whereas the interaction of adenine and ribose is similar in all available Sirtuin X-ray structures, the interaction of the nicotinamide part is less clearly defined. Several, so called productive and non-productive conformations of nicotinamide have been observed in crystal structures, reflecting the high flexibility of this part of the cofactor. In the X-ray structure of a SIRT2 homologue from Archeabacteria it was shown that the acetylated peptide binds in a cleft between the two domains [69]. The acetyl-lysine residue inserts into conserved hydrophobic pocket, where NAD$^+$ binds nearby. In case of the human SIRT2 X-ray structure, no structural information about the NAD$^+$ or substrate binding is available. However, due to the homology with bacterial Sirtuins, docking studies showed that NAD$^+$ interact in a comparable way with human and bacterial enzyme [70]. The B and C sites are thought to be directly involved in catalysis. In the presence of acetyl-lysine, NAD$^+$ bound to the B site, bringing the C nicotinamide group in proximity to the C site, where it can

be cleaved [70]. The ADP-ribose product of this reaction may then return to B site, where deacetylation of acetyl-lysine takes place. The organization of the NAD^+ binding site might explain how nicotinamide inhibits sirtuin activity. Thus, at high concentration, free nicotinamide may occupy the C subpocket and block the conformational change of NAD^+ [68].
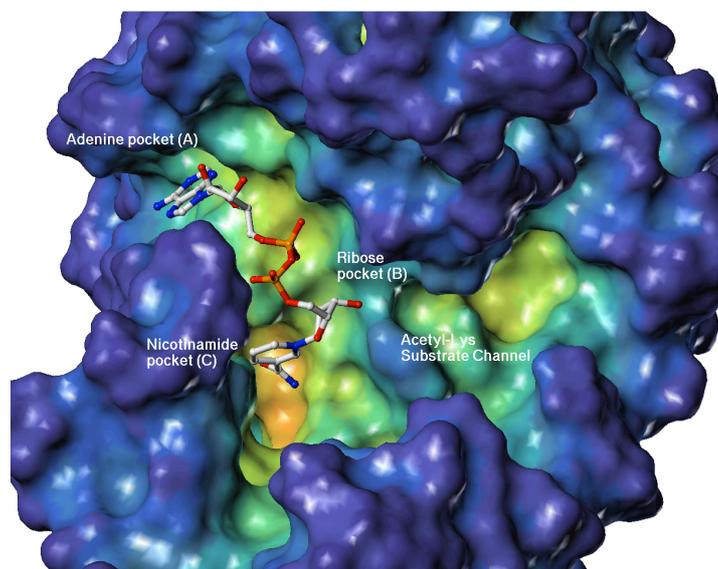
Figure 5: Interaction of NAD^+ in sirtuins binding pocket predicted by docking studies. The molecular surface of the protein is coloured according to the cavity depth.

1.5.4 Catalytic Mechanism of Sirtuins

Several mechanisms by which Sir2 proteins catalyze the NAD^+ have been proposed [63, 71-74]. However, it is still unclear if the initial step, cleavage of nicotinamide from NAD^+ is caused via S_N1 or S_N2 type mechanism (Figure 6). S_N1 type mechanism resulting in an oxocarbenium intermediate II which is attacked by the acetyl-lysine leads to the O-alkylamidate I. Similar in an S_N2 reaction the acetyl carbonyl oxygen directly attacks C1´ of nicotinamide ribose, forming nicotinamide and the O-alkylamidate species II. Recent evidence strongly supports the S_N2 pathway [40]. The next step is the activation of the 2'-hydroxyl of the O-alkylamidate I by a histidine residue in the active site. An intramolecular nucleophilic attack of the O-alkylamidate leads to a 1´, 2´-cyclic intermediate III. Finally, a water molecule leads to formation of the deacetylated peptide and 2´-OAADPR. An intramolecular trans-esterification of 2´-OAADPR results in a mixture of 2´- and 3´-OAADPR. OAADPR was reported as NAD^+-competitive inhibitor for yeast Sir2 with a K_i of

177 μM. The other product of the deacetylation step nicotinamide was reported to be the physiological inhibitor of sirtuins [75, 76].
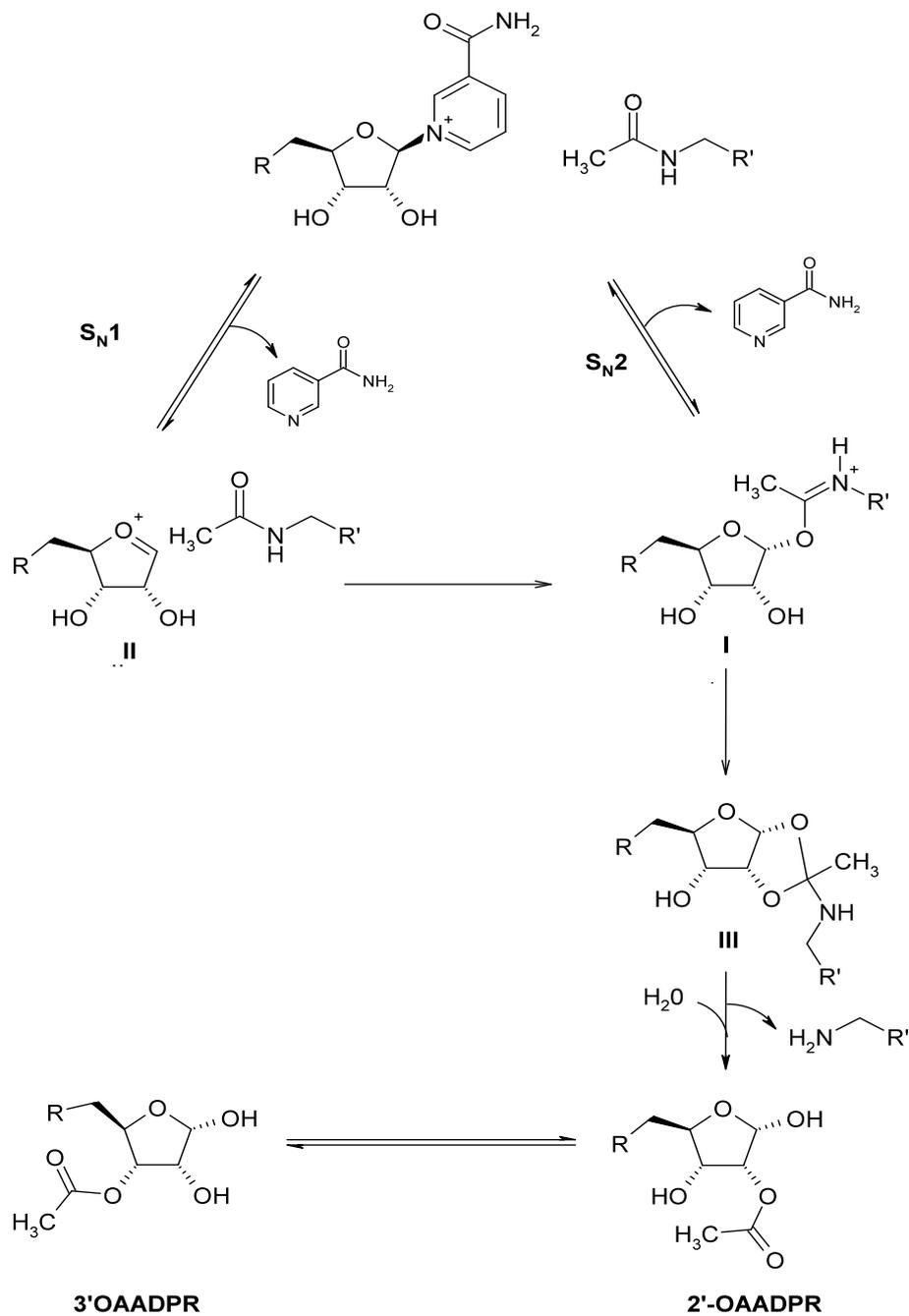
Figure 6: Proposed steps involved in the Sirt2 reaction mechanism [77].

1.6 Sirtuin Inhibitors

Several classes of sirtuin inhibitors have been described over the past few years, such as NAD^+ derivatives (e.g. nicotinamide, carba-NAD^+, NADH), coumarins and related derivatives (splitomicins, HR73) 2-hyroxynaphthaldehyde derivatives (e.g. sirtinol, para-sirtinol, M15, cambinol) [78, 79], tricyclic derivatives, and indole derivatives [80]. Recently, several adenosine mimetics were identified as sirtuins inhibitors [81]. Selective and potent inhibitors are needed to understand the role of these enzymes in biological processes, and several of these compounds are in preclinical evaluation as potential drug candidates.

1.6.1 NAD^+ Derivatives

Nicotinamide is a vitamin B_3 derivative and is an essential nutrient. It is a physiological inhibitor of sirtuins, and inhibits SIRT1 and SIRT2 with IC_{50} values of 50-100μM. Some studies reported that nicotinamide is an allosteric noncompetitive inhibitor [82] interacting with the subpocket C of sirtuins. The direct backward reaction of nicotinamide with the O-alkylamidate intermediate to NAD^+ is discussed as a reason for sirtuin inhibition [83]. The nicotinamide analog 2-anilinobezamide was identified as an SIRT1 inhibitor in library screening by Suzuki *et al.* with an IC_{50} value of 17μM [84] (Figure 7).

Carba-NAD^+ is an inhibitor of NAD^+ dependent histone deacetylases, which compete for coenzyme binding in the active site. This compound consists of NAD^+ with a carbon instead of an oxygen atom in the nicotinamide nucleotide part. Structures related to carba-NAD^+ have been found to inhibit other NAD^+-dependent enzymes, indicating that NAD^+ analogues seem to be suitable for further development of small sirtuin inhibitors [83, 71].
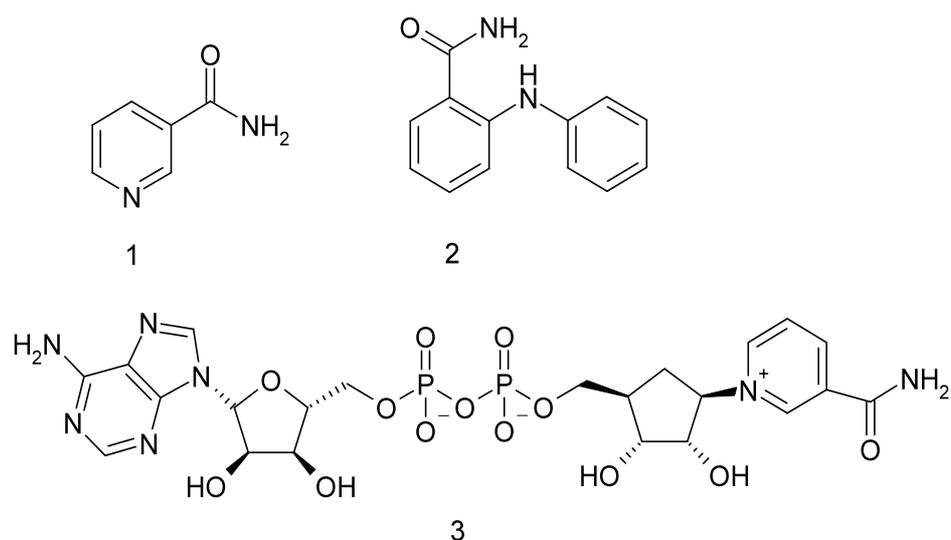
Figure 7: Molecular structure of **(1)** Nicotinamide, **(2)** 2-anilinobenzamide, **(3)** carba-NAD$^+$.

1.6.2 Coumarin Derivatives

Bedalov *et.al* identified splitomicin (4) (Figure 8) through cell-based screening in *S.cerevisae* as inhibitors of Sir2p and HST1 [85]. Mutational studies of the domain near the peptide binding site suggest that splitomicin inhibits sirtuins by hindering access of the acetylated lysine peptide to Sir2. The activity of splitomicins is limited by hydrolysis of the unstable lactone ring, which decreases the potency of the inhibitor. Through the study of 100 splitomicin derivatives, Hiaro *et.al* found several selective SIRT1 and HST1 inhibitors. One such inhibitor is HR73 (5), a bromo-substituted splitiomicin, inhibited SIRT1 *in vitro* with an IC$_{50}$ value of 5μM [86].
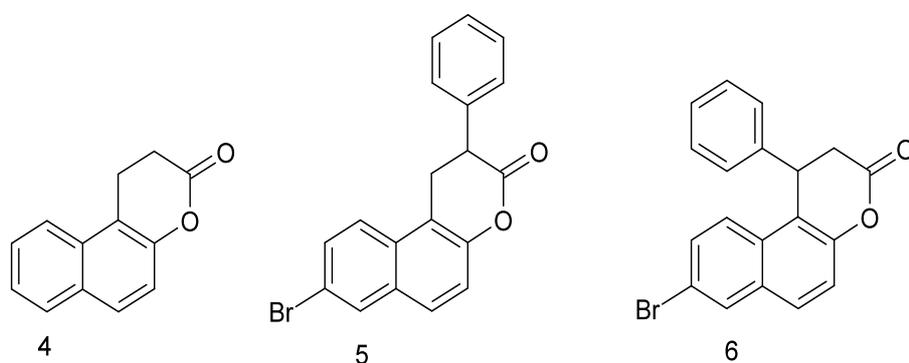
Figure 8: Molecular structure of **(4)** splitomicin, **(5)** HR73, and **(6)** β-aryl splitomicin.

1.6.3 Hyroxynaphthaldehyde Derivatives

Random screening to of 1600-compounds by Grozinger *et al.* led to the identification of Sirtinol, which inhibited Sir2p with an IC_{50} value of 68 μM and SIRT2 at 38μM *in vitro* [86]. Mai *et al.* published a set of Sirtinol analogues [87], and discovered *p*-Sirtinol to be a more potent SIRT1 and SIRT2 inhibitor than Sirtinol (Figure 9). Additionally, Sirtinol was found to as a prodrug in cell cultures through the release of naphthoic acid [87].

Cambinol, was discovered through random screening, was found to inhibit SIRT1 and SIRT2 with IC_{50} values of 56 μM and 59 μM and was inactive on SIRT3 and SIRT5 [88]. The compound displayed anticancer activity in an animal model, and a competition experiment with NAD^+ and histone H4 peptide showed the compound to be competitive with the peptide substrate. Heltweg *et.al* found evidence of cellular activity through observation of cambinol-mediated hyperacetylation of p53, α-tubulin, Ku70 and FOXO3a [89]. An analogue of Cambinol without the β-naphtol group was not able to inhibit sirtuins *in vitro* and did not lead to apoptosis in lymphoma cells.
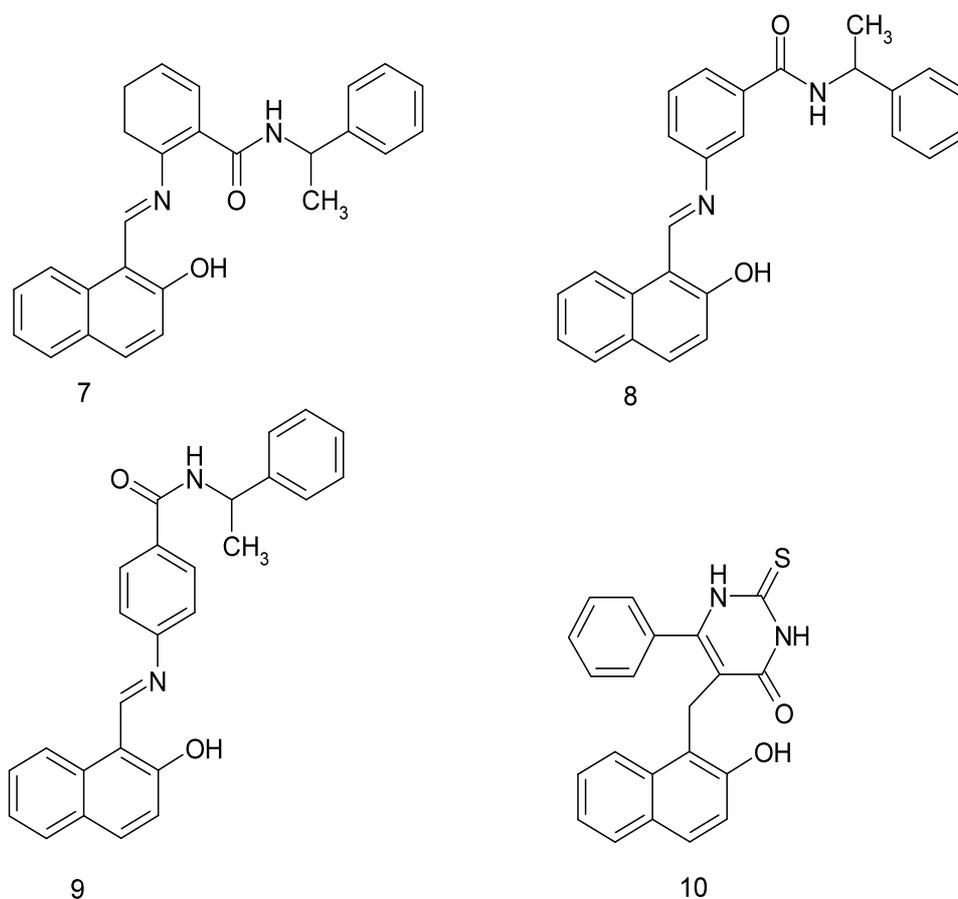
Figure 9: Molecular structure of **(7)** Sirtinol, **(8)** meta-Sirtinol, **(9)** para-Sirtinol, **(10)** cambinol.

1.6.4 Indole Derivatives

High-throughput screening by Napper *et al.* identified Indole derivatives as sirtuin inhibitors with an IC_{50} value of 100 nM for SIRT1, and selectivity over SIRT2 (IC_{50} 19,6 μM) and SIRT3 (IC_{50} 48,7 μM) [90]. Class I, II HADACs were not inhibited by Indole at a concentration of 100 μM. The most potent derivative (EX-527, Figure 10) was shown to penetrate cells and inhibit deacetylation of p53 at a concentration of 1 μM [91].

Figure 10: Molecular structure of **(11)** Indole 35, **(12)** EX-527.

1.6.5 Suramin

Suramin is a symmetric polyanionic naphthylurea derivative (Figure 11) that was originally used for the treatment of trypanosomiasis [92]. It shows a wide range of biological activities such as antiproliferative and antiviral activity. Trapp *et al.* observed that Suramin inhibits SIRT1 [93]. Suramin exhibited an IC_{50} value of 297 nM against SIRT1 and 1150 nM against SIRT2 [94]. A SAR study of suramin found the suramin core structure (NF675) showed IC_{50} of 93 nM, and modification of the benzoyl portion of suramin slightly increased the inhibitory potency. Theoretical studies using X-ray structure of suramin cocrystallized with human SIRT5 and docked into a SIRT2 model suggest that the binding pocket for suramin is localized between the nicotinamide binding site and peptide substrate-binding region [94]. This observation is in agreement with the results obtained by a competition analysis, in which suramin was found to be a noncompetitive inhibitor with respect to both NAD^+ and the peptide substrate. Suramin derivatives are useful tools for the development of novel sirtuin inhibitors, although the therapeutic application of suramin may be problematic due to the high polarity.

13

14

Figure 11: Molecular structure of **(13)** Suramin, and **(14)** NF-675.

1.7 Sirtuin Activators

The first sirtuin activator was reported by Sinclair *et al.* [95, 96]. The phytoalexin Reservatrol (3, 4, 5- dihydroxystilbene, Figure12) and several similar plant derivatives were identified using an *in vitro* assay and fluorescent tags [97]. Commonly found in red wine, Reservatrol has an enzyme activity by ($EC_{1.5}$) of 46 μM with a 200% maximum activation in SIRT1 enzymatic assay [40, 96]. Reservatrol treatment extended the lifespan of yeast cells, worms, fruits flies and vertebrate fish. Further investigations for small molecule activators gave a number of non-polyphenolic compounds as SIRT1 activators. Nayagama *et.al* reported treatment with pyrroloquinoxalines showed 2-fold activation of SIRT1 at 10 μM (Figure 12) [97]. Milne *et al.* found a series of imidazothiazoles as selective SIRT1 activators which also

showed activity in a cell-based SIRT1 deacetylation activity assay. Sirtuin activators appear to be promising for the treatment of human diseases such as diabetes type 2 [78], Huntington's disease [96], Alzheimer's disease [95], inflammation [79], and cancer [98], but are still in early stages of development.
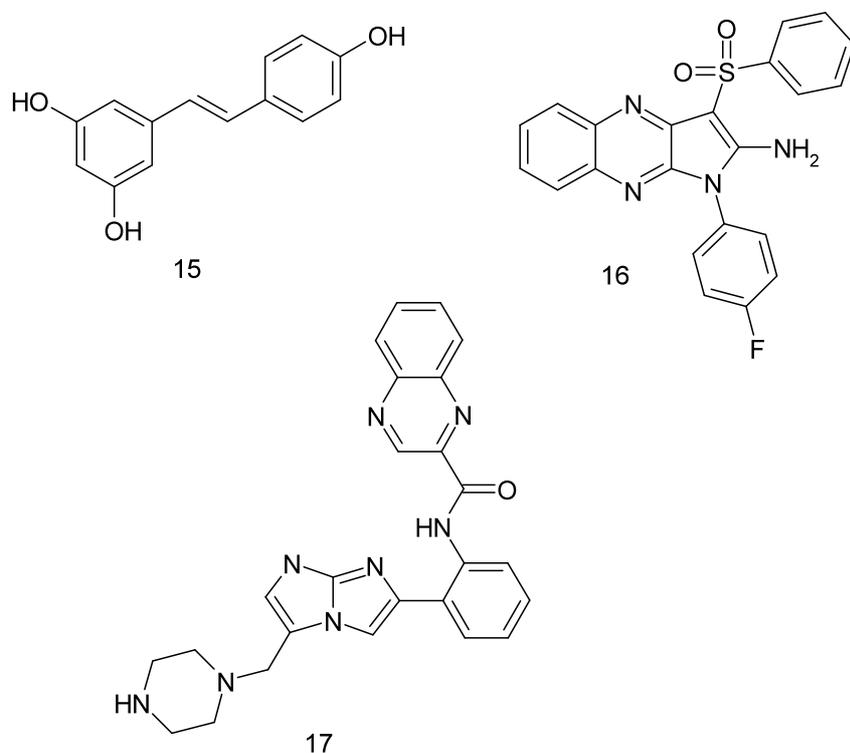
Figure 12: Molecular structure of Sirt1 activators **(15)** Reservatrol, **(16)** Pyrroloquinoxalline, **(17)** SRT-1720.

1.8 Aim of the work

The Sir2 family of proteins are class III histone deacetylases that are conserved in organisms ranging from archaea to human. The Sir2 complex represses transcription at telomeres, mating-type loci, and ribosomal DNA, and suppresses recombination. Sir2 proteins are active as NAD^+ dependent deacetylases, and many structural aspects are conserved throughout the protein family (including the core domain, acetyl-lysine substrate channel, and zinc binding module). Potent and subtype-selective inhibitors will be needed to distinguish between the biological function of the various Sir2 enzymes. Our work focuses on the design of selective and potent inhibitors of SIRT2, a member of the Sir2 protein family, through both analytical and theoretical methods.

The study was accomplished through:

- the discovery of novel inhibitor scaffolds through virtual screening
- the study of the binding mode and interactions of selected compounds with the SIRT2 protein
- the analysis of the stability of the selected compounds in the SIRT2 protein by means of molecular dynamic simulations
- the calculation of binding free energy calculations to predict the biological activity of novel and potent inhibitors
- the incorporation of experimental results from Prof. Manfred Jung's group (University of Freiburg)

Chapter 2

Computational Methods

The rapid development of computer technology and new modeling software in the last two decades gave a strong boost to the field of computer assisted molecular design (CAMD). X-ray crystallography, NMR and spectrometry provide data about bond energies, angles, electron density distributions and other properties of molecules. The increased availability of three-dimensional structures of small molecules and target proteins was essential for the establishment of computational drug discovery. The first part of this chapter presents a brief overview of current molecular docking techniques and scoring functions, which are applied to the discovery of binding modes for potential lead compounds. Virtual screening methods search large databases for compounds suitable for biological testing. The free energy section describes approaches used to predict binding energies of potential hit molecules.

2.1 Molecular Docking

Molecular docking is an important tool in structural biology and computer assisted molecular design. The main idea of this method is to predict the binding mode of a ligand for a protein with known three-dimensional structure. Docking methods are used to effectively search high-dimensional spaces and use scoring functions to correctly rank obtained conformations [99]. Several docking algorithms and techniques have been developed. The most commonly applied methods use genetic algorithms or molecular dynamics related search methods [100-104]. Protein flexibility is the main problem in current docking procedures. This is mainly due to the computational cost in exploring many degrees of freedom. Therefore docking a static protein structures is usually carried out. The flexibility problem of the ligand is handled e.g. by dividing the ligand into smaller fragments. *De novo* algorithms create new molecules from a fragment database whereas combinatorial docking algorithms use molecular libraries for docking. The most popular docking programs are `FlexX` [105], `Glide` [106], AutoDock [107], `DOCK` [108] and `GOLD` [109]. `FlexX` allows for flexible ligand docking into different binding site conformations, `DOCK` uses so called place and join algorithm, and `GOLD` implements a genetic algorithm. Some of the docking programs do not use force fields (`FlexX` and `GOLD`) to setup ligand structures. `DOCK` and `AutoDock` use an `AMBER` force

field, and therefore require partial charges. In this study `GOLD` and `DOCK` programs where used and detailed information are presented below.

`GOLD` (Genetic Optimisation for Ligand Docking developed by Jones *et al.* [109]) was one of the first docking programs and based on a genetic algorithm. The computer program "mimics the process of evolution by manipulating a collection of data structures called chromosomes" [109]. The implemented Goldscore scoring function consists of terms for protein-ligand hydrogen bonding, van der Waals energy, ligand torsional energy and internal van der Waals energy.

`DOCK` uses an incremental construction algorithm called place and join. The ligand is divided into two fragments having one atom in common, and then placement lists are created for each fragment. The `DOCK` algorithm searches through these lists for placement pairs, in which the common atom is located at the same point [108]. Finally, the fragments are reconnected, energy minimized, and scored.

2.1.1 Scoring Functions

Scoring functions are an important part of every docking program. There exist three types of scoring functions that are commonly used in molecular docking calculations: force-field based scoring, empirical and knowledge-based scoring. The force field based scoring uses non-bonded interaction terms and is usually more computationally expensive than the other methods [110-112]. A disadvantage of a force field based score is that they measure only potential energies rather than free energies; consequently electrostatic energies often dominate the docking. The force field score used in DOCK consists of the intermolecular terms of the AMBER energy function [113-115]. The GOLD program uses a scoring function that combines a Lennard-Jones potential with additional terms for hydrogen bonding. The energies of hydrogen bond between donors and acceptors are calculated using model fragments, and account for desolvation [116]. Empirical scoring techniques employ regression methods to fit coefficients of physically motivated structural functions by using a training set of protein-ligand complexes with measured binding constant. These scoring functions are implemented in many docking programs; they are fast and show good prediction of known protein-ligand complexes [117-119]. Knowledge based scoring functions apply statistical atom pair potentials derived from structural databases for scoring [120]. Known are also chemical

scores, contact scores, and shape complementary scores [121- 124]. There are plenty of scoring functions available today. Unfortunately none of them can reliably and consistently predict the binding strength of a protein-ligand complex [125-128]. Another common approach is consensus scoring, which combines two or more scoring functions to improve the results.

2.2 GRID - Molecular Interaction Fields

The GRID program was originally developed by Goodford [129]. The program calculates interactions between a "probe" (small molecule or molecular fragment) and a "target" (macromolecular system) in order to determine energetically favourable binding regions. The probes imitate the chemical characteristics of a fragment or binding mode. The interaction energy between a "probe" and "target" is calculated using equation (1).

$$E_{GRID} = \sum E_{LJ} + \sum E_{EL} + \sum E_{HB} \tag{1}$$

where (E_{LJ}) is Leonnard-Jones energy, (E_{EL}) is an electrostatic term and hydrogen bond interaction E_{HB}. This approach provides a numerous single and multi-atom probes such as hydrophobic named DRY or polar groups, with water or ions.

GRID is widely used to study small molecules such as drugs or molecular arrays such as membranes or crystals, and macromolecules, such as proteins, nucleic acids, glycoproteins or polysaccharides [130-134]. GRID can be used to understand the structural differences related to enzyme selectivity, a fundamental component of rational design of drugs [135].

2.3 Virtual Screening

Virtual screening (VS) and High-throughput screening (HTS) are techniques regularly used in drug discovery. HTS is employed to experimentally screen hundreds of thousands of compounds against a target protein. This is in contrast to a theoretical approach [136-138] that was designed for searching large databases and selecting candidate molecules for biological testing. In recent years, VS methods have become common in drug discovery research, as they reduce the number of candidate molecules to be tested by HTS [139]. A variety of similarity searching tools can be implemented in VS such as various two-dimensional (2D) and three dimensional (3D) structural queries, pharmacophore models, 2D and 3D

fingerprints and QSAR models [140-143]. There are many examples of successful virtual screening (VS) applications in the literature. Shapira *et al.* [143, 144] found a new agonist and antagonist for Retinoic acid receptor, Klebe *et al.* [145] found several novel inhibitors for human carbonic anhydrase II, and small number of compounds potentially inhibitors of RNA were found. Another reported application of (VS) was 3D pharmacophore searching in discovery of VLA-4 integrin antagonists with submicomolar activity [146].

A variety of filtering methods can be applied to eliminate compounds with unwanted properties. One valuable approach is the removal of substances containing reactive, toxic or undesirable groups. In a next step, so called Lipinski rule of five [147] should be applied to evaluate druglikness. According to this rule the molecular weight of a molecule should be lower than 500, the lipophilicity expressed by clogP octanol/water partition coefficient should be lower than 5, the number of hydrogen bond donors should not be larger than 5, the sum of nitrogen and oxygen atoms should not be higher than 10.

2.4 Molecular Dynamics Simulations

The first molecular dynamic (MD) simulation was performed by Alder and Wainwrigt in the late 1957 to study the relaxations accompanying various nonequilibrum phenomena [148], the first publication describing an MD simulation of experiments explored bovine pancreatic trypsin inhibitor (BPTI) [149]. The following years brought a big interest in MD simulation for the study of both proteins and nucleic acids. Most of these studies focused on the physical aspects of the internal motions, and provided the interpretations for experimental results. The MD simulation programs used, for example, AMBER [150], GROMACS [151] and CHARMM [152], still have a wide range of capabilities.

MD simulations can be understood as an analogy to a real experiment but in a *virtual* (hypothetical) environment. In this experiment, one can prepare a sample of the material of interest, connect the sample to a measuring instrument such as manometer or thermometer and measure it during a certain time interval. The longer we average and measure, the more accurate measurements we have. In MD simulations, one uses exactly the same approaches. Firstly, the sample is prepared, then usually a model system is selected that consist of N particle of the sample, then Newton's equations of motion for this system are solved until the properties of the system no longer change with time. When this occurs, the system is said to

have been equilibrated. Netwon's equation of motion is given by (2)

$$\mathbf{F}_i = \mathbf{m}_i \mathbf{a}_i \qquad\qquad (2)$$

where, Fi is the force exerted on particle i, m$_i$ is the mass of particle i, and a_i is the acceleration of particle i.

All simulation methods require a potential energy surface, which can be usually accomplished by applying the laws of classical mechanics. Applications of molecular mechanics employ energy minimization, molecular dynamics and Monte Carlo methods to move around the hypothetical potential energy surface (Cornell) [153]. These methods are effective at modelling non-covalent interactions between the molecules.

Analytical potential energy functions are used in simulation studies describe bond stretching, bond angle deformation, torsional and dihedral angle space and non- bonding terms including the short range van der Waals interactions and the long range electrostatic contributions. Bond stretching and bond angle deformation forces are usually represented by a simple harmonic potential. Torsional rotation forces are generally modelled with a truncated Fourier series, and non-bonded van der Waals interactions are most often represented as Lennard-Jones (exchange and dispersion) and Coulomb (electrostatic) potentials [154]. Electrostatic and van der Waals interactions are calculated between atoms in different molecules, or for atoms in the same molecule separated by at least three bonds. The energy of the system is given by,

$$E(R) = \frac{1}{2} \sum_{BONDS} K_b (b - b_0)^2 + \frac{1}{2} \sum_{\substack{BONDS \\ ANGLES}} K_\Theta (\Theta - \Theta_0)^2 + \frac{1}{2} \sum_{TORSIONAL} K_\phi [1 + \cos(n\phi - \delta)]$$

$$+ \sum_{NB-PAIRS} \left(\frac{A}{r^{12}} - \frac{B}{r^6} + \frac{q_1 q_2}{D_r} \right) \qquad (3)$$

where, the energy, E, is a function of the Cartesian coordinate set, R, specifying the positions of all the atoms, from which the internal coordinates for bond lengths b, bond angles, dihedral angles $\Theta\varphi$, and interparticle distances r are calculated. K_b and $K\varphi$ are force constants. The first term in equation 3 represents displacement from the ideal bond length, b_0 by a Hooke's

21

law (harmonic) potential. This is the first approximation to the energy of a bond as a function of length. Bond force constants determine the flexibility of the bond and can be evaluated from infrared stretching frequencies or quantum mechanical calculations. Ideal bond lengths can be inferred from high resolution or low temperature crystal structures. The energy associated with alteration of bond angles, given by the second term in equation 3, is also represented by a harmonic potential. For rotations about bonds, a torsion angle potential function is given by the third term in the equation.

MD method can be implemented to study the behaviour of a molecular system and to provide the physical basis of the structure and function of a macromolecular system. Processes such as melting, adsorption and formation of molecular complexes can be investigated. Such studies may lead not only to improved understanding and insight, but also to practical results such as engineered proteins or materials with properties optimized for particular applications. It is clear that the results available from molecular dynamics will play important roles in the future for understanding biology and chemistry.

The main drawback of MD is simulation time, which is currently limited to nanoseconds due to the complexity of calculating protein folding and configurational sampling. With rapidly growing computer memory and computational capabilities, simulation times may be expanded to microseconds in the near future.

2.4.1 Simulation Methods

The first technique applied in computer simulation studies for large biological molecules was energy minimization. The energy of the macromolecule (*e.g.* protein) is minimized as a function of the atomic coordinates. Initially, strongly repulsive interactions are eliminated and velocities are assigned to the atoms. Next, the equilibration phase is performed such that the measurable properties become stable with respect to time. The equilibration period is performed until the potential energies are stable.

2.5 Binding Free Energy Methods

Since understanding the energetics of molecular complexes can speed the discovery of high affinity ligands, the ability to correctly predict binding free energy (BFE) has becoming one of the major goals of computational chemistry. The binding free energy of a protein-ligand complex can be understood as the energetic preference of the ligand to the protein binding

pocket over the solvent. A variety of methods are used to predict the binding free energy of small molecules. Two common methods are empirical techniques, which are based on simple energy functions [110-112], and knowledge-based statistical scoring, which is based on the frequency of various atom-atom contact pairs in complexes [120]. These methods are computationally inexpensive but the lack of conformational sampling and explicit water treatment decrease their accuracy. Another group of BFE methods use molecular dynamics (MD) or Monte Carlo simulations (MC), and comparative studies have shown these techniques to be more accurate than those based on a simple energy functions. Unfortunately, the calculation of BFE makes them more time-consuming. These BFE calculation methods are often used in the study of energetic differences among a series of ligands or protein mutants. Binding free energy simulations are frequently carried out as shown in (Figure 13) [155].
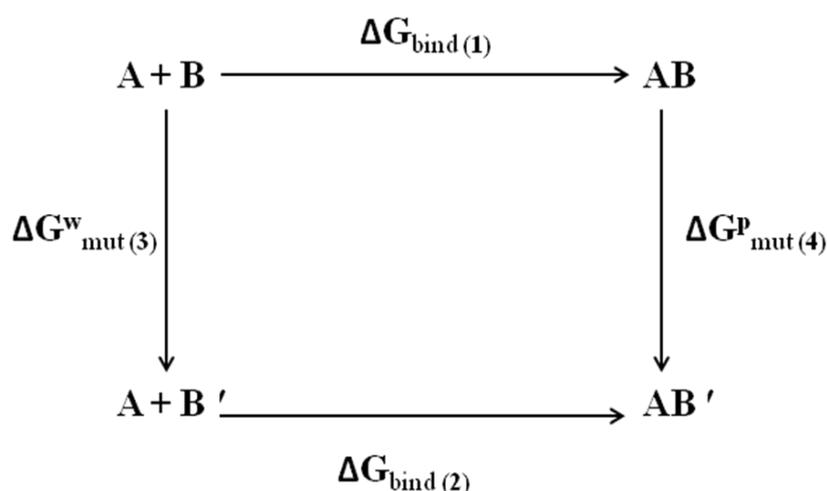
Figure 13. Thermodynamic cycle describing the calculation of the relative binding free energies of two ligands, B and B' to a receptor molecule A. The absolute binding free energy can, in principle, be obtained by treating B as a dummy ligand and taking into account the relevant standard state in terms of volume/concentration (Hermans and Wang, 1997). The binding free energy change can be calculated from horizontal or vertical components: $\Delta\Delta G = \Delta G_{bind(1)} - \Delta G_{bind(2)} = \Delta G^p_{mut(4)} - \Delta G^w_{mut(3)}$.

Where A is the enzyme, B is an inhibitor and B' is the modified inhibitor, A+B represents the unbound state and AB represents the bound state. ΔG^w_{mut}, ΔG^p_{mut} denote the difference in free energy between B and B' when bound to the solvated receptor binding site and in water. In other words, the relative free energy difference in binding between the two inhibitors is equal to the difference in the free energies calculated for the non-physical mutations [155-157].

The most advanced binding free energy approaches are free energy perturbation (FEP) and thermodynamic integration (TI). In these methods, free energy is calculated by slowly changing one system into another using a set of unphysical states running MD or MC simulations. Unfortunately these types of calculations are computationally demanding and the techniques are limited to only a few similar ligands (~10) [155-159]. In addition, more approximate methods have been developed, e.g. molecular mechanics Poisson-Boltzmann surface area (MM-PBSA) [160] and linear interaction energy (LIE) [161]. Both have become of interest in drug discovery as an alternative for predicting relative binding free energies. These two methods are described below in detail.

2.5.1 Molecular Mechanics Poisson-Boltzmann Surface Area (MM-PBSA)

The MM-PBSA and molecular mechanics-generalized Born surface area (MM-GBSA) combine molecular mechanics and continuum solvent models to estimate ligand binding affinities of ligand-protein, protein-protein or nucleic acid complexes [160]. This approach was initially developed to study the stability of DNA and RNA fragments [162], but has also been used in recent years to estimate ligand binding free energies [160]. The MM-PBSA algorithm combines explicit solvent molecular dynamics (MD) with implicit solvation models. A set of snapshots from MD trajectory is saved as representative conformations of a macromolecular complex. Then the water molecules are removed and replaced by a continuum solvent model. The free energy of the complex consists of the molecular mechanics potential energy of the solute, the solvation free energy, and a solute entropy term. The solvation free energy consists of electrostatic or polar portion and non-polar solvation contribution. The binding affinity is estimated from the free energies of the receptor, the ligand and the complex based on equation (4).

$$\Delta G_{binding} = G_{complex} - [G_{protein} + G_{ligand}] \qquad (4)$$

where $G_{complex}$ is the absolute free energy of the complex, $G_{protein}$ is the absolute free energy of the protein, and G_{ligand} is the absolute free energy of the ligand. The free enrgy of each term is estimated as a sum of four terms:

$$G = <E_{MM}> + <G_{PBSA}> - T<S_{MM}> \qquad (5)$$

$$E_{MM} = E_{int} + E_{ele} + E_{vdw} \qquad (6)$$

in which T is the temperature of the system in Kelvin, $<E_{MM}>$ is an average of molecular mechanical energy that includes bonds, angles, torsions, and a sum of van der Waals, electrostatic and internal energy equation (6), $<G_{PBSA}>$ is the continuum solvation free energy which is composed of an electrostatic term, usually calculated using a Poisson-Boltzmann (PB) model and a hydrophobic non-polar term, which is proportional to the solvent accessible surface area (SA) [160,162]. The last part $<S_{MM}>$ is the entropy term, which can be estimated by quasi-harmonic analysis of the trajectory or by normal mode analysis [162].

There are two ways to run MM-PBSA, one is to use only a single trajectory of a complex according to equation (4). The second alternative is to use trajectories for both a complex and unbound molecules and evaluate the terms in equation (5) with a subsequent determination of $\Delta G_{binding}$ based on equation (4). As it can be seen, the first way of running MM-PBSA costs less time, free energy is not converged during simulation time. The second option would be difficult to use in protein-ligand studies because there is no way to calculate the $<E_{MM}>$ term to converge it for receptor or complex within reasonable computational time. So probably this option has never been used in protein-ligand study. It turns out that using a single trajectory approach can get better results if there is no significant conformational change in the protein structure.

The MM-PBSA was successfully applied in several macromolecular systems [163-165] but not for others. Calculating binding free energy interactions for a series of p38 MAP kinase complexes gave very poor results compared with other approaches [166]. Langen *et.al* studied the selectivity of the human glucocoriticoid receptor (hGR) with five steroids, cortisol, progesterone, aldosterone, testosterone and estradiol [167]. Using MM-PBSA approach for different complexes he could properly discriminate compounds with strong affinity from those with weak binding. However for low-affinity ligands could not predict the correct rank. Kuhn and Kollman [163] studied *avidin* inhibitors; authors found that free energy components for solute entropy were quite variable; they concluded that more accurate methods should be developed to predict entropic changes.

This method has theoretical restrictions, which may limit their applicability and accuracy [162-166]. A difficult task in MM-PBSA approach is to determine the entropy contribution upon binding especially when conformational fluctuations are significant. If ligands are closely related, it is possible to ignore it assuming that $<S_{MM}>$ is the same for all of them. For structurally different compounds, the change in solute entropy can vary and must be included.

2.5.2 Linear Interaction Energy (LIE)

Recently Aqvist *et al.* proposed method for estimation binding affinities, known as linear interaction energy approximation LIE [161]. This is a semiempirical method, based on linear response theory, which is less computationally expensive than free energy perturbation methods FEP. This method rely on the simulation of several different states , mostly unphysical, whereas LIE approach uses the initial and final states of binding process, which is the free and bound state of ligand. LIE is also faster than FEP and MM-PBSA uses explicit solvent model, which means that desolvation can be reasonably handled. These advantages make LIE very useful tool in structure-based lead optimization, which helps to understand detailed interactions between the lead compounds and their receptor, and to estimate binding affinities.

The concept of the LIE approach is to separately calculate the van der Waals and electrostatic interaction energies for the ligand in water and ligand in complex with solvates protein [168]. Then, averages of interaction energies between the ligand and its surrounding are analyzed. The LIE equation is known as:

$$\Delta G_{calc} = \alpha \Delta E_{vdw} + \beta \Delta E_{elec} + \gamma = \alpha \ (E_{B\_vdw} - E_{F\_vdw}) + \beta \ (E_{B\_ele} - E_{F\_ele}) + \gamma \qquad (7)$$

where the Δ term indicates the change in energy from the ligand free and bound state (E_{bound} - E_{Free}). The α, β and γ are LIE fitting parameters, determined by comparing calculated and experimentally estimated binding affinities. Obtaining suitable values α and β has been subject of several investigations described recently. Aqvist *et al.* have found that $\alpha \approx 0.5$ and $\beta \approx 1.043$ are best to correlate the calculated binding free energies with the experimental values [168]. On the other hand Jones-Herzog and Jorgensen observed that $\alpha \approx 0.5$ and $\beta \approx 0.161$ are not optimal for sulfonamide inhibitors with human thrombin [169]. It means that these two

parameters can be protein dependent. Proper fitting parameters must be determined by comparing calculated and experimentally estimated binding affinities, they depend also on the investigated system and used force field. The γ parameter is co called additional constant, which sometimes needs to be added in order to obtain reasonable binding free energy predictions [169].

In many cases the binding free energies obtained from LIE approach showed to be in very good agreement with experimental results. Meerman *et al.* [170] predicted binding affinities of ligands bind to the estrogen receptor ERα isoform, combining MD simulations and LIE calculations, obtained excellent linear interaction energy (r^2=0.94, *n*=19). In the work on thrombin inhibitors was demonstrated that using LIE approach is possible to predict relative affinities of chemically different ligands, but γ=-2.9 kcal/mol parameter was needed in order to estimate good predictions [171]. Paulsen and Ornstein applied the methodology to a series of cytochrome P45-camphor analogue complexes using the CVFF force field [172] using α=1.043, β=0.5 and γ=0 obtained very good correlation coefficient. Another example, Luzhkov *et al.* studied binding of several sertindole analogues which block the hERG K^+ channel, LIE model gave also very good agreement with experimental values [173].

There are several advantages of the LIE approach, firstly is faster that FEP or MM-PBSA calculations because LIE simulates directly the end sates. Secondly, LIE and FEP taking into account the protein flexibility which is not always included in scoring functions. LIE uses explicit solvent model, so the desolvation free energy can be reasonably handled.

Chapter 3

Molecular Modeling Studies of SIRT2 Proteins

The crystal structures of human and yeast sirtuins in complex with NAD^+ have been determined and analyzed recently, but the exact binding mode of NAD^+ to human SIRT2 is still unclear. Thus, MD and MM-PBSA methods were used to gain insight the interaction details of NAD^+ at the catalytic site of human SIRT2.

3.1 Structure Analysis

The X-ray structures of several Sir2 proteins have been published over the last few years. The structure of the catalytic domain of Sir2 consists of a large classical Rossman fold and a small zinc binding domain. The interface between the large and the small subdomain is commonly subdivided into A, B and C pockets. This division is based on the interaction of adenine (A), ribose (B), and nicotinamide (C), (Figure 5, chapter 1.5.3), which are parts of the NAD^+ cofactor. The binding site for the adenine and ribose moieties has been well described in many studies (e.g. Sir2-Af1 [174], Hst2 [175], Sir2-Af2 [176], SIRT2 [177]), but the location of the nicotinamide moiety of the NAD^+ has been reported to be variable. Multiple binding modes have been observed for the nicotinamide portion. Several so-called productive and non-productive conformations of NAD^+ have been observed in the crystal structures from Archaeabacteria, reflecting the flexibility of this part of the cofactor and the corresponding binding site. Avalos *et al.* [176] showed the binding of free nicotinamide to the C-part of Sir2Tm and Sir2-Af2, in a configuration where NAD^+ is suggested to be active for catalysis. The catalysis is assumed to take place when NAD^+ changes its conformation from a non-productive to a productive conformation [178]. The nicotinamide subpocket is linked with a flexible loop; some residues in this loop are highly conserved in sirtuins. Avalos *et al.* called this loop "front wall" of the C subpocket or a "ceiling" [176]. The flexibility of this loop can be detected in different sirtuin crystal structures (e.g Sir2-Af1, Sir2-Af2, Hst2). It has been observed that in sirtuins cocrystallized with NAD^+ or ADP-ribose the loop shares a similar orientation and seems to be tighter in comparison to those without NAD^+ (Figure 14, and Figure 15). Also the acetyl-substrate channel seems to be more closed for sirtuins in complex with NAD^+ or ADP-ribose (i.e. Sir2-Af1 (1M2G) and Sir2Af2 (1S7G) Figure 14 and 15). Additionally in the X-ray structure of a Sir2 homologue from Archaeabacteria [176] a peptide structure was found that binds in a cleft between the large and small domains nearby NAD^+

(Figure 15). The position of ADP-ribose is nearly identical in all available Sir2 X-ray structures that bind NAD^+ or ADP-ribose (Figure 15, 16 and 17). Only the location of the nicotinamide ring is different in Sir2-Af1 (faces the flexible loop) and Sir2-Af2 (sticks outside the binding pocket), which can be inferred from the position of the ribose group. Interestingly, the nicotinamide-ribose part of NAD^+ in Sir2-Af2 does not bind to C-site residues, but was proposed to be involved in the polarization and hydrolysis of the NAD^+ glycosidic bond [176]. On the other hand in Sir2-Af1 the conformation of nicotinamide-ribose adopts a position that allows the ribose ring to make hydrogen bonds to His116 and the nicotinamide ring to the crystal water molecules (Figure 22). In the case of the human SIRT2 X-ray [177], which was crystallized as trimer, no structural information about NAD^+ or inhibitor binding is available. However, owing to the homology with bacterial sirtuins, it is clear that the interaction between NAD^+ and Sir2 is likely to be similar to that observed in the bacterial X-ray structures. Only the position of nicotinamide ribose rings may be different.
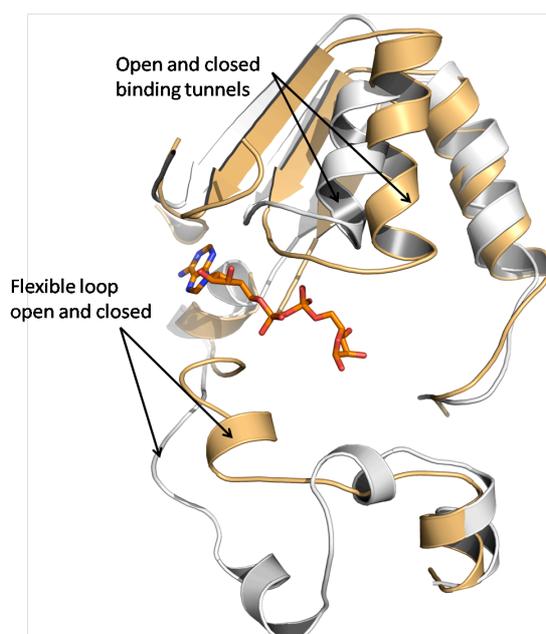
Figure 14: Schematic representation of superposed crystal structures of Sir2-Af1 (orange) (PDB ID 1M2G) and human SIRT2 (white) (PDB ID 1J8F).
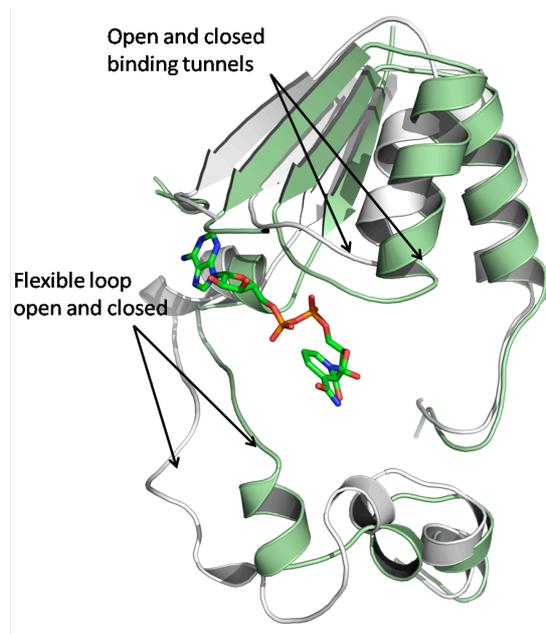
Figure 15: Schematic representation of superposed crystal structures of Sirt-Af2 (green) (PDB ID 1S7G) and human Sir2 (white) (PDB ID 1J8F).
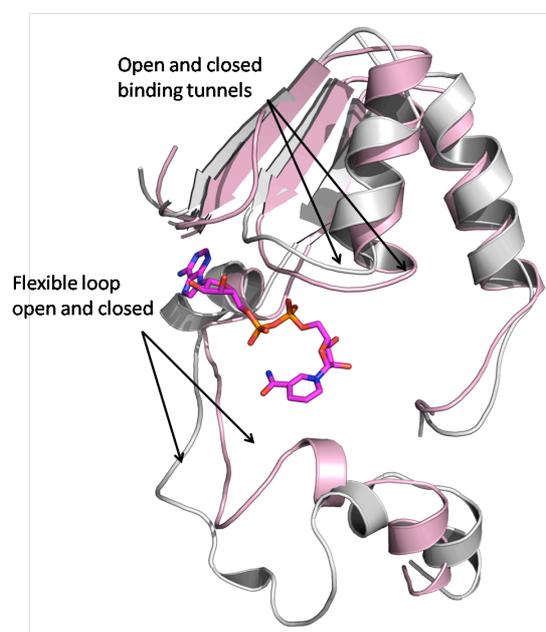
Figure 16: Schematic representation of superposed crystal structures of Sir-Af1 (violet) (PDB ID 1ICI) and human SIRT2 (white) (PDB ID 1J8F).

3.2 Docking Studies

NAD$^+$ was docked using DOCK to the human SIRT2 domain-B and the best twenty poses were scored, amongst which the most plausible docked coordinates were selected based on their resemblance to the hydrogen bonding pattern found in NAD$^+$ in complex with the

bacterial homologues of Sir2 [174-177]. All docking results were analyzed in detail by visual inspection and two main clusters of docking poses were selected representing the productive and non-productive conformation of NAD^+ (Figure 17). The difference between these two docking solutions is the position of the nicotinamide ribose part of NAD^+: one faces towards the binding pocket (Figure 17 magenta) and one sticks more outside the pocket (Figure 17, colored cyan). Prediction of the exact location of the nicotinamide moiety in the C site of human SIRT2 is quite difficult, because the corresponding groove is much wider than that observed in Sir2-Af1 or Sir2-Af2. Thus for the further analysis two conformations (conf. 1 and conf. 2) were considered. Obtained binding energies for these two poses were similar: for conf.1 -84.04 kcal/mol whereas conf. 2 the score is -82.42 kcal/mol (Table 2). In both cases the nicotinamide ring is positioned in the hydrophobic C- pocket: conf. 1 interacts with Val233 (Figure 18) and conf. 2 makes hydrogen bonds to Ile169 (Figure 19). The planar adenine ring of NAD^+ fits perfectly in the Rossmann fold domain, and forms hydrogen bonds to Thr89, Glu323 and Asn286 (Figure 17, 18, 19). X-ray structure of Sir2-Af1 shows very similar hydrogen bond contacts as predicted for the two conformations obtained from the docking study on human Sirt2: the adenine ring is surrounded by Glu29, Asp213 and Asn211 (Figure 21). The pyrophosphates part of NAD^+ lies in a central position of the binding pocket. We observed similar hydrogen bonding with NAD^+ bound to Sir2-Af1 and Sir2-Af2 (Figure 20, 21 and 22). The main residues that make hydrogen bond interactions with the B pocket are Ser263, Thr262, Ala86 and Gln167. In the conf. 1, the ribose adopted a position that allows to form a hydrogen bond with Ile169 while conf.2 to form hydrogen bond with His187 which is similar to the interactions of Sir2-Af1 with NAD^+.
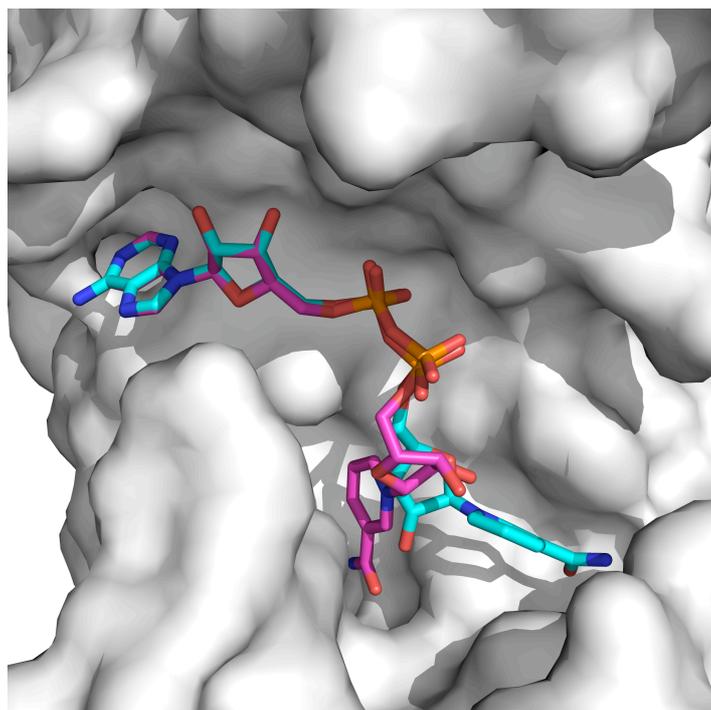
Figure 17: Obtained docking poses for NAD$^+$ at human Sirt2. Docking studies were carried out using DOCK v6.1 (UCSF) [108] (conf. 1 is colored cyan, conf. 2 in magenta).

Table 2: Binding energy E_{bind} (kcal/mol) obtained for two the best docking conformations of the NAD$^+$, E_{vdw} and E_{ele} represents Van der Waals and electrostatic energies.

	E_{bind}	E_{vdw}	E_{ele}
conf. 1	-84.04	-71.70	-12.33
conf. 2	-82.42	-69.55	-12.87
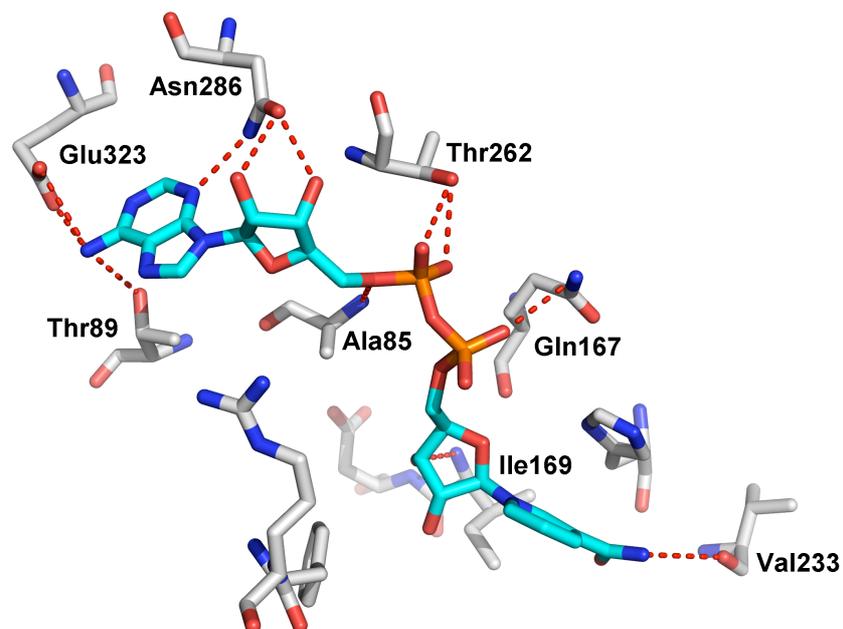
Figure 18: Interaction of NAD$^+$ docked into the binding pocket of human SIRT2 (conf. 1). Hydrogen bonds are shown as dashed line.
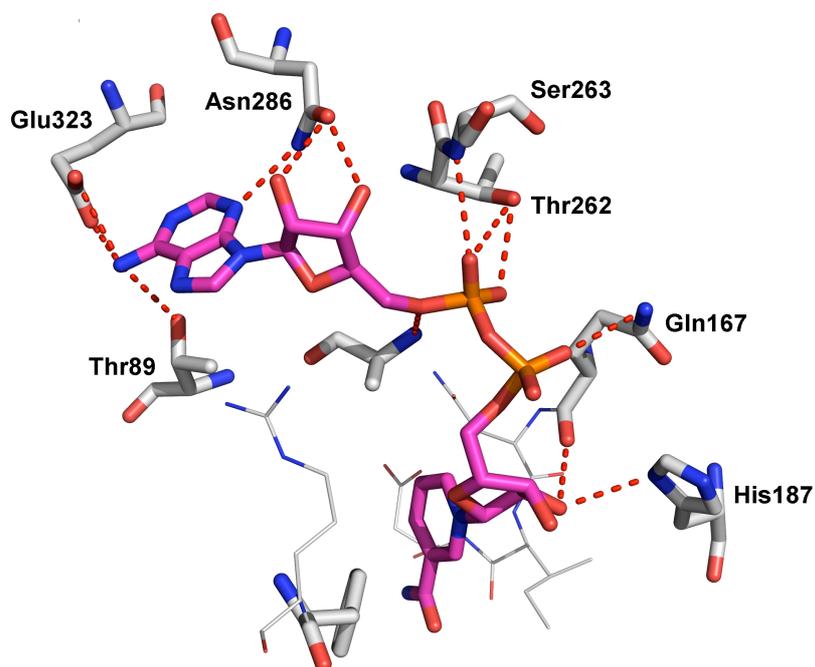
Figure 19: Interaction of NAD$^+$ docked into the binding pocket of human SIRT2 (conf. 2). Hydrogen bonds are shown as dashed line.
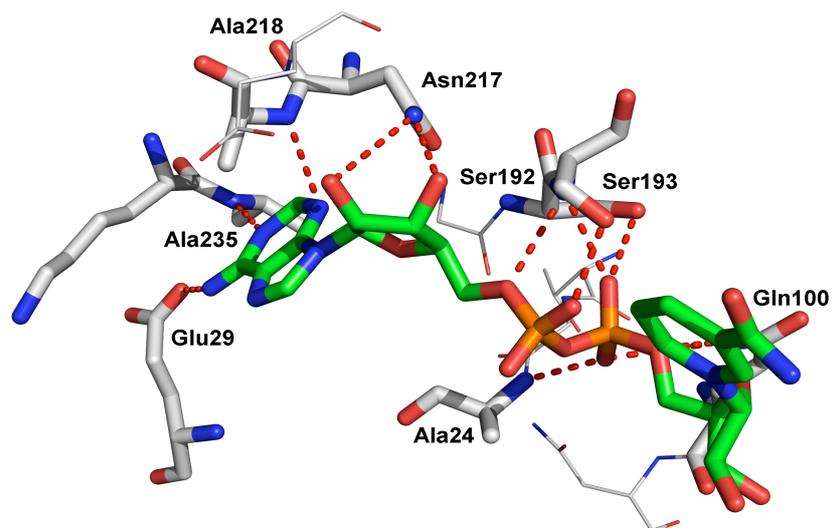
Figure 20: Interaction of NAD$^+$ (green) in the binding pocket of Sir2-Af2 (PDB ID 1S7G). Hydrogen bonds are shown as dashed line.
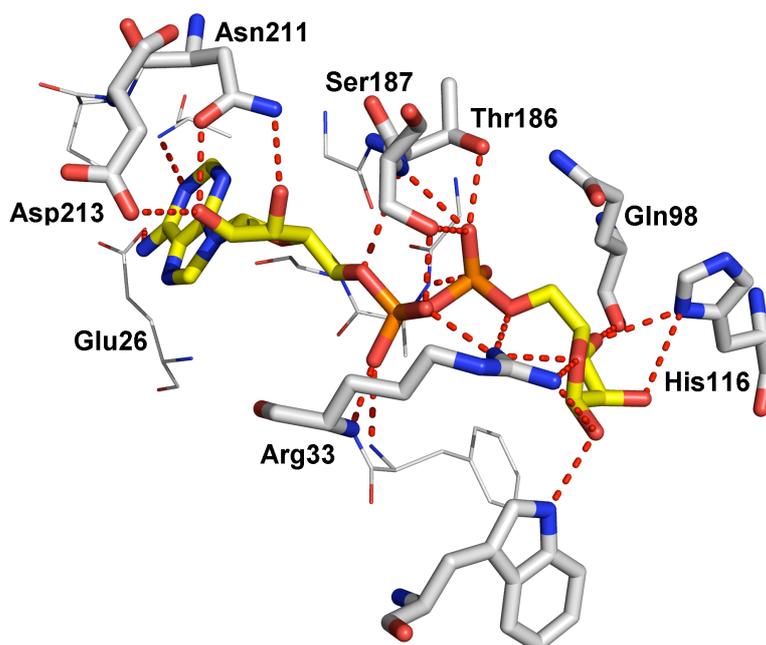
Figure 21: Sir2-Af1 (PDB ID 1M2G) in complex with ADP-ribose (yellow). Hydrogen bonds are shown as dashed line.
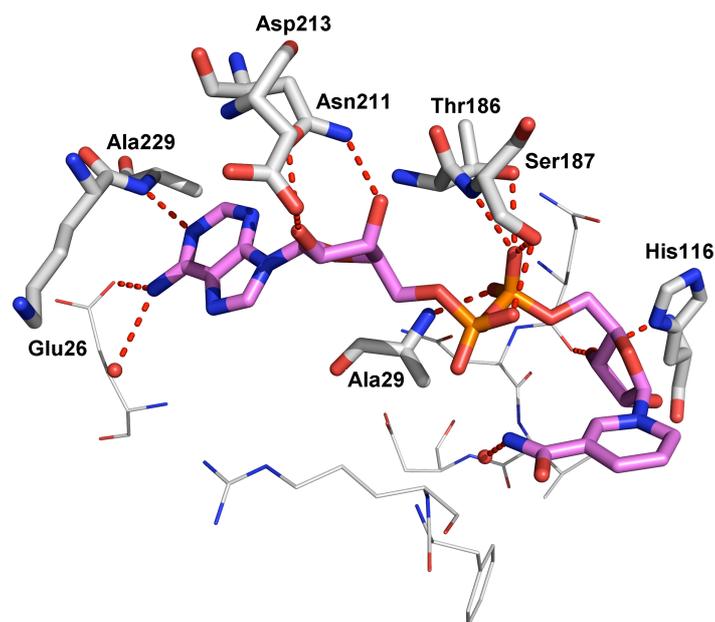
Figure 22: Sir2-Af1 (PDB ID 1ICI) in complex with NAD$^+$ (magenta). Hydrogen bonds are shown as dashed line.

3.3 Molecular Dynamics Simulations

3.3.1 Dynamical Behaviors of Human SIRT2

To analyze the human SIRT2 structure, different MD simulations were applied for the NAD$^+$ bound and unbound form. Starting structures for these MD simulations were taken from the docking study described in chapter 3.2. To assess the stability of the complexes, the root-mean-square deviation (RMSD) values with respect to the initial structures were calculated. The RMSD values for unbound human SIRT2 along the 12.5-ns simulation period is shown in Figure 23. It can be seen that the unbound form reaches an equilibrium state beyond 6 ns and this steady-state is maintained through the rest of the MD simulation oscillating around 4 Å RMSD referenced to the crystal structure coordinates, suggesting that the conformation is structurally stabilized.

When NAD$^+$ binds to human SIRT2 in the conf. 1, the complex reaches its equilibration state beyond 7 ns and oscillates also around 4Å (Figure 24), suggesting that the binding affinity on NAD$^+$ in this simulation time is favorable. The bound human SIRT2 has larger RMSD fluctuations (Figure 24, black) than the unbound form (Figure 23). Visual inspection of the bound human SIRT2 trajectory revealed that the adenosine-phosphate part of NAD$^+$ is very

stable during the MD simulation and is positioned in the A and B sub-pocket during 10 ns whereas the nicotinamide part rotates to some extend and oscillates in and out of the C sub-pocket. At the end it is stabilized in the entrance of the acetyl-lysine substrate channel (see Figure 24, red and Figure 26). The RMSD plot pattern for NAD$^+$ bound SIRT2 exhibits three sharp peaks at 2200 ps, 4300 ps and 4500 ps, which show the flexibility of the nicotinamide group. As can be clearly seen in Figure 24, there is a jump at 5 ns and the RMSD increase from 3 Å to around 4.8 Å, which is due to a sudden leaving of the nicotinamide group from the binding pocket C (Figure 25).
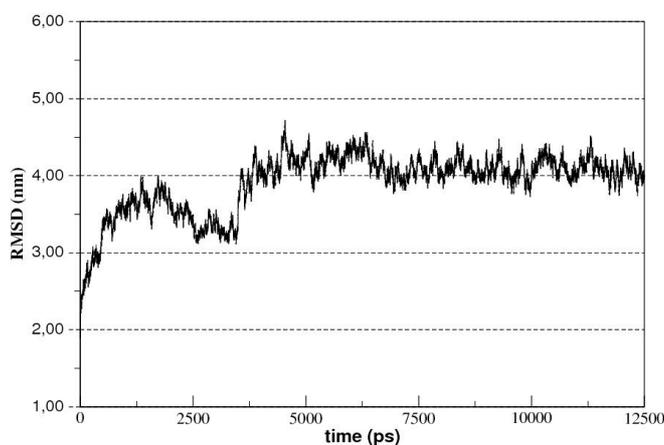
Figure 23: Root mean square deviation (RMSD) plot for unbound human SIRT2.
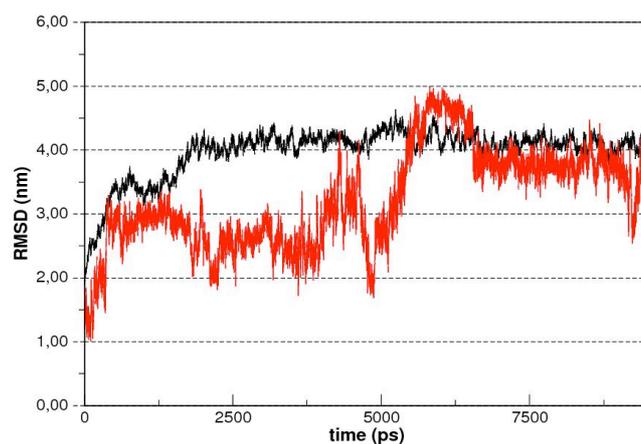
Figure 24: Root mean square deviation (RMSD) plot representing bound human SIRT2 (black) and bound NAD$^+$ (red) obtained for the conf. 1.

36

Beyond 6 ns of MD simulations the n-ribose and nicotinamide part stabilizes and faces towards the binding channel (Figure 25 and 26). Interestingly, in this stable conformation residues located in the C-site are no longer in direct contact with NAD^+ (Figure 26). During MD simulations significant fluctuations of the loop regions and acetyl-lysine channel were observed. It can be seen that for unbound SIRT2 the flexible loop is stable during the simulation, whereas for the bound form the loop seems to close the binding pocket (Figure 26). Upon NAD^+ binding, the conformation of the acetyl lysine binding tunnel closes up while this tunnel is open in the absence of NAD^+ (Figure 26); a similar situation can be observed in the X-ray structure of Si2-Af2 (Figure 15).

Figure 27 presents the superposition of the Sir2-Af1 crystal structure with the MD structure of human SIRT2 over the last 2 ns. It can be seen that the flexible loop from human SIRT2 moved during the MD and adopted similar position to the loop observed in the X-ray structure of Sir2-Af1 in complex with ADPR (Figure 27).
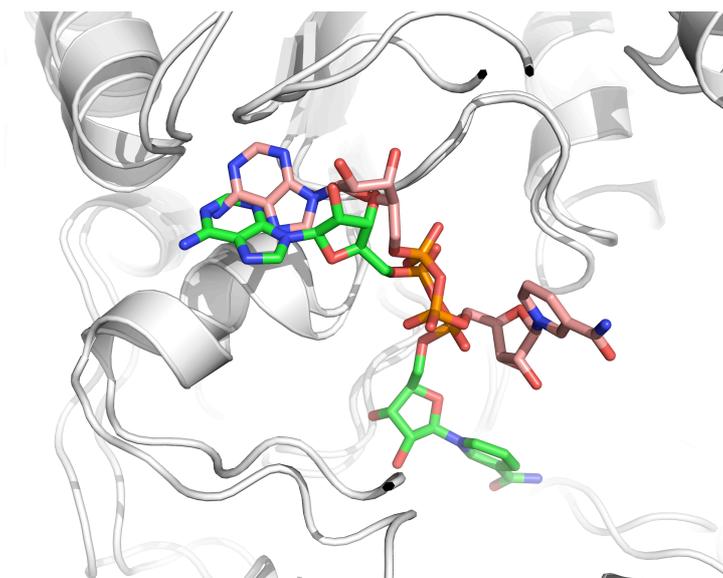
Figure 25: Snapshot (5 ns) from the simulation of human SIRT2 complexed with NAD^+. The nicotinamide group of NAD^+ has changed its position from the inside of pocket C (green) to the outside (pink).
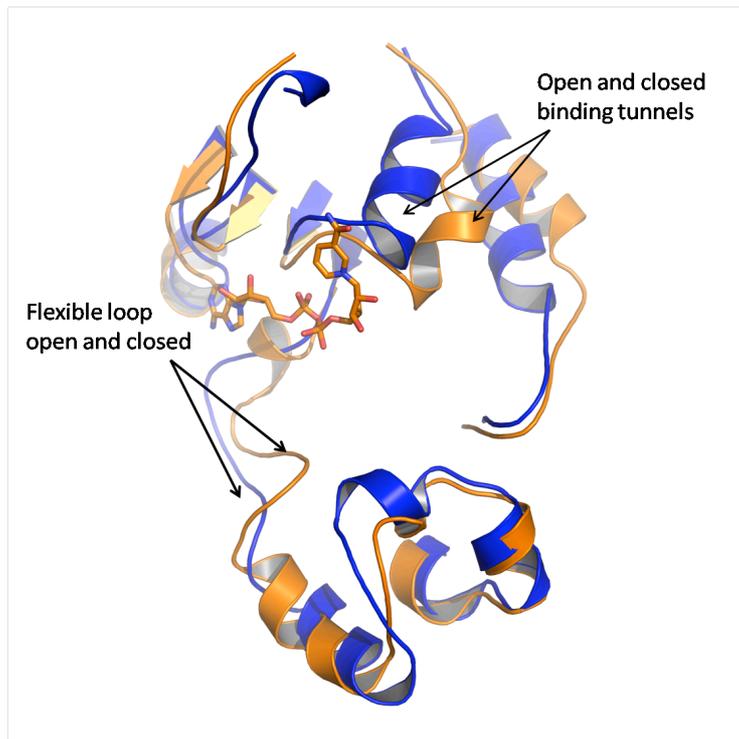
Figure 26: Superposition of human SIRT2 complexed with NAD$^+$ (orange) and unbound SIRT2 (blue). The starting NAD$^+$ conformation was conf. 1.
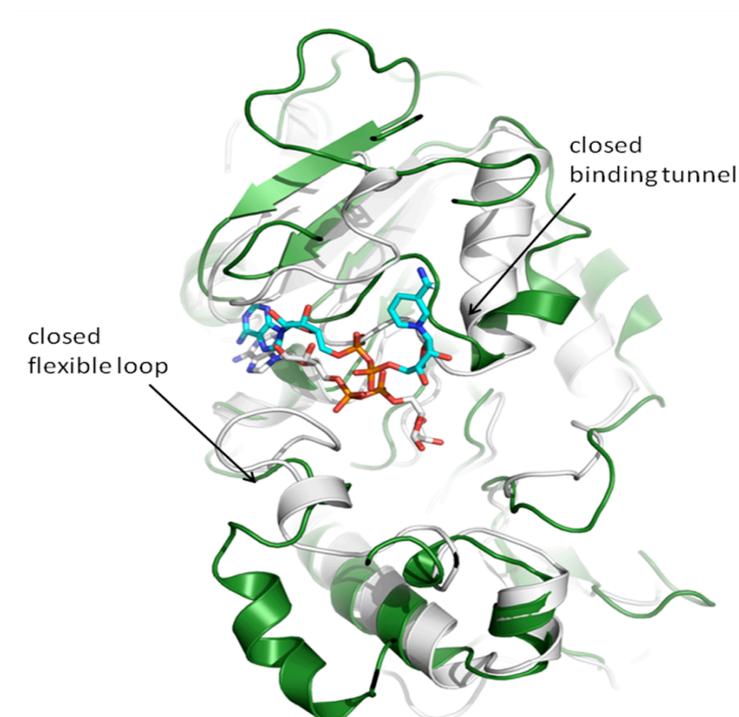
Figure 27: Human SIRT2 (green) complexed with NAD$^+$ (cyan) and Sir2-Af1 in complex with ADP-ribose (grey).
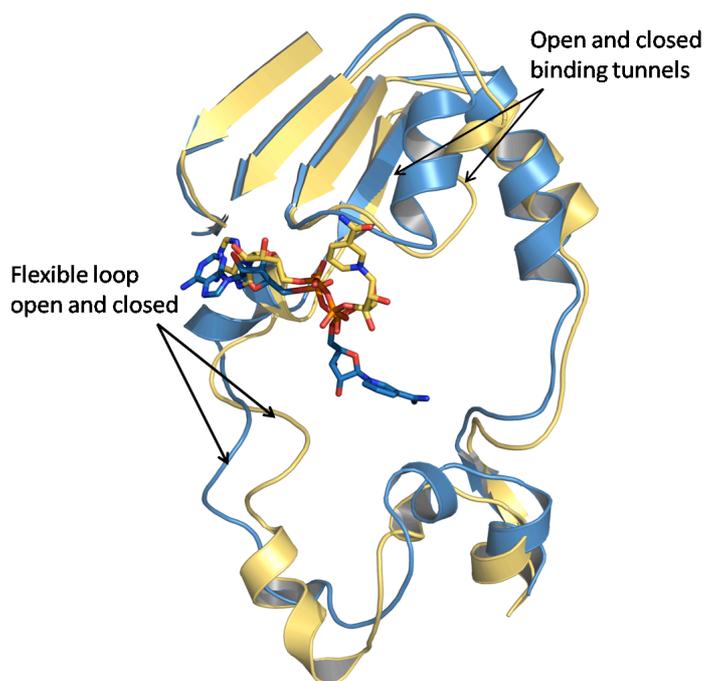
Figure 28: Human SIRT2 complexed with NAD$^+$ at the beginning of the MD simulation (blue) and at the end (yellow).

The second NAD$^+$ conformation obtained from the docking study (Figure 17, magenta and Figure 19) reaches an equilibrium state beyond 12.5 ns and this steady state is maintained with less than 4 Å referenced to the starting coordinates (Figure 29).
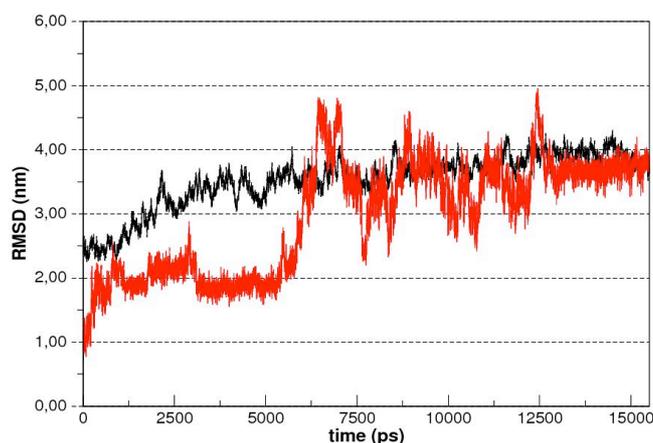
Figure 29: Root mean square deviation (RMSD) plot representing bound human SIRT2 (black) and bound NAD$^+$ (red) obtained for the conf. 2.

On the RMSD plot in Figure 29 four sharp peaks at 6200 ps, 7100 ps, 9000 ps and 12500 ps of the simulation are observed. The RMSD significant jumps beyond 5 ns, which is attributed

to the leaving nicotinamide group, form the C subpocket area (Figure 30). Then the nicotinamide ribose ring slightly shifts towards the flexible loop (Figure 30, 31). Visual inspection of the trajectory reveals that like in the previous conformation the ADP part of NAD$^+$ is positioned in the Rossman fold (Figure 31), while the nicotinamide group shows higher flexibility. We observed here also that Arg97 (Figure 30) makes hydrogen bonds with the phosphate group of NAD$^+$ while the ribose nicotinamide rings remains in the C-pocket, which may indicate the importance of this residue during the catalytic reaction. The stable conformation of NAD$^+$ obtained from MD is similar to the one in the X-ray structure of Sir2-Af1, where nicotinamide ring also faces towards the flexible loop (see Figure 31, 16).
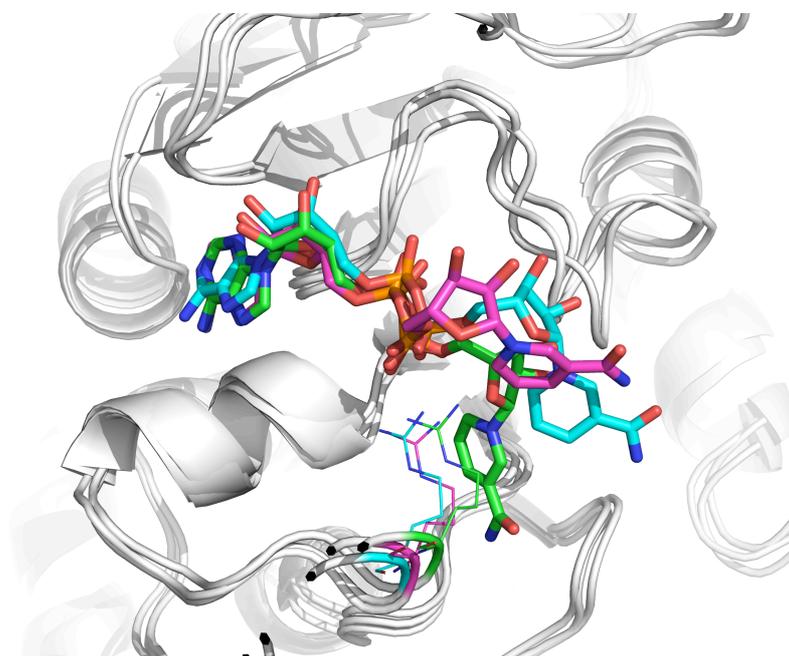
Figure 30: After 5 ns of MD simulation, the nicotinamide moiety is moving out of the C-subpocket NAD$^+$ starting structure in (green), after 5 ns (cyan) and after 7.5 ns (magenta).
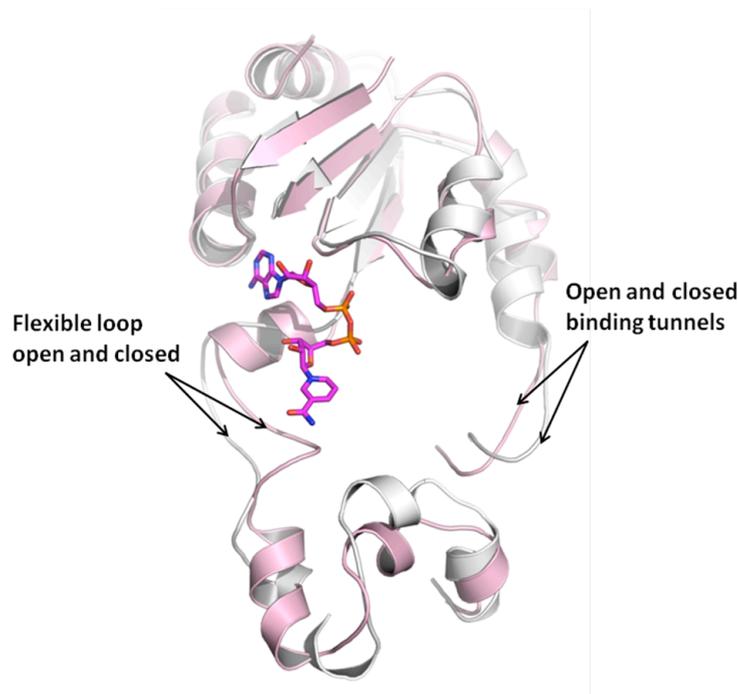
Figure 31: Comparison of complexed (pink) and unbound (white) human SIRT2 (conf. 2) after 12.5 ns of MD simulation Figure 29.

3.3.2 Hydrogen Bond Analysis

A comprehensive hydrogen bond analysis was done on the trajectory of the simulation of NAD^+ complexed SIRT2. Waston-Crick base pair formation and intermolecular receptor-ligand interactions contributing to the specificity of binding were characterized as an alternative to thermodynamic computations by hydrogen bond formation. A solvation pattern for bound NAD^+ was also characterized for conf. 1 between 6.0-9.0 ns and for conf. 2 between 12.5-15.0 ns simulation during which all water molecules are thought to be pre-equilibrated. A cut-off distance of up to 3 Å between the heavy atoms of donor and acceptor groups and a hydrogen bonding angle up to 120° was used to analyse hydrogen bond formations. Intermolecular hydrogen bond formations between human Sir2 and NAD^+ are listed in Table 3 and 4. As can be seen, for both conformations the same residues were found to be important in the MD simulation. It seems that the most essential hydrogen bonds contributing to binding exist between the phosphate oxygens of NAD^+ and O1 of Ser263 with 85.70% occurrence and to a lesser extent Thr262 with 4.74% occurrence. Gly30 makes also a key hydrogen bond to the N3 of NAD^+ (Figure 32) with an occurrence 13.75%. In addition Gly30 is one of the conserved residues among all Sir2 family members. In general NAD^+ makes hydrogen-bonding contacts with the adenine-ribose and diphosphate groups suggesting

the stability of these parts during MD simulation. Water molecules are presented near the nicotinamide and adenosine parts during MD simulations (Table 3, 4) similar finding can be also observed in the Sir2-Af1 (Figure 22). The N3-NAD atom forms multiple hydrogen bonds to Gly30 and to water molecules indicating the stability of the adenine-sirtuin interaction throughout the simulation.

Table 3: Occurrence of hydrogen bonds (%) for NAD$^+$-complexed SIRT2 conf. 1.

donor	Acceptor	occurence (%)	distance
NAD-O1	Ser263-OG	85.70	2.68
Gly30-O	NAD-N3	13.75	2.86
NAD-O2	Thr262-OG1	4.74	2.84
WAT	NAD-N3	19.11	3.00
WAT	NAD-N7	6.17	3.00
WAT	NAD-O12	5.43	2.78
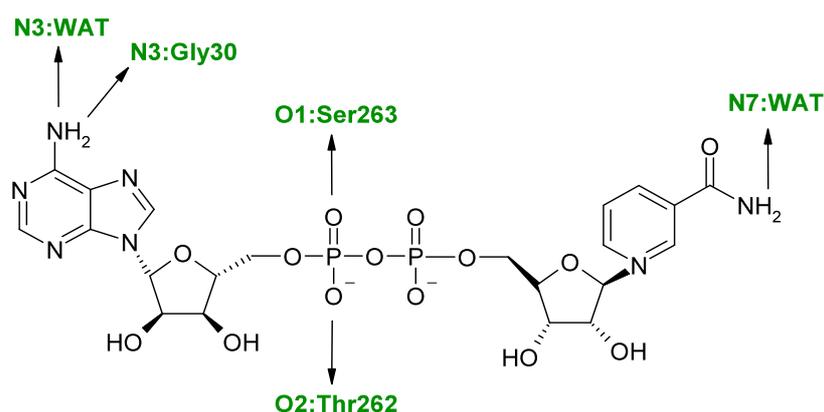
Figure 32: Schematic presentation of the most stable intermolecular hydrogen bonds between NAD$^+$ and human SIRT2.

Table 4: Occurrence of hydrogen bonds (%) for NAD$^+$-complexed SIRT2 conf. 2

donor	acceptor	occurence (%)	distance
NAD-O1	Ser263-HG	81.74	2.68
Gly30-O	NAD-N3	6.17	2.89
NAD-O2	Thr262-OG1	3.85	2.86
WAT	NAD-N3	23.47	2.99
WAT	NAD-N7	3.83	3.00

3.4 Thermodynamic Properties of NAD$^+$ Bound SIRT2

The binding free energies were estimated using the MM-PBSA method as described in chapter 2. Table 5 lists the contributions to the binding free energy calculated from the MD trajectories. As it can be seen the binding affinities for both NAD$^+$ conformations are favorable and very close to each other (-13.23 kcal/mol and - 13.91 kcal/mol). According to the energy components of the binding free energy (Table 5), van der Waals and electrostatic terms in the gas phase provide the major favorable contributions to the ligand binding. Non-polar solvation energies, also contribute slightly favorably. In the presence of NAD$^+$ conf. 1 the electrostatic interaction energy is favorable by -8.60 kcal/mol, but the electrostatic solvation energy is disfavorable by 16.30 kcal/mol which sum gives a disfavorable electrostatic contribution to the enthalpy of binding by 7.70 kcal/mol. Comparing the disfavorable electrostatic interactions in the bound state and the van der Waals interaction energy shows that the binding process is driven mainly by van der Waals forces in solution for conf. 1. A different situation can be seen for conf. 2, where the electrostatic interactions seem to drive the binding process.

The total entropy term, TΔS_{tot}, presented in (Table 5) corresponds to a binding entropy term and is a product of temperature (T) at 300K and the total entropy change which arises from changes in translational (ΔS_{trans}), rotational (ΔS_{rot}) and vibrational (ΔS_{vib}) degrees of freedom upon binding. It appears that the binding process of NAD$^+$ is enthalpy driven, as the disfavorable entropy term remains insufficient to counterbalance the favorable enthalpy effect in both cases.

Table 5: MM-PBSA binding energies given in kcal/mol. ΔE_{ele} and ΔE_{vdw}, are the electrostatic and van der Waals energies of binding, respectively, ΔE_{GBSA} is the solvation energy, ΔH_{tot} presents enthalpy of binding and ΔS_{tot} entropy of binding and is a product of translational (ΔS_{trans}), rotational (ΔS_{rot}), and vibrational (ΔS_{vib}) entropy changes.

SIRT2 NAD$^+$	ΔE_{ele}	ΔE_{vdw}	ΔG_{el}	ΔG_{nonel}	ΔE_{GBSA}	ΔH_{tot}	ΔS_{tot}	ΔG_{calc}
conf. 1	-8.60	-47.91	16.30	-6.59	18.30	-38.21	-24.98	-13.23
conf. 2	-78.62	-47.87	17.67	-6.63	89.66	-36.82	-22.91	-13.91

3.4.1 Single Step Mutation NAD$^+$ to Acetylated ADPR

The proposed sirtuins reaction mechanism indicates that the acetylated ADPR is the leaving product [55-57]. Thus, 100 snapshots of NAD$^+$ in conf. 1 were taken and mutated to acetylated ADPR by modifying the nicotinamide group. After that, using the MM-PBSA approach, the binding free energy was recalculated. Obtained energies for single-structure-based (SSB) acetylated ADPR are presented in Table 6. However, to address more reliability of binding free energy calculations and for comparison, a complete MD simulation was carried out for human SIRT2 in complex with acetylated ADPR. Obtained energies from both types of calculations are similar, suggesting that the SSB method could be sufficient for quantitative analysis. The binding free energies for acetylated ADPR are -4.76 kcal/mol and -4.00 kcal/mol (Table 6 and 7), which is in agreement with the suggested sirtuin reaction mechanism. The binding energy of NAD$^+$ for the two favoured conformations is about -13 kcal/mol. The less favourable energy of acetylated ADPR could be the reason why the acetylated product can easily leave the binding site and then the next NAD$^+$ molecule is able to enter the binding site.
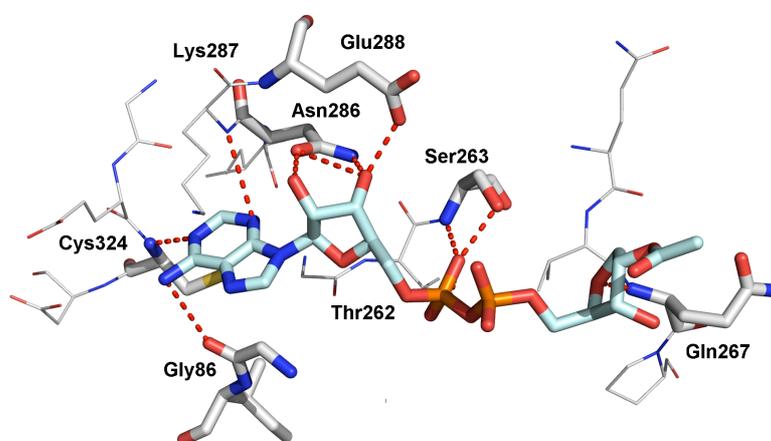
Figure 33: The mutated acetylated ADPR (light blue) is thought to be the leaving product of NAD$^+$. Hydrogen bonds are shown as dashed line.

Table 6: Components of the binding free energy of the acetylated-ADPR (modified from NAD$^+$ conf. 1, Figure 28).

	ΔE_{ele}	ΔE_{vdw}	ΔE_{GBSA}	ΔH_{tot}	ΔS_{tot}	ΔG_{calc}
SIRT2- Acetylated ADPR (single point calculations)	91.17	-41.82	-81.38	-32.03	-27.27	-4.76

3.4.2 Dynamical Behaviour of Human SIRT2 in Complex with Acetylated ADPR

As the results from single trajectory mutations may not be sufficient for the detailed analysis of ligand protein interactions. Thus, in the second step complete MD simulations were run for human SIRT2 in complex with acetylated ADPR. The MD simulation was set up using the same protocol as for NAD$^+$. The RMSD were calculated from the trajectories with the initial structures as the reference. As can be seen in Figure 34 the human SIRT2 protein (black) is stable and oscillates around 3 Å throughout 10 ns of the simulation. The acetylated ADPR shows more degree of flexibility; from about 3.7 ns to 6.2 ns the acetylated ribose group slowly leaves the nicotinamide binding pocket and reaches RMSD value of 3.7 Å (Figure 34, 35). Beyond 7.5 ns acetylated ADPR reaches its equilibration point and this steady state is maintained with less than 3.5 Å during the rest simulation time. Interestingly, the final stable position of acetylated ADPR is exactly corresponding to that of NAD$^+$ in conf. 1 found in the free MD simulation (Figure 24, 25 and 26). In both cases the ligands reached equilibration state around 7 ns whereas the NAD$^+$ in conf. 2 (Figure 29 and 30) needed more simulation time. Visual inspection of the trajectory showed that the ADP part is positioned deeply in the Rossman fold, whereas the acetylated ribose group oscillates between the nicotinamide subpocket and acetyl-lysine binding tunnel (Figure 35). Moreover during the simulations the flexible loop closed the nicotinamide subpocket (Figure 36, blue).
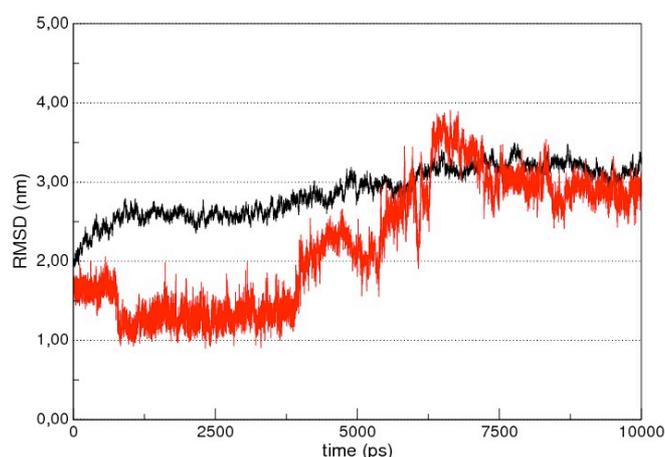
Figure 34: RMSD plot representing bound human SIRT2 (black) and bound acetylated ADPR (red).
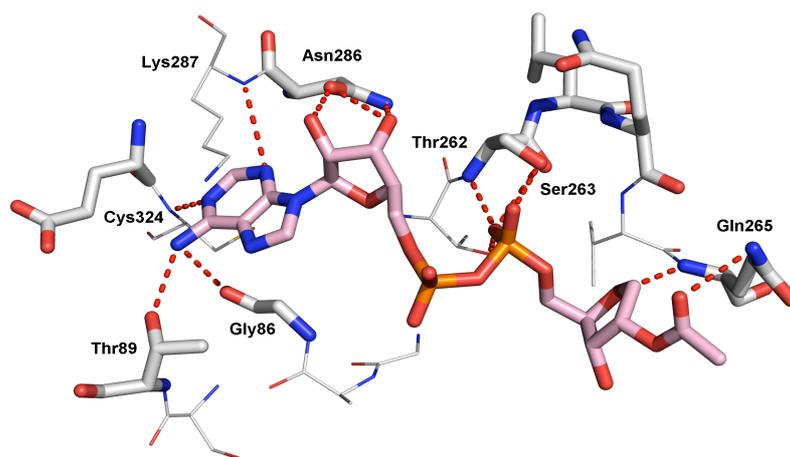
Figure 35. Stable position of acetylated ADPR (pink) at the end of 10 ns of MD simulation. Hydrogen bonds are shown in dashed lines.
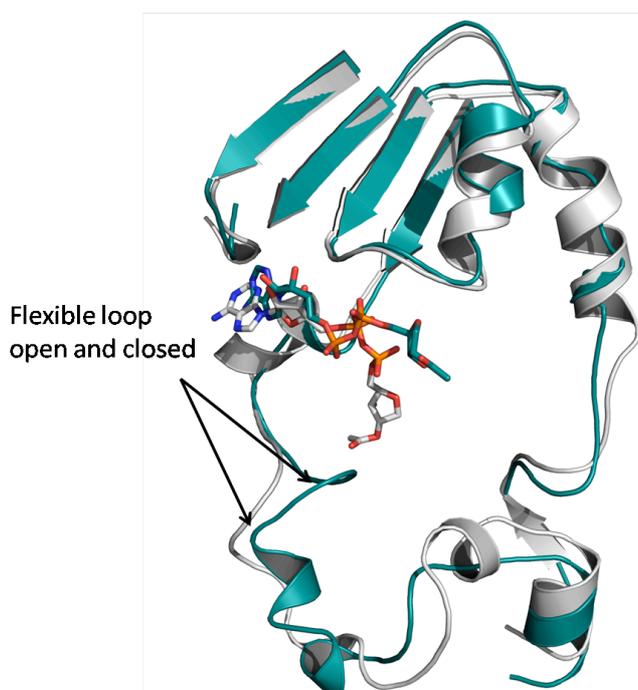
Figure 36: Human SIRT2 complexed with acetylated ADPR at the beginning (white) and at the end of the MD simulation (blue).

A hydrogen bond analyses was carried out on the trajectory of the human SIRT2-acetylated ADPR complex. A cut off distance of 3 Å was used and a hydrogen-bonding angle cut off of 120° was used. As can be seen from the complexes with different NAD^{+} conformation, the crucial interactions are the hydrogen bonds between the ligands and the Ser263, Thr262, and Gly30. In the case of the acetylated ADPR, also Ser263, Thr262 and Gly30 make the strongest hydrogen bonds with occupancies of 41.43%, 40.65% and 9.34% respectively. A solvation pattern was found for acetylated ADPR: N3 with the occupancy of 7.36%.

Table 7: Components of the binding free energy of acetylated-ADPR.

	ΔE_{ele}	ΔE_{vdw}	ΔE_{GBSA}	ΔH_{tot}	ΔS_{tot}	ΔG_{calc}
SIRT2- Acetylated ADPR (Complete MD calculations)	76.88	-48.87	-56.61	-28.60	-24.60	-4.00

3.5 Conclusion

Applying docking procedures, two different binding modes of NAD^+ at human SIRT2 were obtained. In both conformations the ADP part of NAD^+ interacts with the Rossman fold domain whereas the nicotinamide-ribose part adopts a variety of different conformations (Figure 17). In the first conformation (conf. 1) the nicotinamide ring lies outside the binding pocket, while for conf. 2 the nicotinamide is buried in the conserved C-pocket (Figure 17, 18 and 19). Also quite interesting is the position of the n-ribose: in first case it adopts a conformation that allows making hydrogen bond with Ile169 (Figure 18). In the second conformation, n-ribose forms hydrogen bond with His187 (Figure 19). The same interaction with the corresponding residue His116 is found in the X-ray structure of Sir2-Af1 (Figure 22). Different positions of the nicotinamide-ribose part have been observed in other Sir2-like proteins e.g. Si2-Af1, Sir2-Af2 in complex with NAD^+ and in SirTm in ternary complex with NAD^+ and peptide substrate analog [174-177].

In the second step MD simulations were performed in the presence and absence of NAD^+. The aim was to check the impact of ligand binding. The RMSD values of the complexes, compared to their starting points were monitored and only those conformations in which the ligand exhibited a stable binding position were considered for further analysis. During the MD simulation it has been observed that the adenosine and phosphate part remained stable bound to the Rossman fold domain. This suggests that the observed hydrogen bonds are relevant for keeping this part of NAD^+ stable during the catalytic reaction. On the other hand the nicotinamide-ribose part was quite flexible during the MD and adopted a number of different conformations. Interestingly, these NAD^+ conformations were also observed in other Sir2-like protein crystal structures e.g. Sir2-Af2 and Sir2-Af1 in complex with NAD^+. The conf. 2 (Figure 17, 19) of NAD^+ observed at the end of the MD simulations adopted an identical conformation as observed in the crystal structure of Sir2-Af1 (Figure 21). In case of conf. 1, where the nicotinamide-ribose part sticks out of the binding pocket (Figure 20) structural similarity was observed with the NAD^+ conformation from the Sir2-Af2 X-ray structure. Overall, in both cases the nicotinamide and n-ribose moiety rotate during MD and

adopt different conformations which are also observed in Sirt2-like proteins in complex with NAD$^+$. The MD simulations of the free and complexed human SIRT2 showed also a conformational transition of the flexible loop and substrate binding tunnel from an open to a more closed conformation (Figure 27, 31). These observed movements of the flexible loop can be deduced from different conformations that this loop can adopt (observed in the crystal structures of Sir2-Af1, Sir2-Af2 and Hst2. (Figure 15, 16). It can be also seen that in sirtuins co-crystallized with NAD$^+$ the flexible loop is "closing" the binding pocket (Figure 31). The same behavior was observed during the MD simulation of human Sirt2-NAD$^+$ complex.

An inspection of the H-bonds between NAD$^+$ (conf. 1 and conf. 2) and SIRT2 showed that the N3: NAD$^+$ makes strong interactions to the Gly30, as well as the O1, and O2: NAD$^+$ to the Ser263 and Thr262. These residues fix the adenosine phosphate part of NAD$^+$. Similar interactions were found in the X-ray structures of Sir2 in complex with NAD$^+$ or ADP-ribose. In Sir2-Af2 Glu29 interacts with N3: NAD$^+$, in Sir2-Af1 Glu26 forms hydrogen bonds to the same atom (Figure 20, 22). Similar interactions to Thr262 and Ser263 can be observed in the Sir2-Af1 X-ray structure (Figure 22). Additionally, water molecules are presented nearby the adenine and nicotinamide pocket, which were also observed in the sirtuin crystal structures e.g. Sir2-Af2 (Figure 20).

MM-PBSA calculations were applied to investigate the stability of the NAD$^+$ binding mode and the binding mechanism. Obtained binding affinities for the two NAD$^+$ conformations were quite similar (-13.23 and -13.91 kcal/mol for conf. 1 and conf. 2 respectively, Table 5). In addition, the cofactor structures in all derived snapshots were modified acetylated-ADPR (leaving product) and binding free energies were recalculated. As it can be seen in Table 6, the energies are much lower around ≈5 kcal/mol, suggesting that the acetylated ADPR can easier leave the human SIRT2 binding pocket and make place for the next NAD$^+$ to come in. However to address more reliability of binding free energy calculations, complete MD simulations for human SIRT2 in complex with acetylated ADPR were performed. The obtained results were analyzed and binding free energy was calculated using MM-PBSA method. The binding energy obtained from single structure based (SSB) method appeared to be similar to the value obtained from the standard MM-PBSA calculations. These suggest that the SSB approach would be sufficient for analysis in this case.

Chapter 4

4. Splitomicin Derivatives as SIRT2 Inhibitors

Bedalov *et al.* identified splitomicin (**1a**) (Figure 37) as an inhibitor of Sir2p and HST1 in a cell-based screen in *Saccharomycese cerevisiae* that abrogate telomeric silencing [85]. For examination of the potential binding site of Splitomicin, Sir2p was mutated in the domain near the peptide substrate binding-site. Such mutants were resistant to the antisilencing effects of splitomicin. Based on these results splitomicin seems to inhibit yeast sirtuins by preventing the access of the acetylated peptide substrate to the corresponding binding site. A first potent inhibitor of human subtypes based on the splitomicin scaffold was a α-phenyl splitomicin derivative with a bromo substituent in 8-position (HR73 (**1b**) Figure 37), which inhibits SIRT1 with an IC_{50} vaule of 5μM. A significant decrease of HIV transcription was shown with this compound in the cell culture model due to an interfence with the reversible acetylation of the viral TAT-protein [80]. In order to investigate structure activity relationships a series of different β-splitomicines like (**1b**) (Figure 37) were prepared and tested. The work resulted in identification of SIRT2 inhibitors active in the low micromolar range. Compounds **8c** and **8a,** with IC_{50} values of 1.5 and 6.4 μM respectively were the most active inhibitors in the set (Figure 38 Table 8).

1a: R1=H; R2=H
1b: R1=Br; R2=phenyl
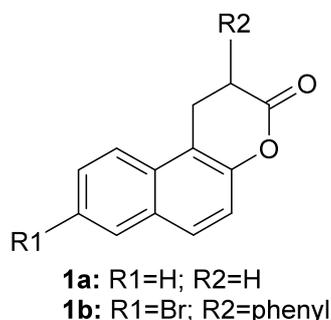
Figure 37: Splitomicin Sir2 inhibitors.
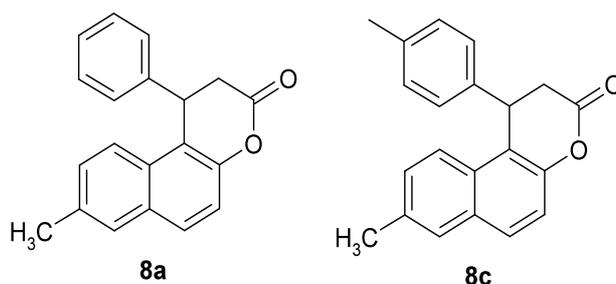
Figure 38: The most active β-phenyl splitomicins in the set.

Table 8: Biological data for the most active β-phenyl splitomicin derivatives **8a** and **8c**.

comp.	substitution	SIRT2 (IC$_{50}$ ± SE or inhibition at concentration, μM)
8a	R1:Ph	6.4±0.3
8c	R1:4-MePh	1.5±0.3
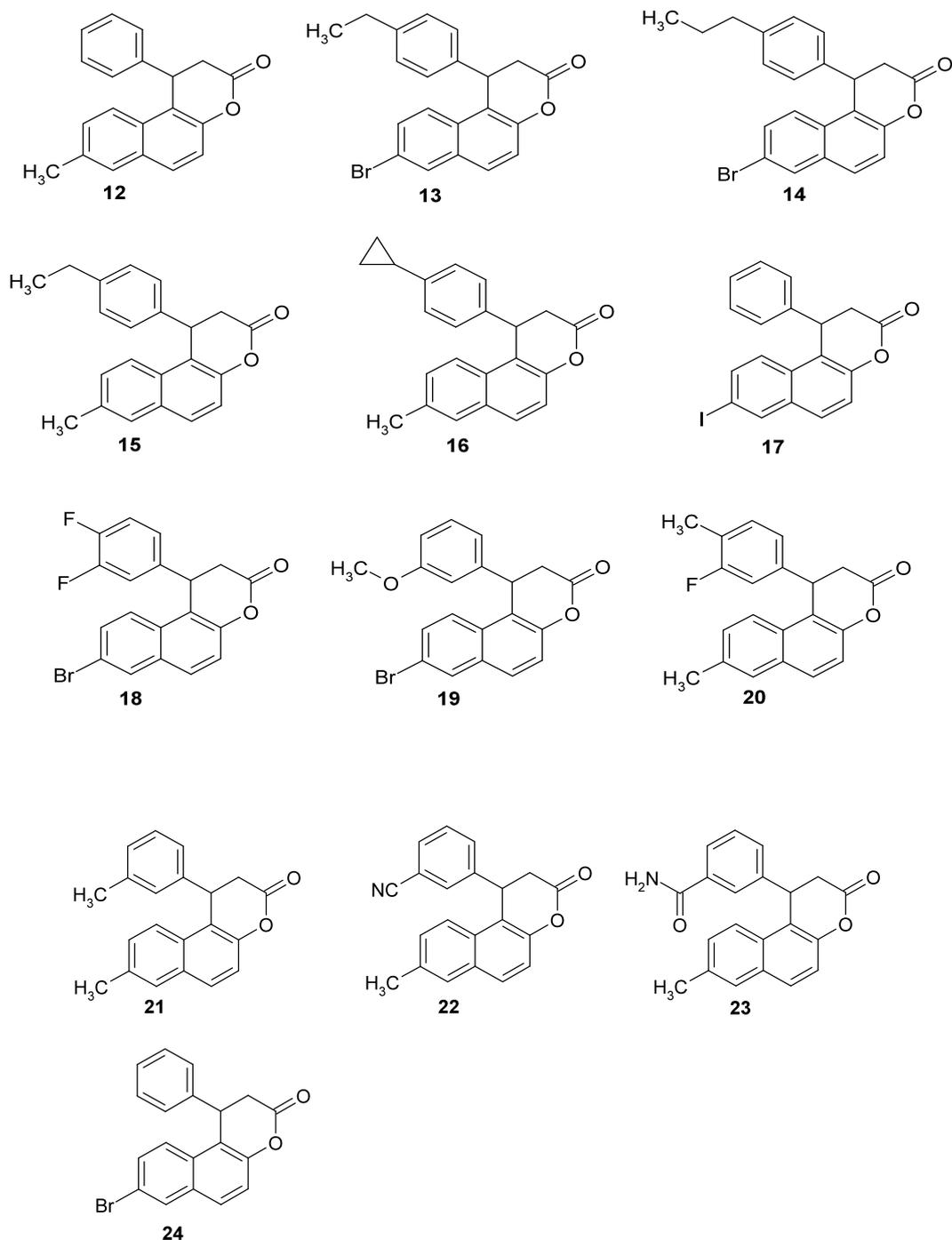
Figure 39: Series of β-aryl-8-bromosplitomicins.

4.1 Docking Studies

In our previous studies we described the analysis and development of SIRT2 inhibitors, including adenosine mimetics and suramin derivatives [81]. Based on the docking studies that we carried out for human SIRT2 and competition experiments with NAD$^+$, we found that these compounds interact with the adenine and the nicotinamide subpocket (suramin) respectively. Due to the structural dissimilarity between these inhibitors and the splitomicins, it can be expected that they interact in a different way with sirtuin proteins. In docking studies, the X-ray structure of human SIRT2 was used for an automated ligand docking using the program GOLD [109]. The analysis of the X-ray structure of human SIRT2 and preliminary docking simulations using the known inhibitors cambinol and indole (Figure 10, 40 and 41) showed that these compounds interact with the nicotinamide subpocket (C) of SIRT2. The consideration of four water molecules found in all SIRT2 X-ray structures, which are located at a narrow cavity nearby the active site, significantly improved the docking results. The polar moieties of known inhibitors such as cambinol (Figure 40) were found to interact with the polar residues Gln167, Asn168 and the water molecules of the nicotinamide subpocket.
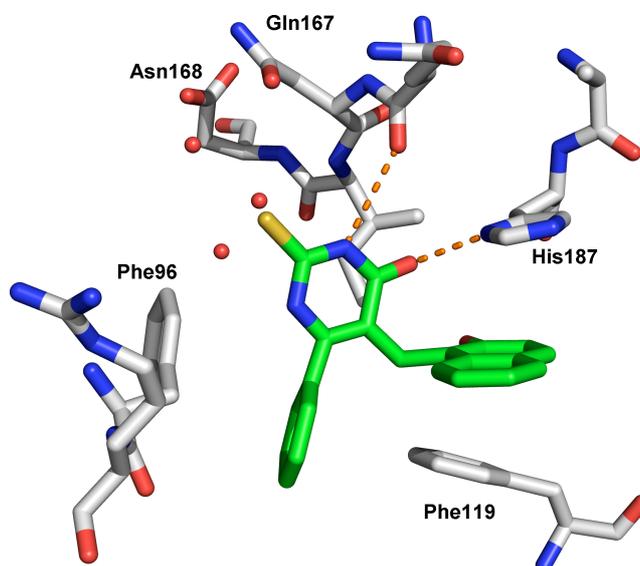
Figure 40: Predicted binding mode of cambinol at the nicotinamide-binding site of human SIRT2. The conserved water molecules are displayed as red balls. Hydrogen bonds are indicated by dashed lines.
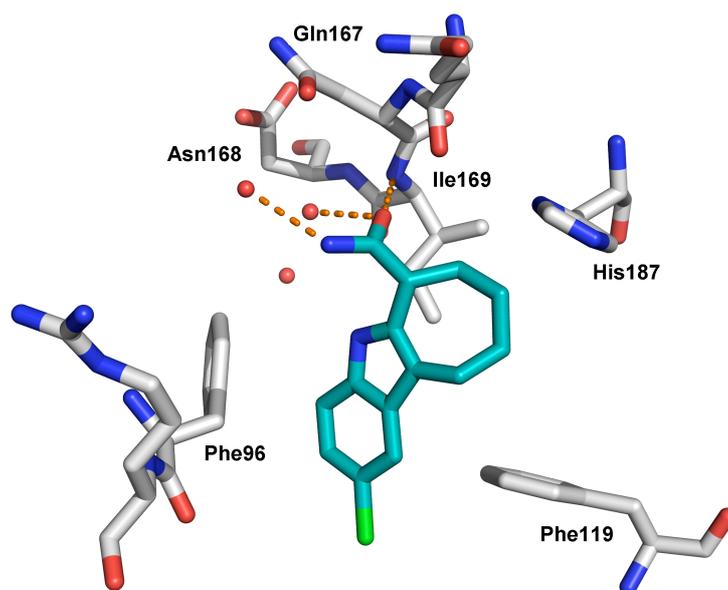
Figure 41: Predicted binding mode of indole (Figure 10, comp.14) at the nicotinamide-binding site of human SIRT2. The water molecules used in the docking study are displayed as balls. The dashed lines indicate hydrogen bonds.

A series of docking simulations were carried out to better understand the binding of the splitomicin derivatives. For docking studies we considered crystal water molecules. Visual analysis of obtained docking poses revealed that all docked *β*-phenyl splitomicins showed the same binding mode including a hydrogen bond to the water molecule bonded to Gln167 (Figure 45, 42). The *β*-phenylsplitomicins at first were prepared and tested as racemates, but we considered both stereoisomers (*R* and *S*) in the docking study. The obtained docking scores and visual analysis of the docking poses showed that only the *R*-isomer is able to favourably interact with the nicotinamide subpocket (Figure 42 and 43). The *β*-phenyl substituent of all *R*-isomers fits into a hydrophobic channel and is sandwiched between Phe119 and His187 (Figure 42). This channel represents the binding site for the acetylated lysine residue of the substrate. For the *S*-enantiomers, the docking showed that the lactone ring is also facing toward the nictoinamide subpocket. However, no direct hydrogen bond was observed between (*S*)-8a and the residues of active site (Figure 43). Our proposed type of interaction of (*R*)-8a and (*R*)-8c with SIRT2 is similar to docking results published for other SIRT2 inhibitors [82]. Also, in these studies, the polar moieties of inhibitors were found to interact with the nicotinamide binding pocket C (Phe96, Gln167, Asn168 and Ile169).

The docking study and the visual inspection of the interaction possibilities clearly suggested that the *R*-enantiomers represent the active form of the *β*-phenylsplitomicins, whereas for the

S-enantimers, no clear binding mode was observed. After docking studies the *R*- and *S*-enantiomers were synthesized and tested, we observed that the *R*-enantiomer exhibited similar activity as the racemic mixture, whereas the *S*-enantiomes displayed only weak SIRT2 inhibition (Table 9).

Table 9: Biological data for the enantiomers of **8a** and **8c** (Figure 38).

comp	substitution	SIRT2 (IC$_{50}$ ± SE or inhibition at concentration, μM)
(R)-8a	R1:Ph	3.4±0.2
(S)-8a	R1:Ph	inactive
(R)-8c	R1:4-MePh	1.0±0.3
(S)-8c	R1:4-MePh	inactive

In the next step, we analyzed the obtained docking scores for all studied inhibitors. In the case of the enantiomers (*R*)-8a, (*S*)-8a and (*S*)-8c, higher scores were observed for the *R*-species. The docking results showed that the active inhibitors interact in similar ways with the adenine-binding pocket. However, on the basis of the Goldscore values, no discrimination could be derived between more and less active splitomicin inhibitors. It was shown in many docking studies that often a low correlation is observed between docking scores and biological activities [178].
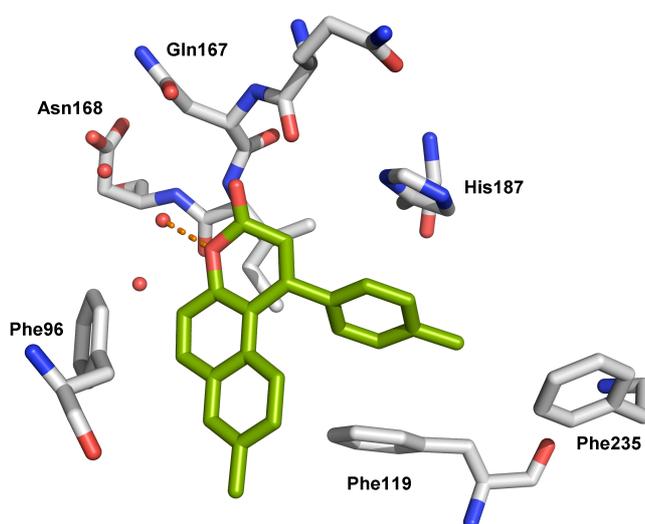
Figure 42: Docking solution for the active *R*-enantiomer of the *β*-phenylsplitomicins (green). Crystal water molecules are coloured in red, hydrogen bond is shown as dashed line.
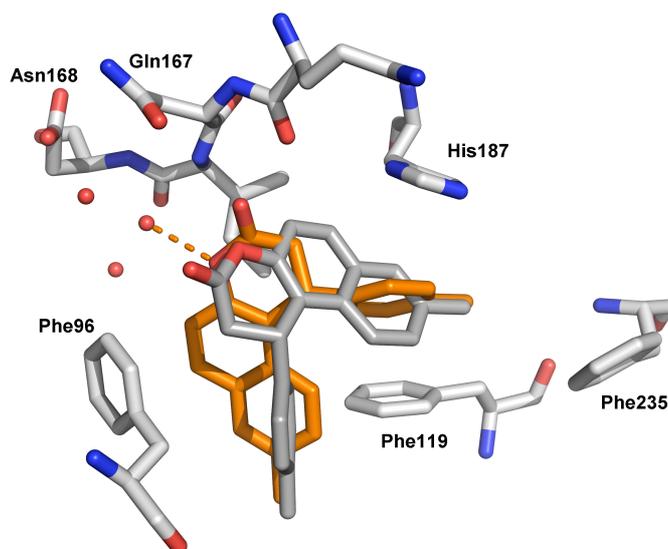
Figure 43: *R*-(orange) and *S*-(grey) isomer docked into SIRT2 binding pocket. Crystal water molecules are coloured in red. Hydrogen bond is shown as dashed line.
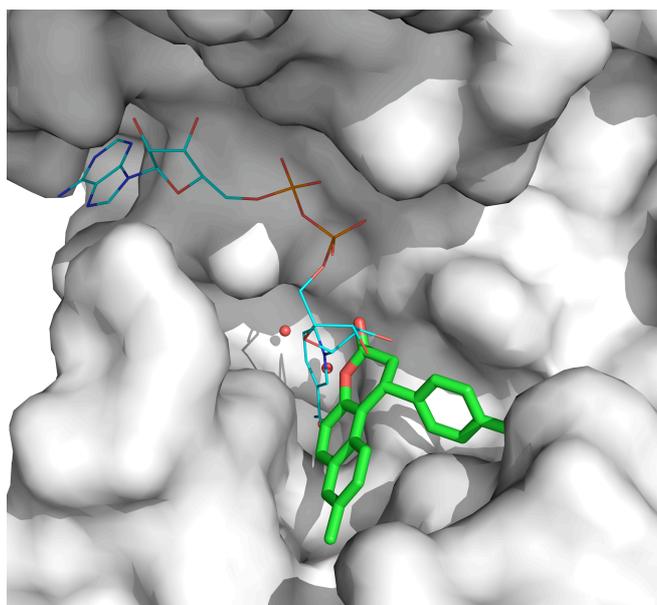
Figure 44: Docked *R* isomer of the active splitomicin to the nicotinamide subpocket of human SIRT2. The position of NAD is shown in comparison in cyan.

The docking results of splitomicin derivatives with substituents at the 3- and 4-positions of the β-phenyl group showed that the phenyl ring is located at the entrance of the acetyllysine substrate channel. Therefore, we suggested that the addition of a hydrophobic substituent at the 4-position of the β-phenylsplitomicins would increase the inhibitory potency. The subsequent synthesis and biological testing (Table 8, Figure 48) showed that the presence of an ethyl group at the 4-position results in the most potent inhibitor of this series. Bulkier

hydrophobic groups at the 4-positon or polar groups at the 3-position resulted in a decrease in the inhibitory activity [179].

Interaction possibilities at the binding pockets were analyzed by calculating the contact preferences using the MOE program [180]. The purpose of this knowledge-based approach is to calculate preferred locations for hydrophobic ligand atoms from the 3D coordinates of the binding site. The visual analysis of the contact preferences further supported the binding mode obtained by the GOLD [109] docking (Figure 45). The most favourable interaction with hydrophobic ligand atoms was observed in the acetyl-lysine channel and nearby the Tyr104 and Val233 residues. The favoured polar interactions were detected nearby the polar residues Gln167 and Asn168, which are in agreement with the location of the water molecules.
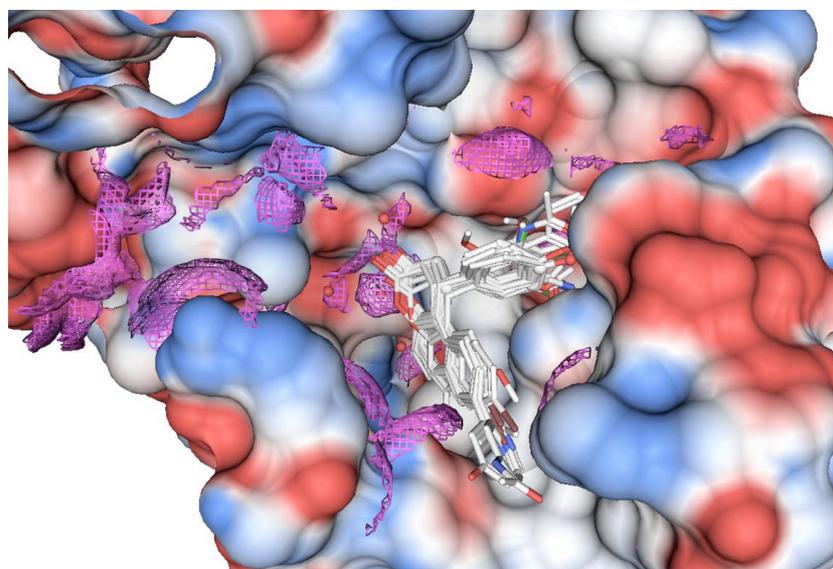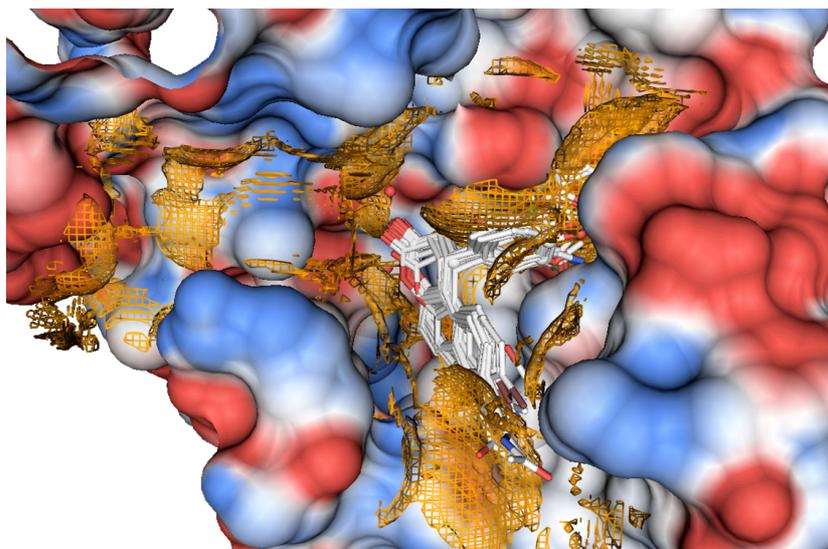
Figure 45: Interaction possibilities at the binding pocket, as analyzed by calculating the contact preferences using the MOE program. The docked inhibitors (*R*-enantiomers) are coloured atom type coded. The Connolly molecular surface of the binding pocket is coloured according the electrostical potential (blue=positive potential, red=negative potential). The favourable hydrophilic contact preferences (contour level 90%) are coloured magenta. The favourable hydrophobic contact preferences are coloured orange.

4.2 Molecular Dynamics Simulations

The MD simulations of the SIRT2-inhibitor complexes were performed in total for 6 ns. Finally, root-mean-square deviation (RMSD) was computed from the trajectory relative to the initial structures to judge the stabilization of the complexes. The RMSD plot for *R*-enantiomer (Figure 46), clearly shows that **8c** compound reaches an equilibrium state beyond 2000 ps of MD and this state is maintained throughout the simulation with less than 2 Å RMSD as referenced to the crystal structure coordinates. As shown in Figure 46 the RMSD jumps at 2 ns, which is probably attributed to a dispositioning of the lactam ring. The flexibility of the β-phenyl substituent is lower and during simulations slightly oscillates in the entrance of the acetyl lysine pocket. The overall structure of bound *R*-isomer remains stable with less than 3.5 Å. The superposition of the X-ray structure and an average structure taken from the last ns of MD simulations showed that the Gln167 and His 187 play a major role in the formation and stabilization (Figure 47). Both residues form quite strong hydrogen bonds to the ligand during MD simulation see section 4.2.1.
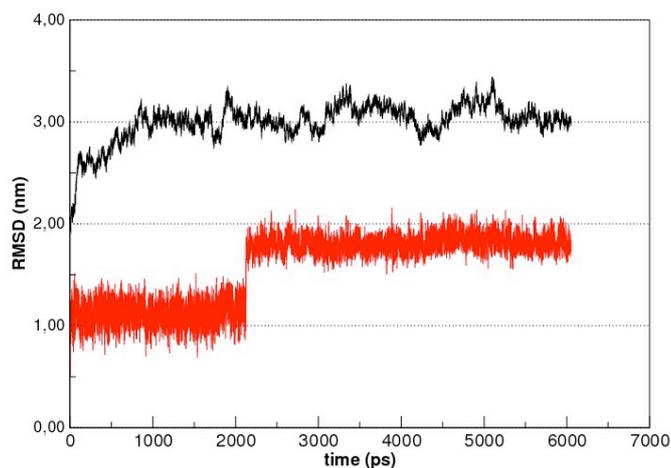
Figure 46: Root mean square deviation (RMSD) plot representing h-SIRT2 (black) and β-phenylsplitomicin *R*-(8c).
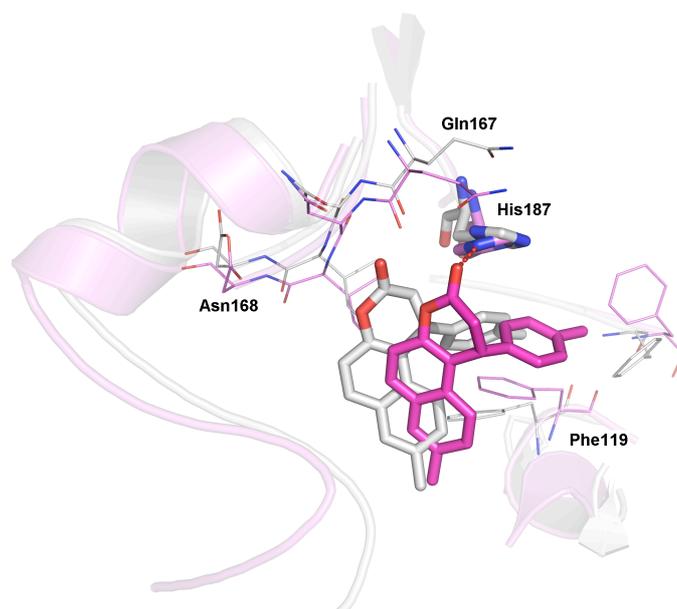
Figure 47: Superposition of the human SIRT2 with *R*-isomer 8c at the beginning of the MD simulations (white) and at the end (magenta).

The *S*-enantiomer reaches an equilibrium state beyond 3.5 ns of MD simulation and this steady state is maintained with less than 2 Å referenced to the starting coordinates (Figure 49). In this case on the RMSD plot two sharp peaks at 2500 ps and at 3500 ps are observed. Beyond 3.5 ns the *S*-enantiomer slightly shifts towards the entrance of the acetyl lysine pocket (hydrophobic pocket) and stays in this conformation for the rest of the simulations (Figure 48 and 49). Interestingly, also the two residues His187 and Gln167 are more flexible in the MD simulation of the complex with the *S*-isomer. Both residues slightly moved away from the ligand. Thus the *S*-isomer has more degree of flexibility during MD (Figure 48). Thus the *S*-

isomer needs more simulation time to reach the equilibration. Also, no hydrogen bonds were found for the *S*-isomer, which is in agreement with the docking study.
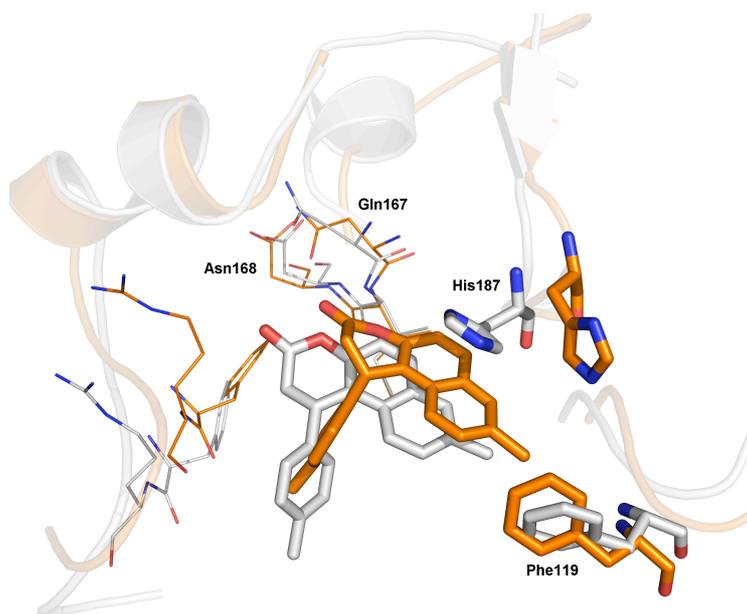
Figure 48: Superposition of the human SIRT2 with *S*-isomer **8c** at the beginning of the MD simulations (white) and at the end (orange).
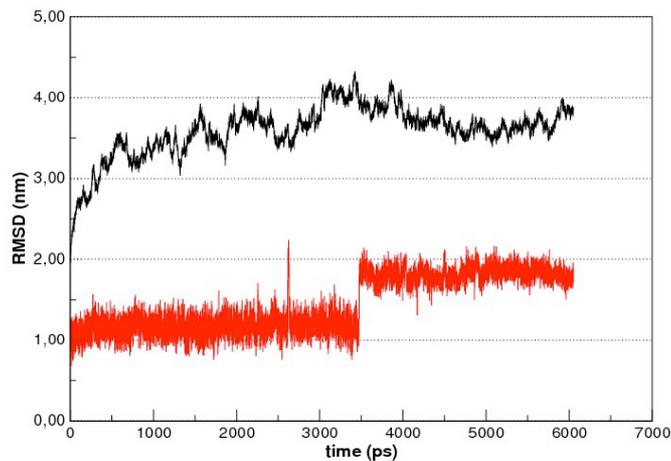
Figure 49: Root mean square deviation (RMSD) plot representing h-SIRT2 (black) and β-phenylsplitomicin *S*-(8c).

4.2.1 Hydrogen Bond Analysis

A comprehensive hydrogen bond analysis was carried out on the trajectory of the splitomicin-SIRT2 complexes. Protein inhibitor interactions were characterized by analysing hydrogen bond formations through the trajectory of the 6 ns simulation time. Also a solvation pattern

for bound isomers was calculated between 2 and 6 ns, where all water molecules are thought to be pre-equilibrated. A cut off distance of 3 Å between the heavy atoms of donor and acceptor groups, and a hydrogen bonding angle cut off of $120°$ was used to analyze hydrogen bond formation. Intermolecular hydrogen bond occurrence > 1% was only found for the *R*-isomer Gln167 2.85%, Ile169 4.23%, His185 3.25% and solvation pattern with 17.44% occurrence. For the *S*-isomer only a solvation pattern was found with an occurrence of 11.25%.

4.3 MM-PBSA Approach

The MD trajectories were further analyzed through the MM-PBSA approach [160]. In this method the absolute free energy of a system is estimated from a combination of molecular mechanics energy and Poisson-Boltzmann surface area. Because the inhibitors **8a** and **8c** were synthesized and tested as enantiomers, we focused our free energy calculations on this set of inhibitors. The estimated binding free energy for two pairs of stereoisomers shows (Table 10). The calculated mean binding free energies were -7.41 kcal/mol for (*R*)-8c and -4.73 kcal/mol for (*S*)-8c, respectively. Also for 8a the MM-PBSA calculation predicted the *R*-enantiomer to bind stronger to SIRT2 (*R*)-8a, -7.53 kcal/mol, and for (*S*)-8a, -2.70 kcal/mol. Thus, binding of (*R*)-8c is more favourable than for the *S*-enantiomer, whereas in case of 8a the energy difference is 4.65 kcal/mol. The estimated binding free energies are in good agreement with the biological data where the *S*-enantiomers are more than two log units less-active than the *R*-enantiomers (ΔG_{exp} > ~3 kcal/mol, calculated on the basis of the IC_{50} values measured at 310 K).

	SIRT2/*(R)*-**8c**	SIRT2/*(S)*-**8c**	SIRT2/*(R)*-**8a**	SIRT2/*(S)*-**8a**
ΔE_{ele}	-7.81	-3.22	-2.09	-0.19
ΔE_{vdW}	-30.87	-31.54	-38.68	-31.44
ΔE_{gas} (ΔE_{ele} + ΔE_{vdW})	-38.68	-34.76	-40.77	-31.63
ΔG_{solv}	9.77	10.74	7.63	5.66
$T\Delta S_{tot}$	-21.50	-19.29	-25.79	-23.27
ΔG_{calc}	-7.41	-4.73	-7.35	-2.70

Table 10: Energy contributions to the free energy of binding in (kcal/mol) obtained from MM-PBSA approach for R and S isomers.

4.4 Virtual Screening

We screened the Chembridge database for inhibitors related to the *β*-phenylsplitomicins. The compounds of the Chembridge databse were transformed into 3D molecular structures using the Omega module from OpenEye Software [181]. The ~328000 molecules were stored in a MOE database (Chemical Computing Group) and ESshape3D MOE fingerprints were calculated. The ESShape3D is a value spectrum shape fingerprint. Each fingerprint is a fixed length and allows for comparison of 3D shapes made from the heavy atoms of a molecule. Compounds similar to 8a (with an inverse distance >0.9) were retrieved and further analyzed. Among the retrieved compounds 17 lactam analogs of **8a** were identified. The lactams were docked into the human SIRT2 protein structure using the program GOLD. GoldScores were calculated for all docking poses that were subsequently visually analyzed within MOE. To confirm the virtual screening results, four lactam analogs of **8a** that showed a similar binding mode as the *β*-phenylsplitomicins were selected and purchased from Chembridge (Figure 50 and 51).

11a: R=H, X=CH
11b: R=F, X=CH
11c: R=H, X=N
11d: R=Ph, X=CH

12
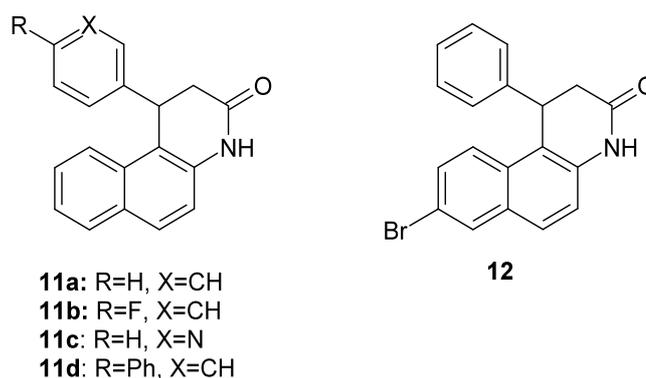
comp	SIRT2 (IC$_{50}$ ± SE or inhibition at concentration, µM)
11a	31.5% @ 40
11b	16.9 % @ 40
11c	No inhib. @ 20
11d	4.2 % @ 40
12	6.4 µM ± 0.3

Figure 50: Lactam analogues of splitomicin (**11a-d**) and bromo-substituated lactam analogue (**12**) found in the virtual screening.
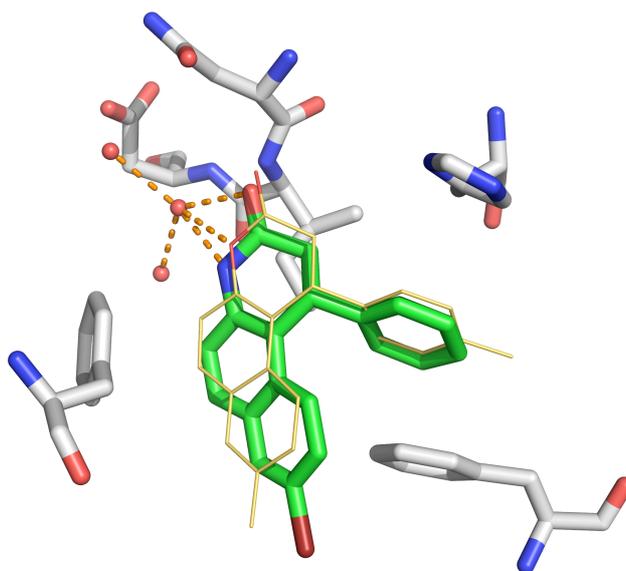
Figure 51: Human SIRT2 with docked lactam 12 (green) and splitomicin **8c** (yellow).

4.5 Conclusion

Structure-activity relationships for β-aryl splitomicins led to the identification of SIRT2 inhibitors that are active in the low micromolar region. A link between increased enzyme inhibition and anticancer activity could be established. This supports the use of our fluorescent small molecule in sirtuin assays to identify antiproliferative agents. Docking studies confirmed that in the whole series of β-phenylsplitomicines the orientation of the β-phenyl group is important for their SIRT2 activity. Only in the case of the *R*-enantiomers of the chiral inhibitors the interaction with the substrate binding channel is observed. The preparation and biological testing of two pairs of enantiomers confirmed the docking results and the MD simulations. Furthermore, we reported calculations of binding free energies between these two pairs of enantiomers and SIRT2 using the recently developed MM-PBSA method. This approach proved to be attractive for rationalizing at a quantitative manner the interaction of the splitomicines and SIRT2. The competition experiment carried out with NAD$^+$ clearly showed that the β-phenylsplitomicins are noncompetitive to the cofactor. The comparison of the predicted binding mode of *R*- (8a) and the observed interaction of NAD$^+$ in the homologues bacterial sirtuin X-ray structure complexes further supported the noncompetition between both molecules and is in agreement with recently published structural data on sirtuin homologues [71]. One of the limitations of splitomicins is the instability of the lactone ring, this lead to a short half-life particularly at physiological pH [80]. Therefore, we used Virtual Screening to discover more drug-like compounds. Similarity

based searching and subsequent docking the hits into the SIRT2 binding site gave us series of inhibitors where the lactone of β-phenylsplitomicine is replaced with the lactam ring, resulting in equally active inhibitors. The predicted binding mode of the lactam-based inhibitor **12** is shown in (Figure 51). Experimental analysis showed that lactam analogues are more stable and better water-soluble which makes them interesting for further development.

Chapter 5

5. Thiobarbiturates as Sirtuin Inhibitors

The purpose of this part of the study was to find new series of compounds that inhibit human sirtuins. We used an approach that combines the benefits of structure-based virtual screening and experimental testing with validated sirtuin inhibition assays to subsequently screen only a limited number of the top-ranking compounds. We performed a multi-step Virtual Screening experiment starting with a prefiltered compound library containing over 328 000 molecules and combination of similarity based screening and ligand docking. The virtual screening was followed by MD simulation and free-energy calculations applying the MM-PBSA [160] approach to get better estimate of the ligand binding free energy.

5.1 Virtual Screening

The Virtual Screening was carried out with the Chembridge database (Chembridge Corporation, San Diego, CA, USA) containing a library of ~328 000 compounds. We screened this database for inhibitors structurally related to cambinol (Figure 9, 40). The compounds of the databank were transformed into 3D molecular structures using Omega module from OpenEye Software [181]. The ~328 000 molecules were stored in a MOE databse and several physiochemical descriptors were applied: a) M_r between 250 and 400 b) log P < 5 c) TPSA < 150 Å, and at least one nitrogen atom. MACCS fingerprints were calculated for all compounds. Molecules similar to cambinol (with an inverse distance >0.7) were retrieved and further analyzed. The 390 compounds were docked into the SIRT2 protein structures as described above and using the GOLD program. GoldScores were calculated for all docking poses; 131 molecules were successfully docked into the nicotinamide binding pocket (showing a GoldScore between 30 and 62). The final selection of a small subset of compounds was based on visual inspection of the binding mode (only molecules showing hydrogen bond to Gln167 were considered) and on the lipophilicity of the compounds (lower log$P$ favored). The five compounds were purchased from Chembridge and tested in an in vitro assay [89] for their ability to inhibit human SIRT2 (Figure 52, Table11).
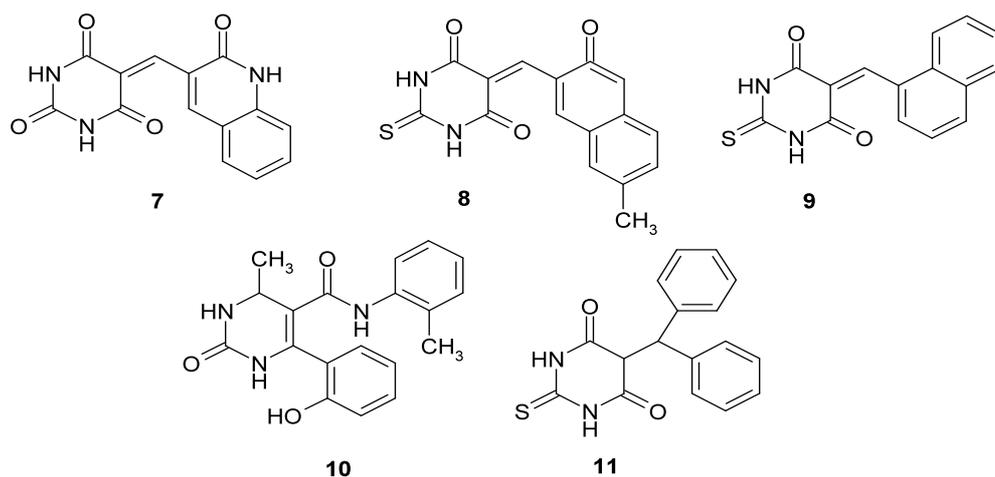
Figure 52: Molecular structures of the five hits from the Virtual Screening of the Chembridge database.

Table 11: Inhibition of SIRT2 by the hits from screening.

comp	SIRT2 IC$_{50}$±SE [µM]
7	61±3.5
8	11.3±1.7
9	9.1±5.8
10	130.7±47.2
11	40.7±3.9

5.2 Docking Studies

The interaction of the most potent compound **9** with human SIRT2 is shown in (Figure 53 and 54). A common feature of the active inhibitors is the interaction (hydrogen bond) of the barbiturate/thiobarbiturate NH group with the backbone carbonyl group of Gln167 and the hydrogen bond between the barbiturate CO group and Hist187. The bulky naphthyl or hydroxyquinoline substituent is directed into the acetyllysine substrate channel and undergoes van der Waals interactions with the aromatic ring system of Phe119 and His187. It can be seen that the binding mode of the novel thiobarbiturate inhibitors is similar to that observed for cambinol (Figure 40).
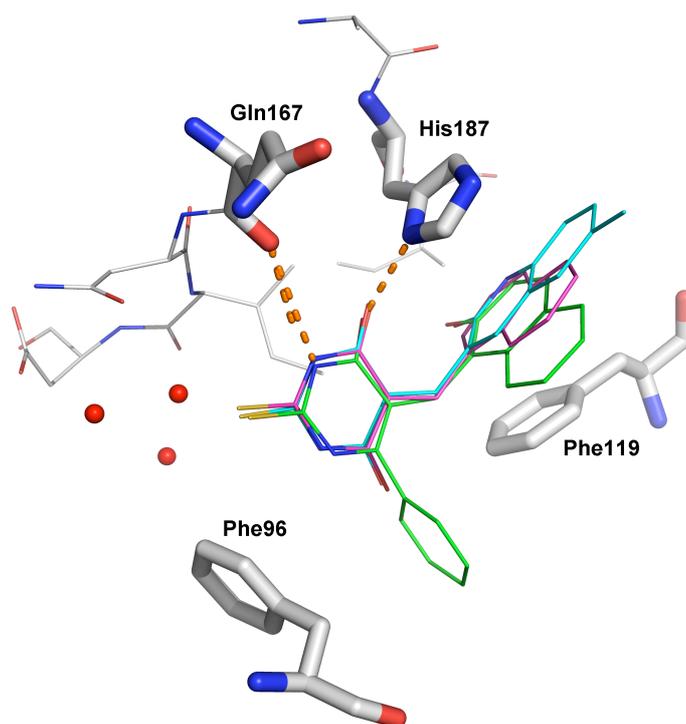
Figure 53: Comparison of the docking results obtained for **8** (cyan), **9** (magenta) and cambinol (green) at SIRT2. The four water molecules used in the docking study are displayed as balls. Hydrogen bonds are indicated by the dashed lined.

Compounds **7** and **8** can be present in two tautomeric forms (Figure 52). In the Chembridge database both molecules are stored as the hydroxyquinoline tautomer, which was also considered for the virtual screening study. We also generated the pyridine tautomer and docked it into the SIRT2 binding pocket. A similar binding mode was observed for the pyridine tautomer, placing the pyridine ring between the aromatic side chains of Phe119 and His187 (RMSD: 0.2 Å). Semi-empirical quantum mechanical calculations using the AM1 method were carried out to calculate the potential energies of two tautomers of **7** an **8** (Figure 52). Such calculations were performed in vacuo yielded an energetic preference for the pyryidyne tautomer, whereas the GoldScores were observed to be higher for the hydroxyquinoline tautomer. Similar results were derived with X-Score and Chemscore [109]. Based on the calculated docking poses and the corresponding scores, no final decision can be made as to which tautomer is more likely to interact with the SIRT2 active site.
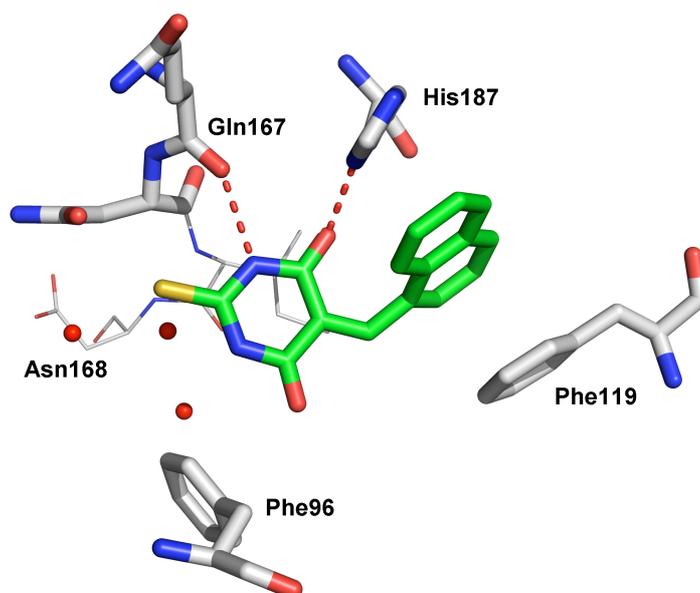
Figure 54: Predicted binding mode of **9** at the nicotinamide-binding site of human SIRT2. The water molecules used in the docking study are displayed as balls.

5.3 Molecular Dynamics Simulations

In this section we present analysis on selected two novel thiobarbiturates, compound **8** which showed the activity of 11.3 μM and, compound **10** with lower activity 130.7 μM. The thiobarbiturates compounds are similar to the cambinol inhibitor thus in the first step a complex of human SIRT2 with cambinol was calculated and analysed. To explore the effect on the dynamical stability of the human SIRT2-cambinol complex, the root-mean-square deviation (RMSD) values relative to the initial structures were calculated and plotted in (Figure 55). The RMSD for cambinol during MD is around ~1.5 Å (red) and stayed stable during the MD simulation, for the receptor the RMSD value is less than 4 Å (black) (Figure 55). The RMSD SIRT2 pattern exhibits one increasing point at 2 ns of the simulation, than the frequency of flexibility is getting lower to about ~3.5 Å and this state is maintained throughout the simulations. The constant RMSD value of cambinol, suggests that the binding mode is stable during the MD simulation (Figure 55 and 56).

Figure 56 presents a superimposition of the bound human SIRT2 before (white) and after (green) 4 ns of the MD simulation. As can be clearly seen, there are some additional conformational changes, which occur mainly in the flexible loop region and at the entrance of the acetyl-lysine pocket (see Figure 56). Based on a trajectory analysis we observed that when the ligand binds the loop slowly shifts towards the binding pocket (green) and make it

closed, suggesting that the loop regulate the stability of the ligand. Also the binding tunnel closes when cambinol is bound. Open and closed conformations we also observed during simulations of human SIRT2 with different NAD^+ conformation (3.3.1). A hydrogen bond analysis was carried out on the trajectory of the human SIRT2 cambinol complex. Hydrogen bond formation between the oxygen from thiobarbiturate ring and His187 was found with an occurrence of 10.51%.
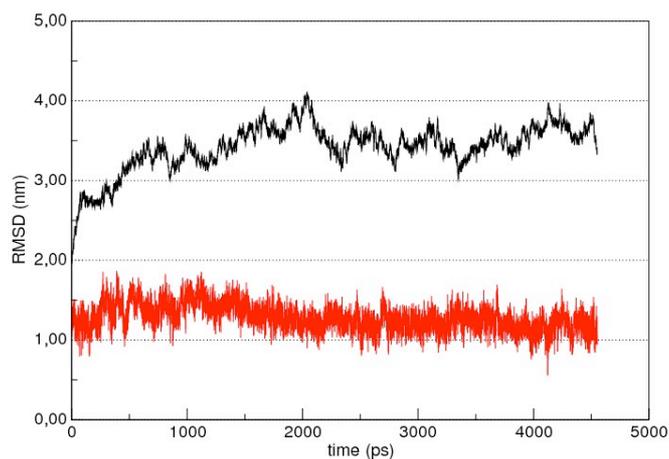
Figure 55: Root mean square deviation (RMSD) plot representing human SIRT2 (black) and bound compound 10 (red).
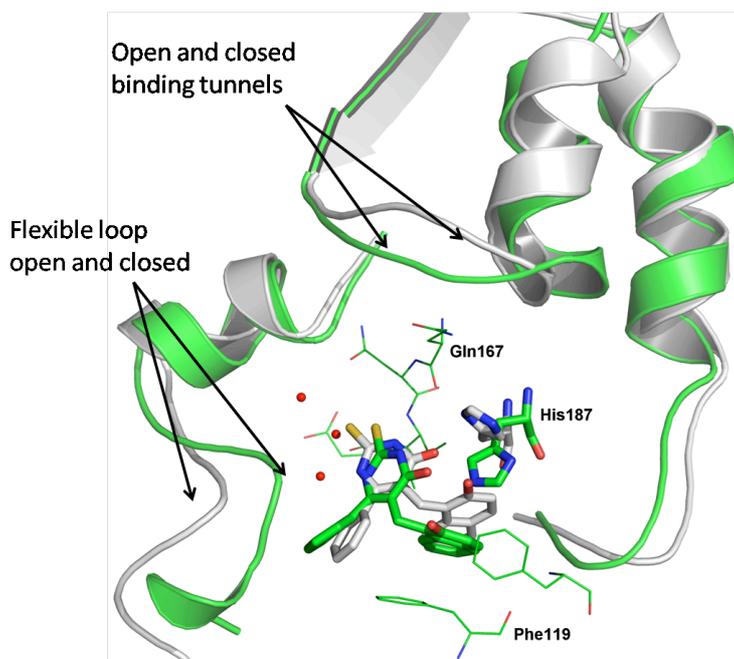
Figure 56: Superposition of the human SIRT2 in complex with cambinol at the beginning (white) and (green) at 5 ns of MD simulations. Water molecules in the binding pocket are shown as red balls.

67

The RMSD of two novel thiobarbiturates - compound **8** and compound **10** (Figure 58 and 60) - remained low (<2 Å) and did not vary significantly during 5 ns of MD simulations in reference to the starting coordinates. When the compound **8** binds to human SIRT2, the complex reaches is equilibration state beyond 2ns and then oscillates around 3.5 Å (Figure 58). In case of compound **10** (Figure 60), the overall structure remains stable around 3.5 Å. Analysis of the trajectories showed that Gln167 and His187 seem to play a major role in the formation and stabilization of the complex during the MD simulation (Figure 57, 58). Moreover visual inspection indicated that when the compounds **8** binds to the human SIRT2 the flexible loop shifted inside the binding pocket and interacts with the bound ligand (Figure 57), which is similar to what we observed for cambinol. However if the compound **10** with a much lower activity binds to the hSIRT2, we did not observe any loop flexibility - the binding pocket remained more open (Figure 59).
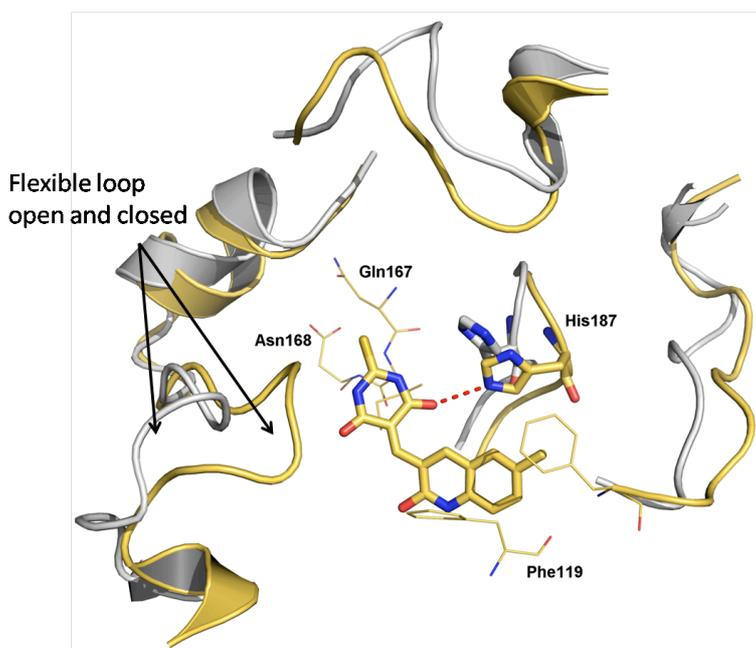
Figure 57: Superposition of the human SIRT2 in complex with a compound **8** (IC$_{50}$= 11.3 μM) at the beginning (white) and (yellow) of the 5ns MD simulation.
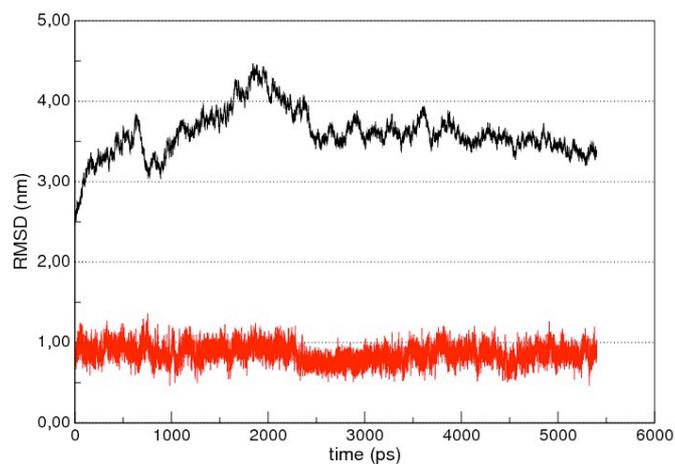
Figure 58: RMSD plot representing human SIRT2 (black) and bound compound **8** (red).
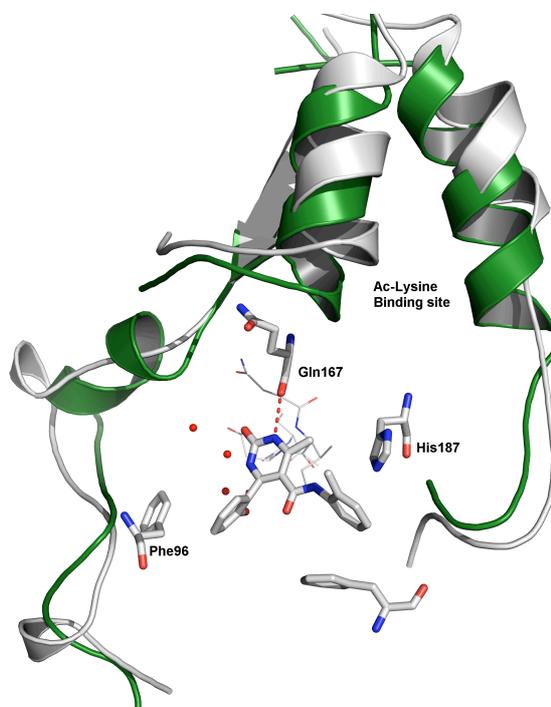
Figure 59: Superposition of the human SIRT2 in complex with compound **10** (IC$_{50}$=130.7±47.2µM) at the beginning (green) and (white) at 5ns of MD simulations. Hydrogen bond is shown as dashed line, and water molecules in the binding pocket as red balls.
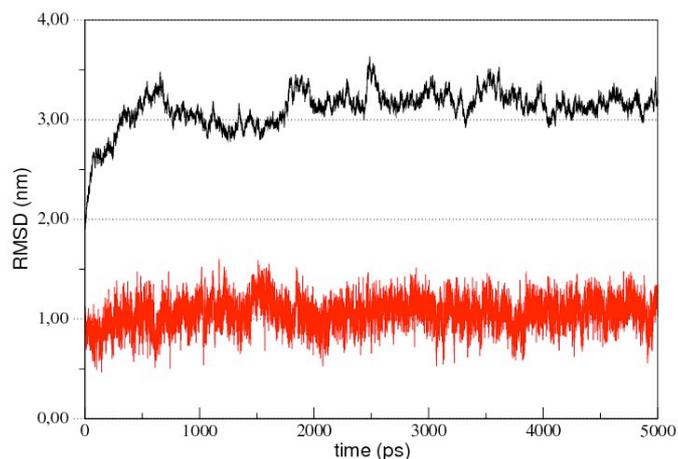
Figure 60: RMSD plot representing human SIRT2 (black) and bound compound **10** (red).

5.4 MM-PBSA Approach

The stability of the complexes during MD simulations suggests that it is reasonable to use these data for a more detailed analysis. The virtual screening resulted in five barbiturates and thiobarbiturates including the active inhibitors **8** and **9**. As we did not observe any correlation between docking scores and IC_{50} values, we calculated the binding free energy by using the MM-PBSA approach. To increase the number of compounds used to establish a quantitative model we added the developed β-arylsplitomicin inhibitors reported in (Table 12). The SIRT2-inhibitor complexes derived from the docking study were used as starting complexes for molecular MD simulations using the AMBER program. All binding free energy presented in this study was based on the last nanosecond of MD simulations of corresponding molecular systems (100). To increase the number of compounds used to establish a quantitative model to five thiobarbiturate inhibitors 15 splitomicin derivatives were added. In chapter 4 we showed that only the *R* isomer is the active enantiomer. Therefore only the *R* isomers of the splitomicin derivatives were used for docking and binding free energy calculations, because the splitomicin derivatives are structurally very similar, it can be suggested that for all compounds, the *R*-isomer represents the active component for biological activity. From (Table 12 and 13) it can be seen that the calculated binding free energies of the β-arylsplitomicin inhibitors are higher in comparison to the thiobarbiturates. On the other hand electrostatic contributions are more favourable for thiobarbiturates (Table 12). The binding free energy for the thiobarbiturate inhibitors is -4.24 kcal/mol (**8**) and -2.98 kcal/mol (**9**). The van der Waals contributions are highly favourable for all compounds.

70

The entropic contribution to binding (TΔS) was estimated by a normal mode analysis of 100 snapshots taken along the last ns MD. The TΔS values are dominated by the translational and rotational contributions whereas their variation is caused by the vibrational contribution. As can be seen in Table 12, 13 all TΔS values are high disfavorable, which means that the entropic effects on binding have high impact on the computation absolute binding free energy (Figure 63).

Table 12: Energy contributions to the free energy of binding of the splitomicin derivatives obtained by the MM-PBSA approach. ΔE_{el} and ΔE_{vdw} are respectively the electrostatic and van der Waals energies of binding; ΔE_{GBSA}: are contributions to the solvation free energy; ΔH_{tot} is the enthalpy of binding, $T\Delta S_{tot}$ is the entropy of binding and ΔG_{calc} is the calculated binding free energy. ΔG_{exp} values were calculated by $\Delta G_{exp}=-RT\ln(IC_{50})$.

comp	ΔE_{el}	ΔE_{vdw}	ΔE_{GBSA}	ΔH_{tot}	$T\Delta S_{tot}$	ΔG_{calc}	IC_{50} [μM]	ΔG_{exp}
2	-2.09	-38.68	7.23	-33.54	-25.79	-7.64	1.5±0.3	-7.94
6	-2.87	-34.10	12.24	-24.73	-17.08	-7.65	6.4±0.3	-7.08
12	-7.81	-30.87	11.26	-27.42	-21.50	-5.92	10.6±1.0	-6.78
13	-2.31	-32.00	8.13	-26.18	-17.72	-8.46	1.2±0.4	-8.07
14	1.27	-32.67	6.01	-25.38	-20.86	-4.52	4.8±2.3	-7.25
15	-8.27	-39.05	16.29	-31.03	-18.00	-13.30	2.8±1.8	-7.57
16	-3.50	-32.56	15.8	-20.26	-15.60	-4.66	5.4±0.2	-7.18
17	-5.00	-28.6	11.49	-22.12	-18.72	-3.40	19.5±9.7	-6.42
18	-0.14	-42.21	17.45	-24.90	-21.22	-3.68	19.7±5.5	-6.41
19	-2.00	-35.81	13.76	-24.06	-14.01	-10.05	2.3±0.3	-7.69
20	-3.81	-37.77	18.41	-23.18	-17.03	-6.15	3.4±0.3	-7.45
21	-3.80	-35.25	12.53	-26.52	-17.47	-9.05	4.4±0.6	-7.30
22	-4.65	-34.28	14.23	-24.70	-11.90	-12.80	3.1±0.5	-7.51
23	-11.10	-34.57	22.80	-22.88	-20.26	-2.62	20.0±8.0	-6.41
24	2.24	-31.94	4.19	-25.51	-15.55	-9.96	5.2±1.0	-7.20

Table 13: Energy contributions to the free energy of binding of the thiobarbiturate and barbiturate derivatives obtained by the MM-PBSA approach.

comp	ΔE_{el}	ΔE_{vdw}	ΔE_{GBSA}	ΔH_{tot}	$T\Delta S_{tot}$	ΔG_{calc}	IC_{50}[μM]	ΔG_{exp}
7	-5.59	-28.71	28.71	-12.97	-8.66	-4.31	61±3.5	-5.75
8	-7.38	-32.20	19.61	-19.96	-16.98	-2.98	11.3±1.7	-6.74
9	-19.10	-31.79	30.35	-20.54	-16.30	-4.24	9.1±5.8	-6.87

10	-7.89	-31.20	24.30	-14.79	-15.56	0.77	130.7	-5.29
11	-13.90	-28.23	25.31	-16.82	-14.54	-2.28	40.7±3.9	-5.98

To determine whether MM-PBSA is useful for the further lead optimization, the correlation between calculated values (binding free energies ΔG_{calc} and binding enthalpies ΔH_{tot}) and the experimental IC_{50} values were analysed. This approach represents only a rough approximation, because the biological data is used instead of pure thermodynamic values from calorimetric studies. Another important element in calculating binding free energy using MM-PBSA approach is the solvation energy. This component is computed from an empirical equation $\Delta G_{SA} = \beta + SASA + \gamma$, the default values in the AMBER package are set to 0.00542 kcal/(molÅ^2) and 0.92 kcal/mol respectively. These parameters were obtained from a regression analysis of the solvation energies of 67-alkane molecules by Honig *et al.* [182]. It is the question if these default values are always appropriate to study diverse set of compounds. Therefore an ideal correlation can not be expected. As shown in Figure 63, where the experimental values are plotted versus the calculated binding energies, there is a significant correlation between the binding free energy ΔG (r=0.83, r^2=0.69, SD=0.40) and the biological activity. For the enthalpy ΔH_{tot} the correlation is lower (r=0.69, r^2=0.47, SD=0.52) due to one outlier: compound 12 (Figure 61). Removing the outlier resulted in a model with a regression coefficient of r^2=0.65 for the enthalpy model (Figure 62). To test the predictive ability of the model, we carried out leave-one-out (LOO) cross validation. For the binding free energy ΔG model we obtained a cross-validated q$^2_{LOO}$ value of 0.61 (Figure 63).
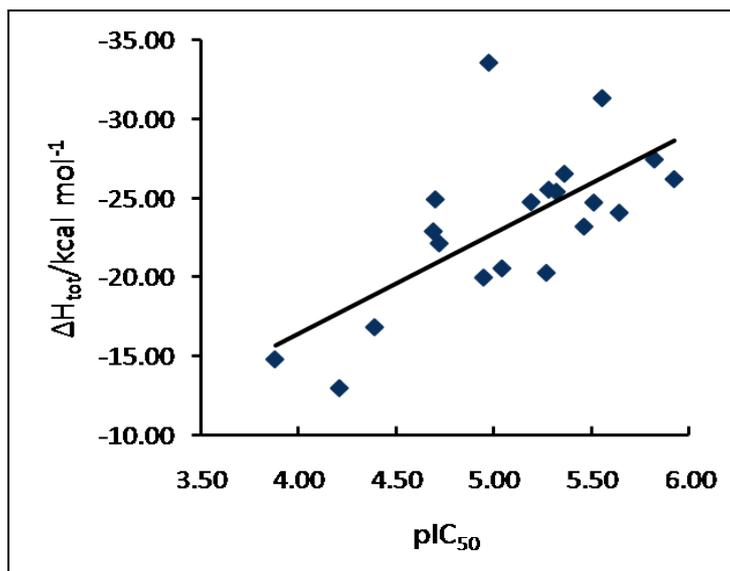
Figure 61: Correlation between calculated MM-PBSA binding enthalpies ΔH_{calc} and the SIRT2 pIC_{50} values.
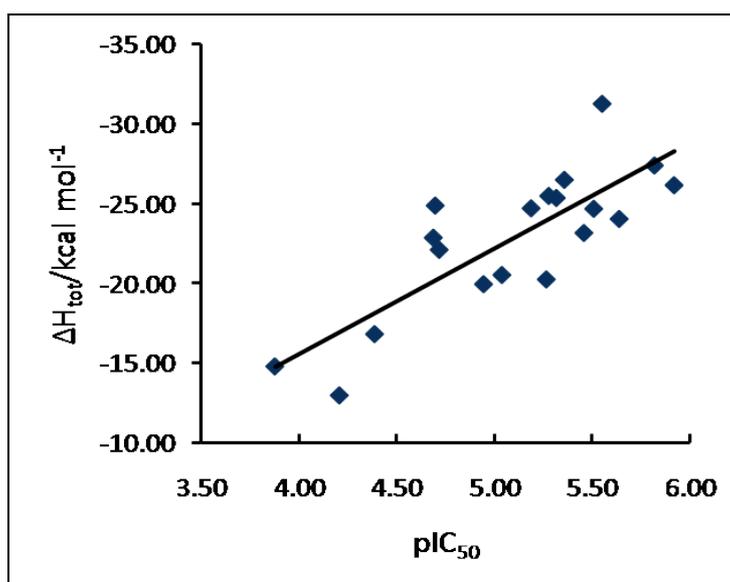
Figure 62: Correlation between calculated MM-PBSA binding enthalpies ΔH_{calc} and the SIRT2 pIC_{50} values, after removing outlier compound 12.
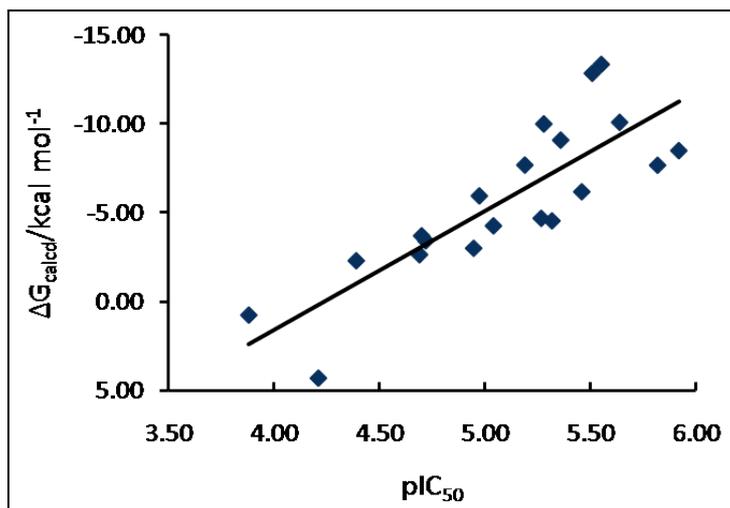
Figure 63: Correlation between calculated MM-PBSA binding free energies ΔG_{calc} and the SIRT2 pIC_{50} values.

In contrast to the applied GOLD docking scores, the MM-PBSA approach takes protein flexibility into account. This is a significant contribution to improved ligand scoring. Another reason for the improved results with the MM-PBSA calculations is that the force field used a continuum solvent electrostatic to calculate $\Delta G_{sol.}$ This provides a more accurate description of the ligand binding than the empirical GOLD scoring function. In contrast to more rigorous methods such as free energy perturbation (FEP) or thermodynamic integration (TI), MM-PBSA is faster by several orders of magnitude. However, the approximations inherent to MM-PBSA result in larger errors than those associated with the more sophisticated methods such as FEP or TI. In particular, estimation of the entropic term on the basis of the trajectories is often connected with a large standard deviation. This can also be seen on our data see (Table 12 and 13), where the entropy contributions are very different for compounds structurally similar. To overcome the entropy problem, it was suggested to increase the simulation time and to use smaller snapshot sizes for sampling the entropic term. However, for larger data sets this dramatically increases the time required for the MD simulations, therefore, finding an acceptable balance between accuracy and simulation time is still a challenge.

5.5 Novel Thiobarbiturates

The analysis of the MD simulations showed that most active thiobarbiturates, compounds **8** and **9**, are stable and make hydrogen bonds with His187 and the backbone NH group of Gln167. The hydrogen bond between His187 and the thiobarbiturate moiety of **8** and **9** was

found to be stable during MD simulation, whereas the direct hydrogen bond to the backbone NH group of Gln167 was observed only at the beginning of the simulation. Additionally analysis of the molecular interaction field derived with the hydrophobic methyl probe showed a favourable interaction field above the napthyl substituent of docked compound **9** **(**Figure 64). Therefore we designed and synthesized five thiobarbiturates (25-29) (Figure 65) with hydrophobic substituents. Docking studies showed that these compounds obtained similar docking pose as for compounds **8** and **9** (Figure 53, 54). As an example, the interaction of the novel thiobabrituates is shown in (Figure 67). The calculated ΔG values of the five compounds were found to be < -4.2 kcal/mol indicating that they should be just, as or more potent than the thiobarbiutate 9 (Table 13). Subsequent biological testing showed that all five new thiobarbiturates are active against SIRT2 at concentrations < 30 μM (Figure 66).
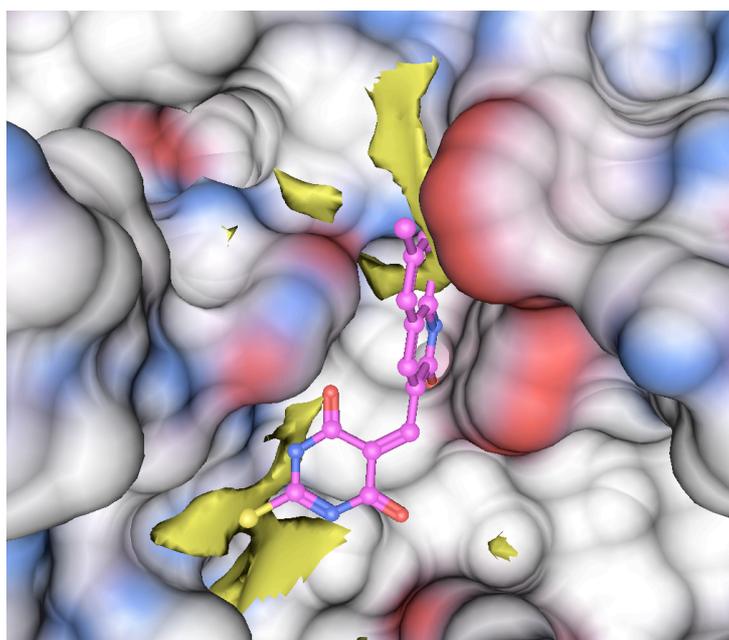
Figure 64: Molecular interaction fields derived with the hydrophobic methyl probe coloured in yellow for compound **9**, obtained in MOE program.
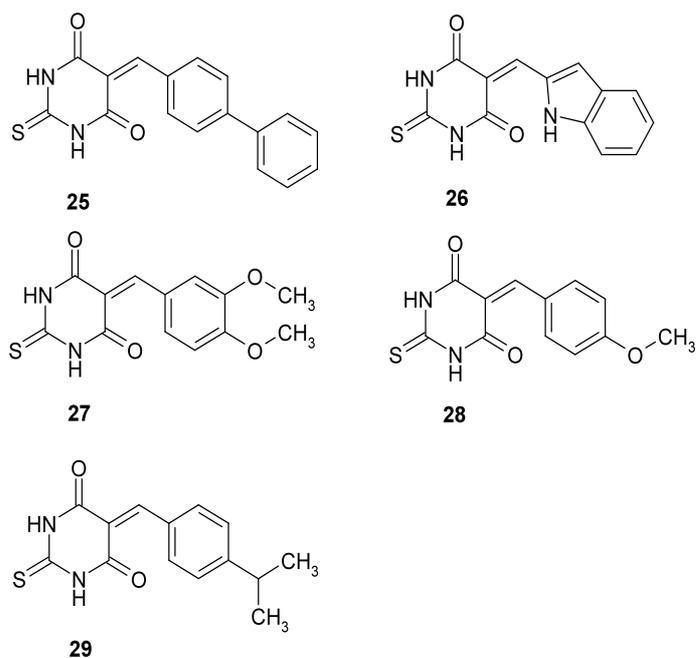
Figure 65: Molecular structures of and five novel thiobarbiturates.

comp	SIRT2 IC$_{50}$±SE [μM]
25	8.7±0.7
26	20.3±1.5
27	30.1±3.1
28	20.0±1.7
29	14.7±2.1
30	NA[a]
31	NA[a]
[a] Inhibition < 10% at 50 μM	

Figure 66: Inhibition of SIRT2 by the novel synthesized thiobarbiturates.
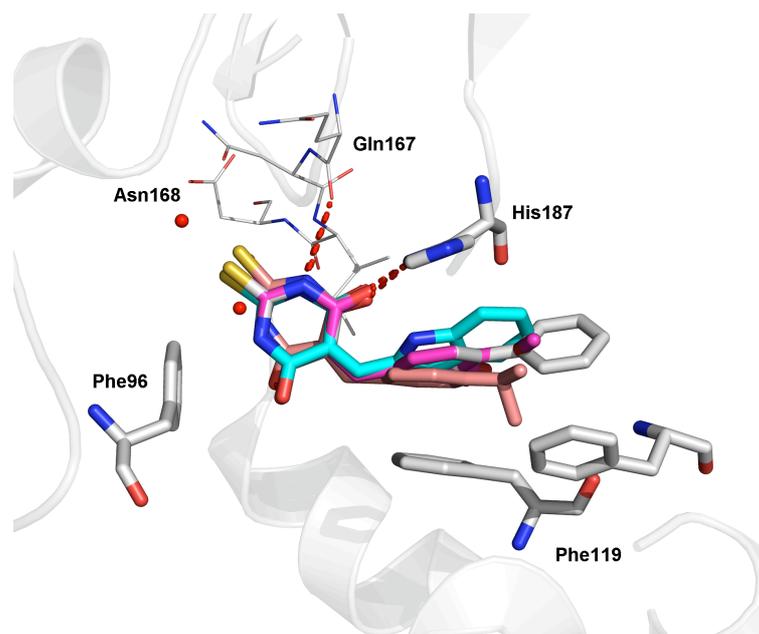
Figure 67: Predicted binding mode of the five novel thiobarbiturates. Water molecules are displayed as red balls. Hydrogen bonds are indicated by dashed lines.

In general, we were able to obtain a good agreement between ΔG_{calc} and pIC_{50} values for the five novel thiobarbiturates (Figure 70, Table 14). Compound **25**, bearing a biphenyl group, is the most active thiobarbiturate toward SIRT2 in agreement with the predicted MM-PBSA calculations. The biphenyl fits well in the acetyl lysine substrate channel and interacts with the surrounding aromatic side chains (Figure 68). To further support our hypothesis that the hydrophobic aryl group is important for sirtuin activity, we experimentally tested unsubstituated barbituric and thiobarbituric acid.

MD simulations were carried out for human SIRT2 in complex with compound **25.** The calculated MD structures remain similar to those obtained for compound **8**, **9** and cambinol with RMSD values for the ligand within 1-1.3 Å and for the protein within the 3.5 Å range (Figure 69). As it is presented in (Figure 68), the acetyl lysine binding tunnel and flexible loop shifted away from the starting position while the compound **25** remained bound. The biphenyl group of **25** slightly moved inside the acetyl-lysine binding tunnels whereas the thiobarbiturate ring stayed stable in the nicotinamide binding pocked making a hydrogen bond with Gln167 (Figure 68). Interesting is also displacement of the His187 residue during MD simulations.
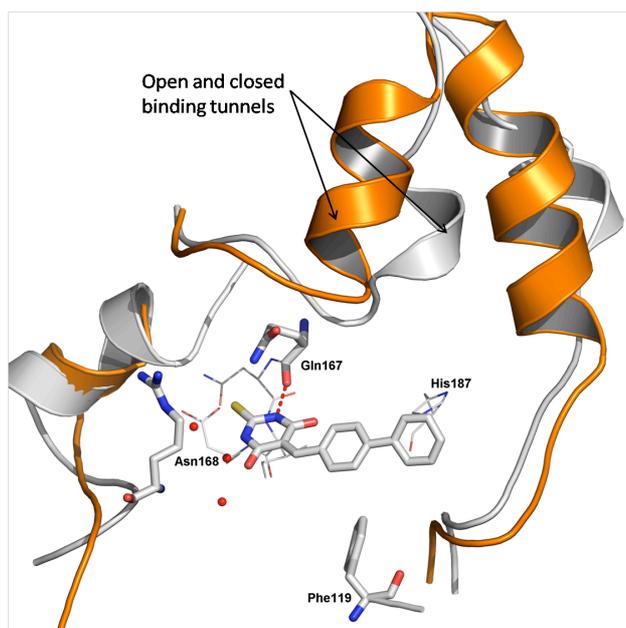
Figure 68: Superposition of the human SIRT2 in complex with compound **25** (IC$_{50}$=8.7±0.7μM) at the beginning (orange) and (white) at 5ns of MD simulations. Hydrogen bond is shown as dashed line, and water molecules in the binding pocket as red balls.
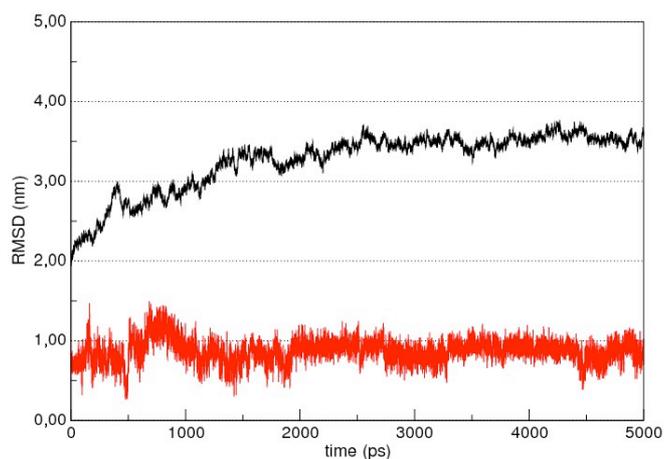
Figure 69: RMSD plot representing human SIRT2 (black) and bound compound **25** (red).

comp	ΔE_{el}	ΔE_{vdw}	ΔE_{GBSA}	ΔH_{tot}	$T\Delta S_{tot}$	ΔG_{calc}	IC$_{50}$[μM]	ΔG_{exp}
25	-5.16	-31.44	15.47	-21.13	-15.01	-6.29	8.7±0.7	-6.90
26	-8.53	-21.73	14.21	-16.05	-11.85	-4.20	20.3±1.5	-6.40
27	-5.76	-24.04	14.48	-15.32	-11.07	-4.31	30.1±3.1	-6.16
28	-7.54	-31.24	20.68	-18.10	-13.56	-4.54	20.0±1.7	-6.41
29	-3.14	-34.98	13.86	-24.26	-19.35	-4.91	14.7±2.1	-6.59

Table 14: Energy contributions to the free energy of binding of the thiobarbiturate and barbiturate derivatives obtained by the MM-PBSA approach.
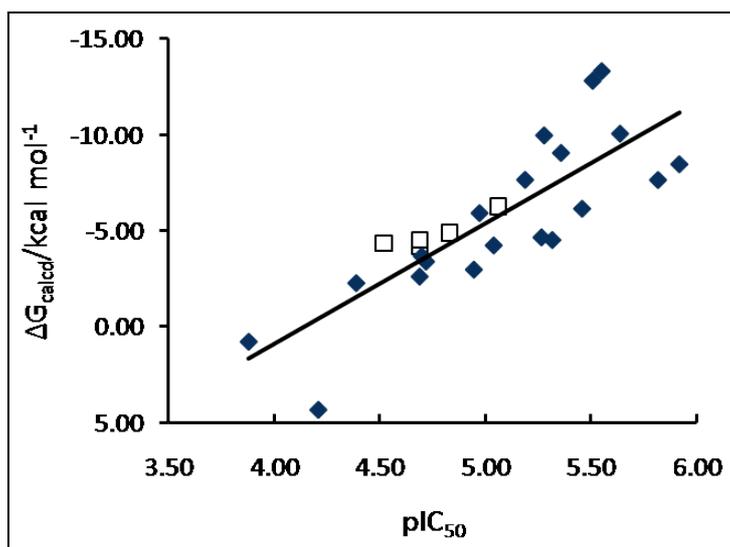
Figure 70: Correlation between calculated MM-PBSA binding free energies ΔG_{calc} and the SIRT2 pIC_{50} values of training set (blue) and test set compounds (white).

5.6 Conclusion

We showed that combination of different computational methods with experimental *in vitro* testing can be used for the discovery of new sirtuin inhibitors. Polar interactions that anchor the identified thiobarbiturates at the SIRT2 binding pocket were found. The hydrophobic groups of the inhibitors were found to interact with the acetyl-lysine substrate pocket. In contrast, barbituric and thiobarbituric acid, which do not possess a hydrophobic group, were found to be inactive. MD simulations showed that the two residues His187 and Gln167 play a major role in the stabilization of the binding mode of splitomicins and thiobarbiturates at the SIRT2 nicotinamide-binding pocket. The MD simulations of SIRT2 bound to inhibitors (as well as NAD^+) showed a general movement of the flexible loop as well as residues of the acetyl-lysine binding tunnel which was not observed in the simulations of the uncomplexed sirtuins. This observation can be useful for the further development of sirtuin inhibitors.

Finally, we applied the MM-PBSA method to calculate the relative binding free energies for a set of 20 SIRT2 inhibitors. These calculations were found to be useful in order to get more detailed information about the binding affinity that cannot be provided by docking programs and scoring functions. Further optimization of the identified thiobarbiturate-based sirtuin inhibitors can thus be performed in a more rational fashion.

Chapter 6

Virtual Screening and Binding Free Energy Calculations of Novel Thiobarbiturates as Sirtuin Inhibitors

6.1 Generation of a Focused Model for Thiobarbiturates

A multi-step virtual screening was carried out in order to identify more potent thiobarbiturates. Compounds were docked into the human SIRT2 structure and virtual screening hits were analyzed through the application of linear interaction free energy (LIE) and molecular mechanics Poisson-Boltzmann surface area (MM-PBSA).

6.1.1 MM-PBSA Models

The ten active thiobarbiturate inhibitors described in chapter 5 (Figure 52, 65) were used as training set for generating MM-PBSA models. Based on calculated enthalpy and binding free energy, ΔH and ΔG models were established. The quality of these models was evaluated by means of the correlation coefficient (r^2), and the root mean square of error (RMSE). In case of the enthalpy model ΔH (n=10), the statistical values yield an r^2=0.60 and RMSE value 0.30 kcal/mol (Figure 71). Compound 29 was found to be an outlier because the difference between calculated and experimental values was shown to be high in comparison to other compounds. Excluding it resulted in a significantly better correlation. The statistical values derived from the new ΔH training set (n=9) were r^2=0.76 and RMSE of 0.18 kcal/mol (Figure 72, Table 15). The ΔG model was built in the same way as described above for the ΔH model. The obtained correlation between experimental and calculated data yielded the following values: r^2=0.54 and RMSE 0.24 kcal/mol (Figure 73). Obtained statistical values for these two models inlcuding the leave one out q^2 values showed that the model based on the calculated enthalpy of binding showed a better internal predictivity than ΔG model.

Table 15: Summary of statistical values obtained for the MM-PBSA models based ond ΔH and ΔG.

Model	Training set		
	r^2	RMSE	q^2_{LOO}
ΔH[a]	0.76	0.18	0.70
ΔG[b]	0.54	0.24	0.40

[a] model obtained for n=9, [b] model obtained for n=10.

Binding free energy calculations require an entropy term, which in MM-PBSA method is estimated using nmode analysis. The entropy term was also included in the ΔG model. This term is sometimes difficult to correctly estimate because of the slow convergence and sampling difficulties. It was shown in literature that for many targets entropy changes could be omitted if all ligands are roughly the same size [183,184]. On the other hand, a reasonable amount of experimental and computational data suggest that if we want to have a more clear picture on the system energy, this term can not be ignored [185]. Both ΔH (n=9) and ΔG (n=10) models were used for the further analysis.
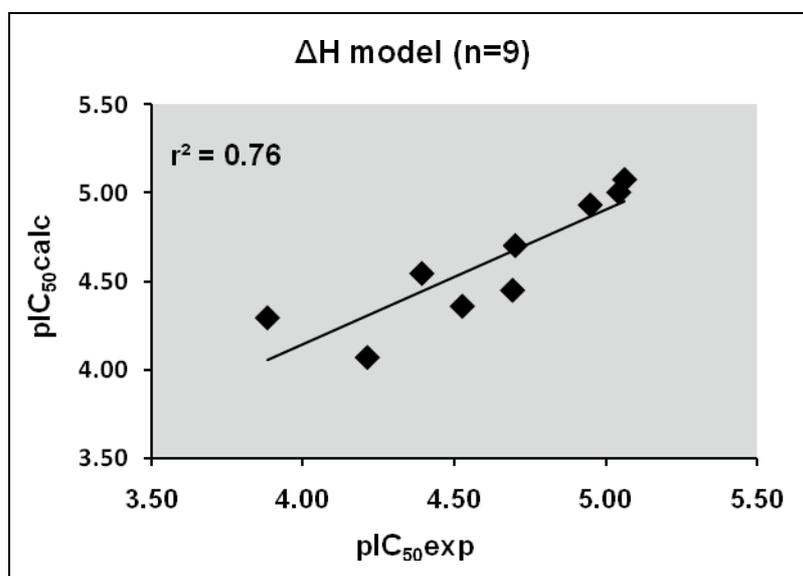
Figure 71: Correlation between experimental pIC$_{50}$exp values and calculated pIC$_{50}$calc values derived from the ΔH model.
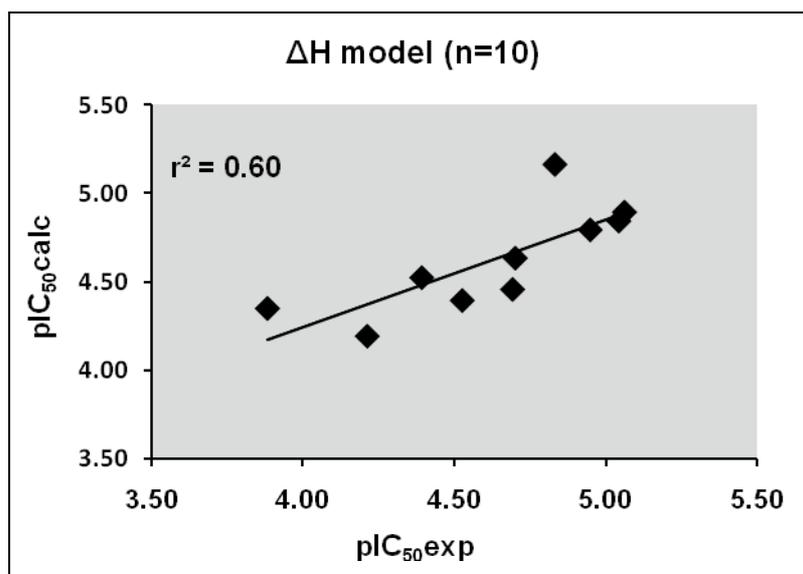
Figure 72: Correlation between experimental pIC$_{50}$exp values and calculated pIC$_{50}$calc values derived from the ΔH model.
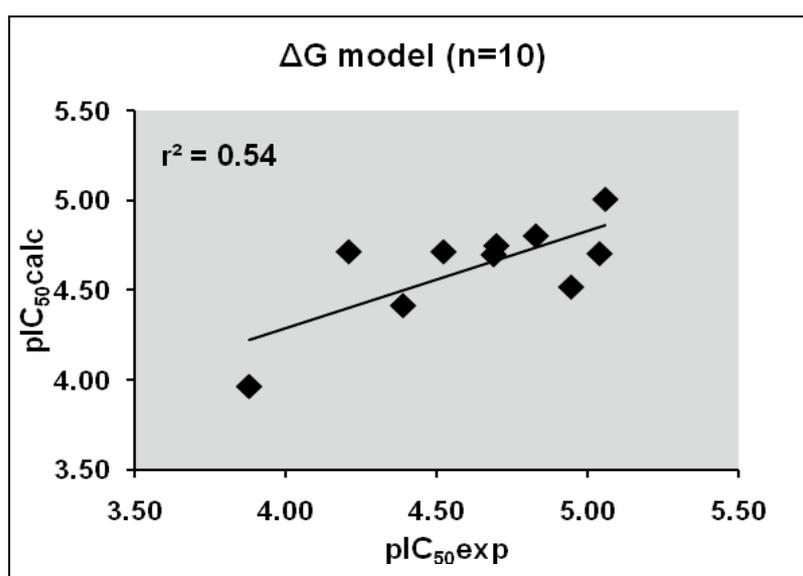
Figure 73: Correlation between experimental pIC$_{50}$exp values and calculated pIC$_{50}$calc values derived from the ΔG model.

6.1.2 Linear Interaction Energy (LIE) Models

The LIE energy method applies experimental data on binding free energy values for a set of ligands (training set) to estimate the binding affinities for novel test set compounds. The method is based on the linear response approximation (LRA), which formulates that binding free energy of a protein-ligand system is a function of polar and nonpolar energy components

that scale linearly with the electrostatic and van der Waals interactions between. In the original formulation of the method the binding free energy is evaluated from:

$$\Delta G^{LIE}_{bind} = \alpha\Delta <E^{vdw}_{l\text{-}s}> + \beta\Delta<E^{ele}_{l\text{-}s}> + \gamma \tag{8}$$

where Δ is a difference between the energies of the bound and free state, and E represents MD or MC averages of intermolecular electrostatic $<E^{ele}_{l\text{-}s}>$ and van der Waals $<E^{vdw}_{l\text{-}s}>$ energies for the ligand with its surroundings. The α, β and γ are LIE fitting parameters, which need to be determined by correlating the calculated with the experimental data of the training set compounds. The fitting parameters α and β were firstly set to fixed values (α=0.161 and β=0.50), and they can be transferred among different protein systems. Since studies, which investigated influence of different α and β parameters, it was found that they depend on the studied system, applied force field and computational methods employed [185, 186].

Standard MD simulations were carried out for one nanosecond to compute the interaction terms required in the LIE method using the Sander module of Amber 9 [150]. Two separate MD simulations were carried out: one for the solvated protein-ligand complex and one for the ligand in solvent only. Obtained snapshots were then split into its environment and the ligand, for that a *perl* script was written which ran *ptraj* [150] multiple times. This allowed generating pdb files of a) the complex environment, b) ligand from the complex, c) solvent environment and d) the ligand from the solvent. Finally, single step minimization was run, for each generated pdb of each sub-section to obtain the van der Waals (vdw) and electrostatic (ele) contribution of each-subsection. The interaction energies between ligand and different surroundings are equal to the difference between the energy of the total system and sum of the individual components. Thus, the interaction energies (E_{IN}) can be described as follows:

$$E_{IN} = E_{vdw} + E_{ele} \tag{9}$$

$$E_{IN\text{-}bound} = E_{IN\text{-}total} - E_{IN\text{-}receptor} - E_{IN\text{-}solvent} - E_{IN\text{-}ligand} \tag{10}$$

$$E_{IN\text{-}free} = E_{IN\text{-}total} - E_{IN\text{-}solvent} - E_{IN\text{-}ligand} \tag{11}$$

The obtained energy terms were applied to the LIE standard formula for 10 training set compounds (Figure 52, 65). The empirical parameters α, β and constant γ were determined using the least-square error fitting method (MOE program) and solved in a fashion similar to that of QSAR models. Two models were prepared: model A, where α, β and γ parameters were evaluated, and model B, where only α and β were evaluated and γ was set to zero. The quality of the training set fit was evaluated by the value of the squared correlation coefficient (r^2) and leave-one-out cross validation coefficient (q^2_{LOO}) which was 0.74 and 0.65 for model A and 0.58 and 0.57 for model B. The values obtained for the three fitting parameters α, β, and γ for model A and B are presented in Table 16, 17. The estimated binding free energy values for the training-set compounds were also plotted against the experimental data pIC_{50} (Figure 74 and 75).

Table 16: Statistical values of the LIE models. α, β and γ correspond to the coefficients of the LIE model; RMSE is the root means square error in kcal/mol, r^2 is the correlation coefficient, and q^2_{LOO} the leave-one-out cross-validated correlation coefficient.

Model	Parameters			Training set (n=10)		
	α	β	γ	r^2	RMSE	q^2_{LOO}
A	0.14	-0.12	-3.98	0.74	0.18	0.65
B	0.36	-0.17	0	0.58	0.31	0.57

Table 17: Overview of the electrostatics (ΔE_{ele}) and van der Waals (ΔE_{vdw}) energies (kcal/mol) obtained for a training set $n=10$, ($\Delta G^{LIE}A$) values predicted with a fitting parameter γ≠0, and ($\Delta G^{LIE}B$) with fitting parameter γ=0, (ΔG_{exp}) experimental values.

comp.	Ligand-surrounding interactions (kcal/mol)				Predictions			
	$<E^{vdw}>_{bound}$	$<E^{vdw}>_{free}$	$<E^{ele}>_{bound}$	$<E^{ele}>_{free}$	$\Delta G^{LIE}A$	$\Delta G^{LIE}B$	IC_{50}	ΔG_{exp}
7	-38.18	-18.70	-42.47	-36.73	-6.02	-6.03	61.00	-5.74
8	-43.98	-21.33	-32.62	-29.25	-6.73	-7.58	11.30	-6.74
9	-37.53	-17.54	-27.52	-25.35	-6.50	-6.83	9.10	-6.87
10	-39.78	-20.92	-38.92	-31.27	-5.71	-5.47	130.7	-5.29
11	-35.98	-20.19	-29.85	-26.03	-5.73	-5.03	40.70	-5.98
25	-38.91	-22.49	-23.74	-28.88	-6.84	-6.82	8.70	-6.89
26	-35.03	-18.20	-23.53	-25.21	-6.50	-6.36	20.30	-6.39
27	-36.34	-16.70	-34.04	-26.76	-5.86	-5.82	30.10	-6.16
28	-32.21	-17.21	-26.14	-28.36	-6.31	-5.80	20.00	-6.40
29	-35.95	-18.89	-25.20	-29.50	-6.83	-6.90	14.70	-6.58
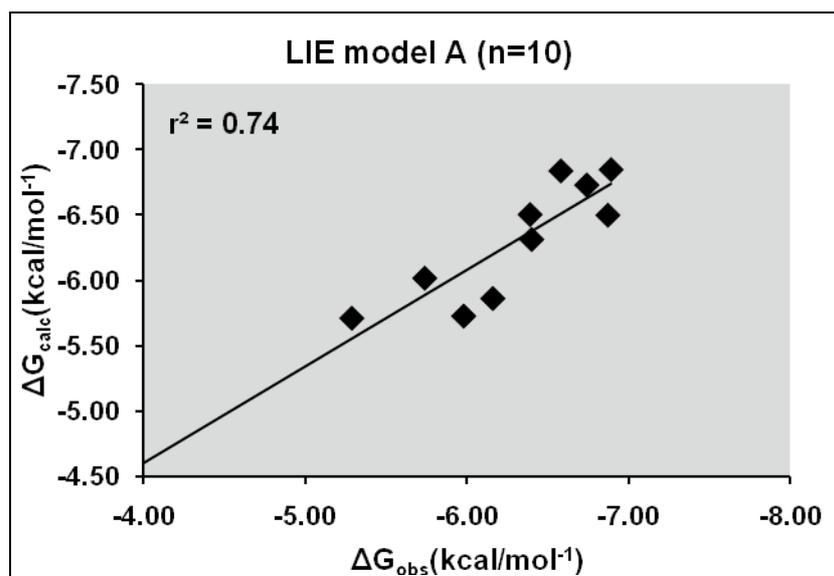
Figure74: Correlation between observed ΔG_{obs} and calculated ΔG_{calc} values obtained for training set compounds derived from LIE model A.
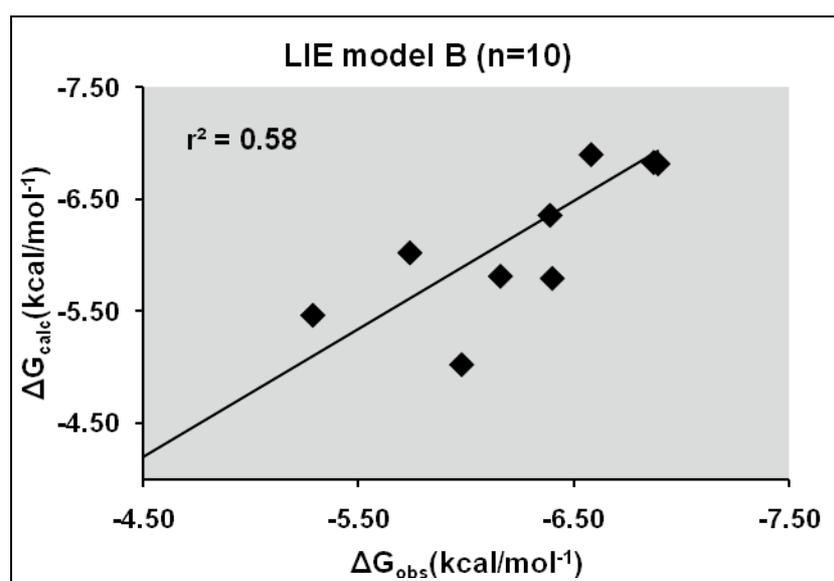
Figure 75: Correlation between observed ΔG_{obs} and calculated ΔG_{calc} values obtained for training set compounds derived from LIE model B.

6.2 Identifying and Predicting Novel Thiobarbiturates

After preparing training set models, a multi-step Virtual Screening (VS) was performed using the Chembridge database to identify novel more potent thiobarbiturates. These comopounds should represent an ideal independent test set. The MACCS key fingerprints were used to search the database for compounds similar to the most active thioabarbiturates (compounds 9 and 25, Figure 52, 65). Applying a Tanimoto coefficient of 0.75 we identified 100 compounds

which were subsequently docked in the SIRT2 binding pocket using the GOLD program. 14 thiobarbiturate derivatives were selected and their biological data were predicted using the MM-PBSA and LIE models (Figure 76). In addition, 9 derivatives were synthesized in the group of Prof. Jung at the University of Freiburg based on our docking studies (Figure 77). The novel compounds were subsequently calculated and added to test set group.
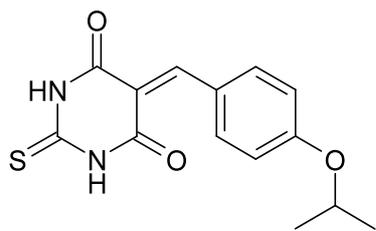
6486096
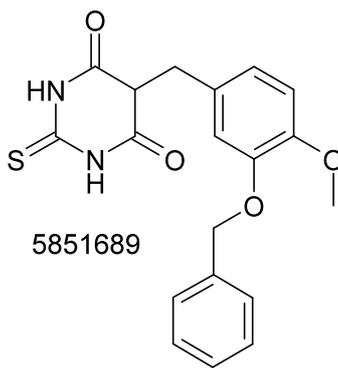
5851689
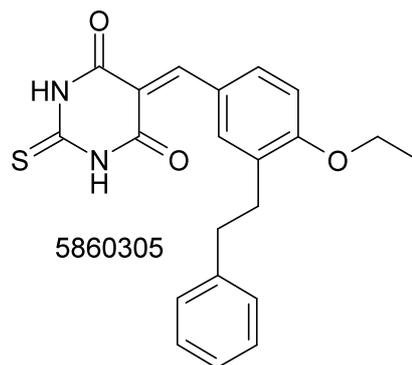
5860305
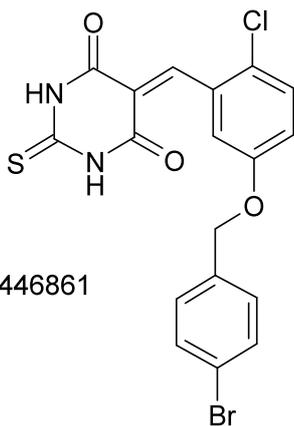
6446861
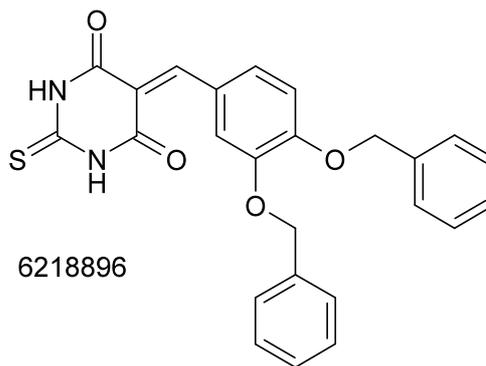
6218896
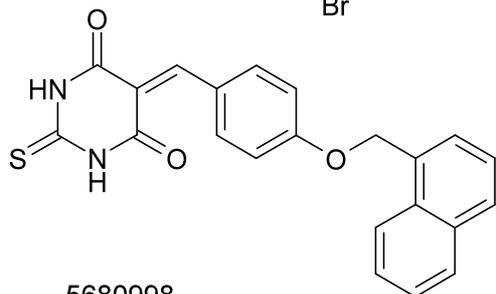
5680998
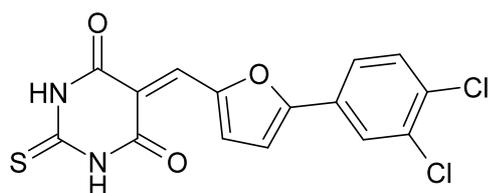
5545264
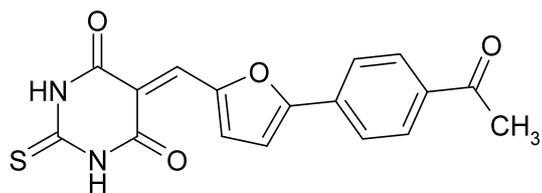
6568425

7093707

5483251

87
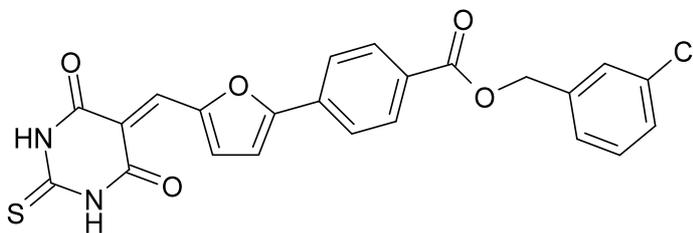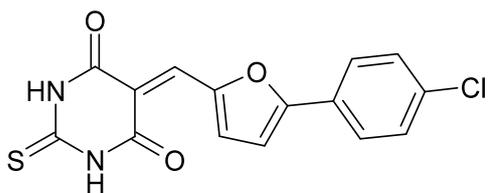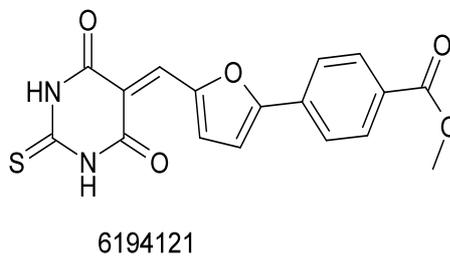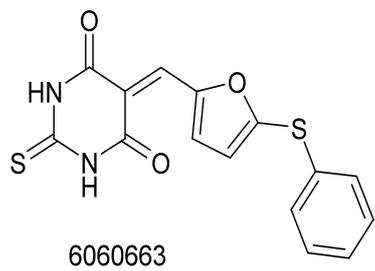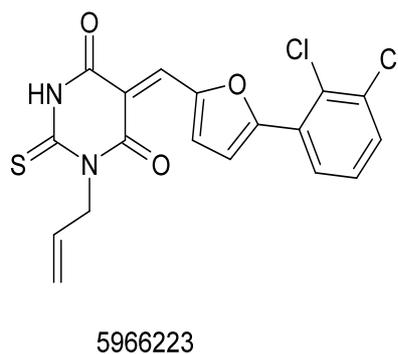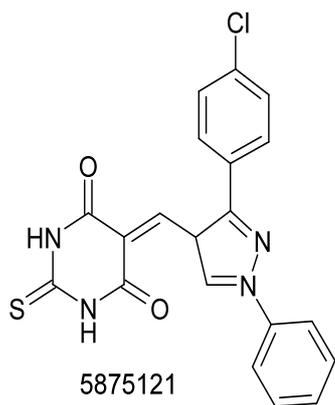
Figure 76: Thiobarbiturate compounds identified by virtual screening from Chembridge database.
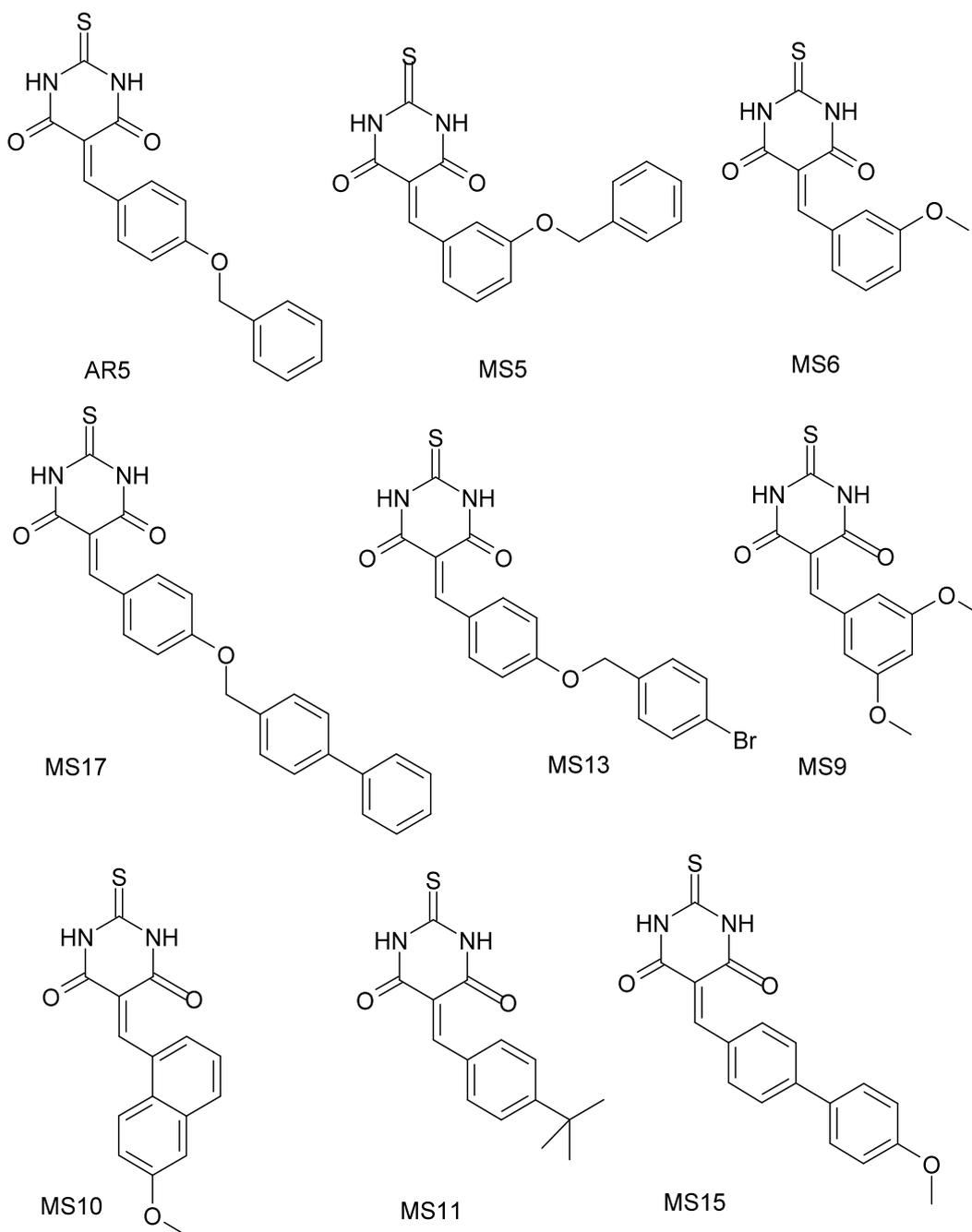
Figure 77: Thiobarbiturate compounds synthesized in the group of Prof. M.Jung, University of Freiburg.

6.2.1 Results Obtained by MM-PBSA approach

The ΔH and ΔG models were then applied for predicting the binding affinities of the selected independent test-set compounds (n=23, Figure 78, 79 Table 18). The ΔH model was found to better predict binding affinities, as the correlation between predicted and experimental values increases to r^2_{pred} = 0.44 (Figure 78). In case of the ΔG model, the correlation coefficient was

$r^2 = 0.035$, which suggests a significantly weaker predictive ability of this model (Figure 79). The enthalpy (ΔH) model was able to predict the exact experimental binding affinities, e.g 7093707, 5860305 and 5966223 (Table 19). In the case of the binding free energy model (ΔG), the values calculated for some of the compounds were significantly underestimated.
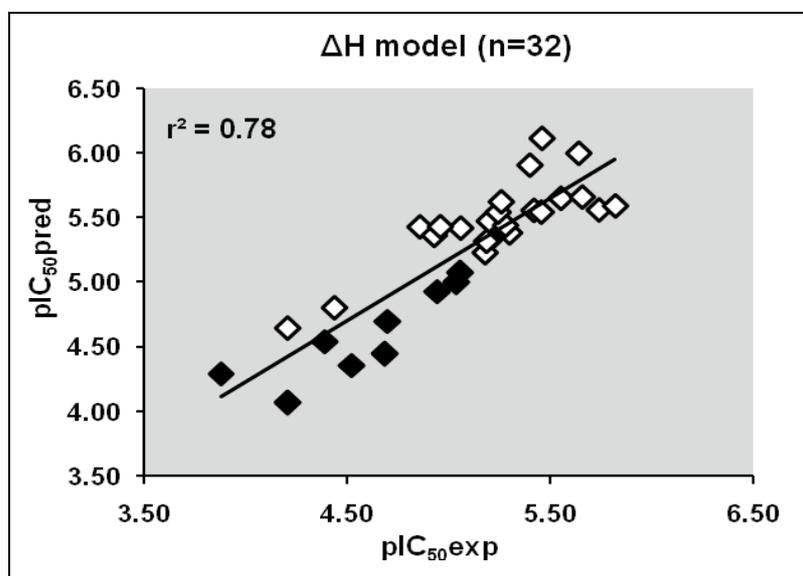
Figure 78: Correlation between experimental pIC$_{50}$exp and predicted pIC$_{50}$pred values for n=32 compounds derived from the ΔH model. Black points represent the training set compounds and the white test set compounds.
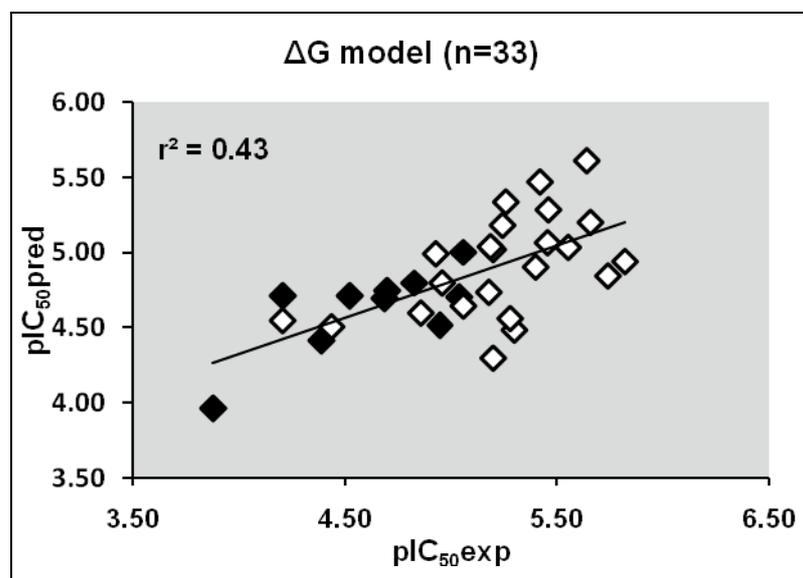
Figure 79: Correlation between experimental pIC$_{50}$exp and predicted pIC$_{50}$pred values for n=33 compounds derived from the ΔG model. Black points represent the training set compounds and white the test set compounds.

Table 18: Energy contributions to the free energy of binding of the thiobarbiturate compounds (test set) obtained by the MM-PBSAapproach. ΔE_{el} and ΔE_{vdw} are the electrostatic and van der Waals energies of binding, respectively, ΔE_{GBSA} are contributions to the solvation free energy, ΔH_{tot} is the enthalpy of binding, $T\Delta S_{tot}$ is the entropy of binding, and ΔG_{calc} is the calculated binding free energy. ΔG_{exp} values were calculated by $\Delta G_{exp}=-RTln(pIC_{50})$. For compounds MS6 and MS9 purity less than 100%.

comp	ΔE_{el}	ΔE_{vdw}	ΔE_{sol}	ΔH_{tot}	$T\Delta S_{tot}$	ΔG_{calc}	$IC_{50}[\mu M]$	ΔG_{exp}
6486096	-18.54	-34.70	30.06	-23.17	-16.78	-6.39	5.80	-7.11
5851689	-11.63	-37.42	24.66	-24.39	-22.91	-1.48	5.80	-7.11
5860305	-6.53	-37.38	20.27	-23.64	-20.89	-2.75	4.90	-7.21
6446861	-16.21	-33.30	24.42	-25.09	-19.89	-5.20	1.80	-7.80
6218896	-17.41	-42.30	32.26	-27.91	-22.31	-5.60	3.90	-7.34
5680998	-16.03	-43.68	31.05	-28.66	-18.25	-10.41	2.30	-7.65
5545264	-4.25	-32.16	11.07	-25.34	-19.49	-5.85	1.50	-7.91
5875121	-15.31	-41.75	30.00	-25.06	-15.61	-9.45	3.80	-7.36
5966223	-14.26	-40.19	28.63	-25.82	-19.33	-6.49	2.80	-7.54
6060663	-14.62	-38.58	28.26	-24.95	-18.25	-6.70	3.50	-7.41
6194121	-13.92	-43.33	32.31	-24.91	-17.42	-7.49	5.70	-7.12
6568425	-19.19	-39.51	33.10	-25.60	-17.06	-8.54	5.50	-7.15
7093707	-6.81	-43.13	24.03	-25.90	-18.28	-7.62	2.20	-7.69
5483251	-16.06	-34.72	27.67	-23.11	-16.59	-6.52	6.50	-7.05
AR5	-11.12	-34.23	21.41	-23.94	-20.10	-3.84	8.60	-6.85
MS5	-12.43	-36.43	24.84	-24.02	-20.50	-3.52	13.50	-6.59
MS17	-1.00	-49.58	26.47	-24.11	-20.84	-3.27	5.20	-7.15
MS13	-15.98	-36.84	23.23	-29.60	-21.41	-8.19	3.40	-7.40
MS6	-7.08	-25.82	13.97	-18.92	-16.02	-2.90	35.60	-6.02
MS9	-22.34	-36.91	41.61	-17.64	-14.46	-3.18	61.60	-5.70
MS10	-14.57	-37.84	28.93	-23.48	-17.28	-6.20	11.70	-6.67
MS11	-14.14	-35.75	25.86	-24.03	-19.15	-4.88	10.90	-6.71
MS15	1.98	-39.91	15.53	-22.39	-17.93	-4.46	6.60	-7.01

Table 19: Predicted biological data for test set compounds, $pIC_{50}\Delta H$-values predicted using ΔH model, $pIC_{50}\Delta G$-values predicted using ΔG model, pIC_{50}-experimental data, error-difference between experimental and calculated value.

comp	$pIC_{50}\Delta H$	error	$pIC_{50}\Delta G$	error	pIC_{50}
6486096	5.33	0.10	5.02	0.21	5.23
5851689	5.48	0.25	4.29	0.94	5.23
5860305	5.38	0.08	4.48	0.82	5.30
6446861	5.56	0.18	4.84	0.90	5.74
6218896	5.91	0.51	4.90	0.50	5.40
5680998	6.00	0.36	5.60	0.40	5.64
5545264	5.59	0.23	4.93	0.89	5.82
5875121	5.55	0.13	5.46	0.04	5.42
5966223	5.65	0.1	5.03	0.52	5.55
6060663	5.54	0.08	5.06	0.40	5.46
6194121	5.54	0.30	5.18	0.06	5.24
6568425	5.62	0.36	5.33	0.07	5.26
7093707	5.66	0.00	5.20	0.46	5.66
5483251	5.31	0.12	5.03	0.16	5.19
AR5	5.42	0.36	4.64	0.42	5.06

MS5	5.43	0.57	4.59	0.28	4.87
MS17	5.44	0.16	4.56	0.72	5.28
MS13	6.12	0.66	5.28	0.18	5.46
MS6	4.80	0.36	4.50	0.06	4.44
MS9	4.65	0.44	4.54	0.33	4.21
MS10	5.36	0.43	4.99	0.06	4.93
MS11	5.43	0.47	4.79	0.17	4.96
MS15	5.23	0.05	4.73	0.45	5.18

6.2.2 Results Obtained by LIE approach

The α, β and γ parameters of models A and B were optimized using LIE, and the two models were subsequently used to predict binding affinities (Table 20). The electrostatic and van der Waals energies were obtained from MD simulations, whereas the same protocol was used for training set compounds. The calculated ΔG values were plotted against the experimental pIC$_{50}$ values, the correlation coefficient was low (r^2_{pred}=0.23) for model A, and model B had a higher correlation coefficient (r^2_{pred}=0.49) (Figure 81). In contrast to the significant correlation observed for the training set compounds, model A did not perform well in the prediction of test set binding affinities (correlation coefficient dropped from 0.74 to 0.62), (Figure 80).

As shown in Table 20, the predicted ΔG^{LIE} values for the test set compounds are in acceptable agreement with the experimental data. Both models poorly estimated the biological data for compound MS15, where the difference between experimental and obtained binding free energy is ~1.76 kcal/mol. This compound was considered an outlier, and was excluded from correlation plots.

Table 20: Overview of the electrostatics (ΔE_{ele}) and van der Waals (ΔE_{vdw}) energies (kcal/mol) obtained for a test set n=23, (ΔG^{LIE}A) values predicted with a fitting parameter $\gamma \neq 0$, and (ΔG^{LIE}B) with fitting parameter γ=0, (ΔG_{exp}) experimental values. For compounds MS6 and MS9 purity less than 100%.

	Ligand-surrounding interactions (kcal/mol)				Predictions				
comp.	$<E^{vdw}>_{bound}$	$<E^{vdw}>_{free}$	$<E^{ele}>_{bound}$	$<E^{ele}>_{free}$	ΔG^{LIE}A	ΔG^{LIE}B	IC$_{50}$	ΔG_{exp}	error
6486096	-40.29	-22.79	-26.64	-26.89	-6.46	-6.34	5.80	-7.11	0.65
5851689	-50.78	-34.48	-26.26	-27.60	-6.38	-6.04	5.80	-7.11	0.73
5860305	-51.28	-28.61	-36.35	-31.27	-6.54	-7.30	4.90	-7.21	0.09
6446861	-43.71	-23.13	-34.46	-33.98	-6.80	-7.33	1.80	-7.80	0.47
6218896	-55.82	-34.51	-27.02	-26.54	-6.91	-7.59	3.90	-7.34	0.25
5680998	-51.28	-28.17	-36.35	-34.75	-7.02	-8.05	2.30	-7.65	0.40
5545264	-46.61	-23.87	-29.14	-29.32	-7.19	-8.22	1.50	-7.91	0.31
5875121	-52.01	-25.25	-39.22	-32.71	-6.94	-8.52	3.80	-7.36	0.42
5966223	-48.93	-26.43	-32.49	-30.92	-6.94	-7.83	2.80	-7.54	0.29
6060663	-43.25	-17.07	-38.40	-34.78	-7.21	-8.81	3.50	-7.41	0.20

6194121	-45.10	-23.48	-50.81	-48.71	-6.75	-7.42	5.70	-7.12	0.30
6568425	-42.53	-21.09	-50.72	-48.57	-6.73	-7.36	5.50	-7.15	0.21
7093707	-52.85	-30.73	-39.09	-43.50	-7.61	-8.71	2.20	-7.69	0.08
5483251	-39.25	-20.91	-42.32	-40.22	-6.30	-6.25	6.50	-7.05	0.75
AR5	-42.30	-22.01	-34.34	-30.85	-6.40	6.72	8.60	-6.85	0.13
MS5	-42.71	-23.65	-35.17	-32.87	-6.37	-6.47	13.50	-6.59	0.12
MS17	-55.32	-34.67	-38.13	-36.65	-6.69	-7.18	5.20	-7.15	0.03
MS13	-47.39	-27.42	-34.48	-29.60	-6.19	-6.36	3.40	-7.40	1.04
MS6	-34.44	-16.40	-29.89	-28.04	-6.28	-6.18	35.60	-6.02	0.16
MS9	-33.73	-14.64	-45.24	-40.21	-6.05	-6.02	61.60	-5.70	0.32
MS10	-39.95	-19.48	-37.13	-28.92	-5.86	-5.97	11.70	-6.67	0.70
MS11	-37.75	-19.25	-26.78	-25.94	-6.47	-6.52	10.90	-6.71	0.19
MS15	-45.30	-26.85	-30.98	-20.16	-5.26	-4.80	6.60	-7.02	1.76
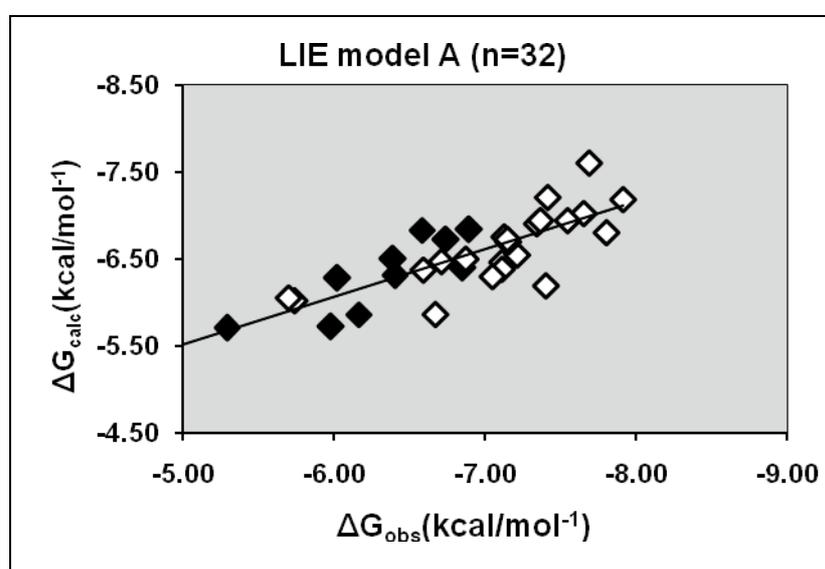
Figure 80: Correlation between observed ΔG_{obs} values and calculated ΔG_{calc} values for LIE model A, black points represent training set and white test set compounds after removing outlier compound MS15.
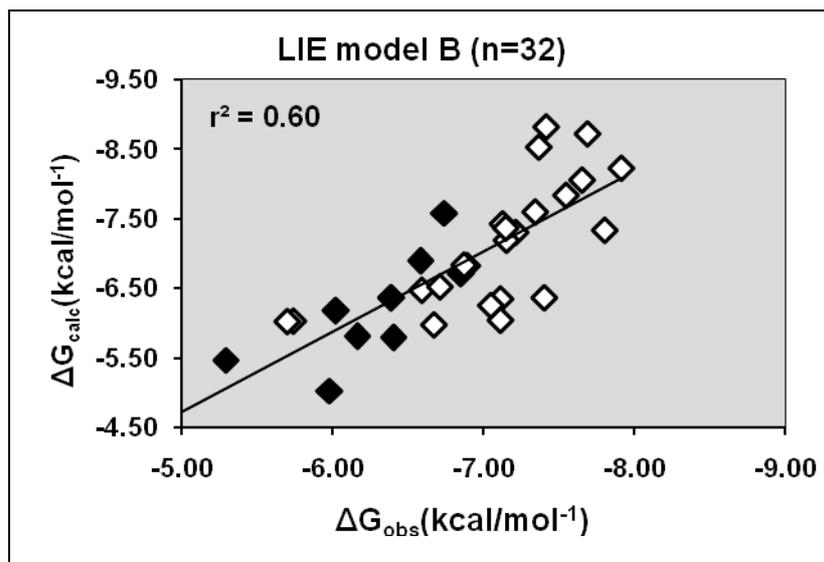
Figure 81: Correlation between observed (ΔG_{obs}) and calculated (ΔG_{calc}) values for LIE model A after compound MS15 was removed. Black points represent training set compounds, and white represent test set compounds.

6.3 Analysis of Inhibitor Binding Mode

The docking poses of the new thiobarbiturates were analyzed by means of MD simulations. All inhibitors showed the same binding mode (Figure 82). They make hydrogen bonding contacts with His187 and Gln167. The one of active inhibitor (compound 5680998, IC_{50}=2.3 µM) binds inside the C-pocket and makes hydrogen bonds to Gln167 and His187. The naphtyl ring of this compound binds deep inside the acetyl-lysine channel (Figure 82, 83). Other active thiobarbiturates show interactions with the residues of the acetyl-lysine channel.
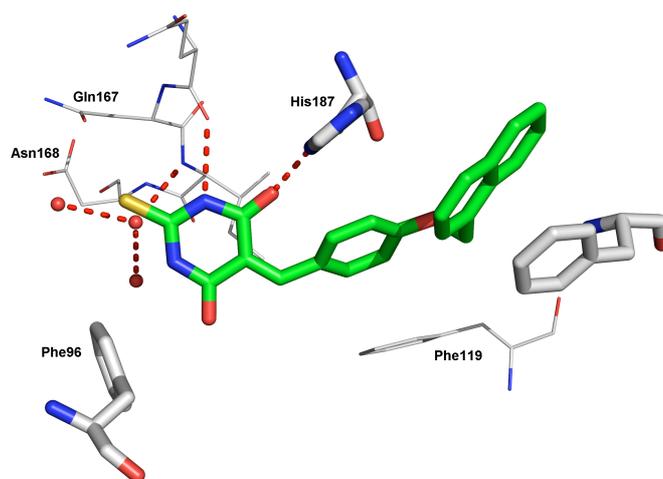
Figure 82: Binding mode of compound 5680998 (IC_{50}=2.3µM) at SIRT2.
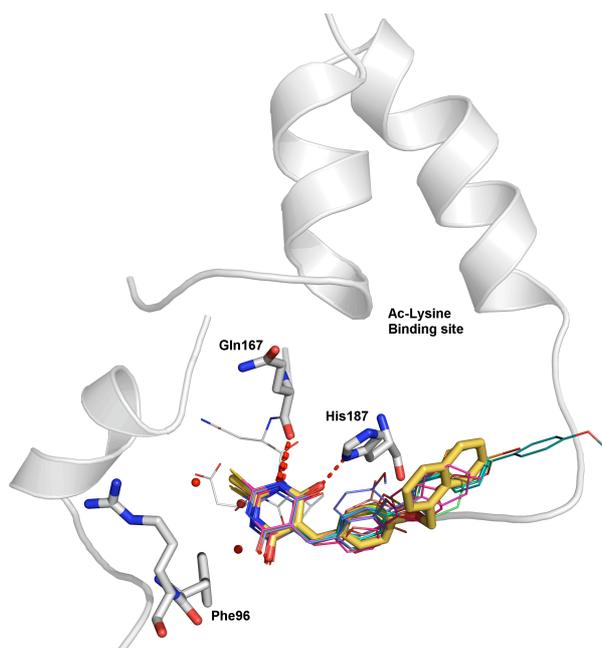
Figure 83: Binding mode of new thiobarbiturate compounds at SIRT2. The most active compound 5680998 is coloured in yellow (capped sticks).

The MD simulations were carried out for five nanoseconds. Coordinates were sampled every 250 steps, and RMSD values were calculated with respect to the crystal structure and remained stable (~2Å) for all inhibitors. Exemplarily, the RMSD plot of compound 5680998 is presented in (Figure 84). The RMSD plot shows that the compound 5680998 reaches an equilibrium state beyond 3000 ps of the simulation time, and this steady state is maintained throughout the simulation (within 2Å).
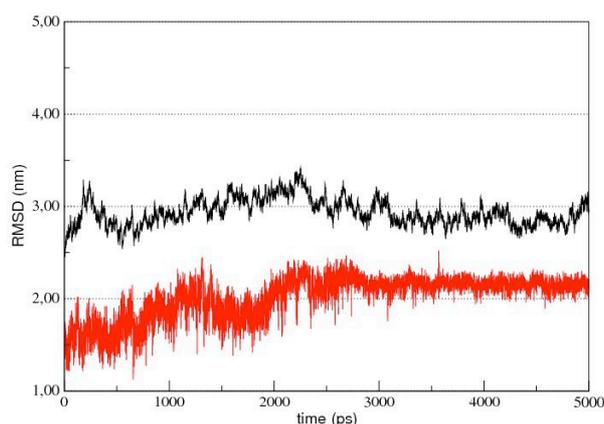
Figure 84: Root mean square deviations (RMSD) plot representing human SIRT2 (black) in complex with thiobarbiturate 5680998 (red line for the inhibitor, IC_{50}=2.3μM).

The RMSD value of the protein-inhibitor complex fluctuates around three nanoseconds, which can be attributed to the movement of the flexible loop (see Figure 83, 84). We also

observed the flexible loop closes the nicotinamide pocket of SIRT2. This causes a slight shift of the ligand towards the acetyl-lysine binding site, which is potentially driven by movement of the flexible loop, and opening of the binding tunnel (Figure 85). The same movements were observed for compound 5545264 (IC_{50}=1.5μM) (Figure 86). In both examples, strong hydrogen bonds to Gln169 and His187 were found.
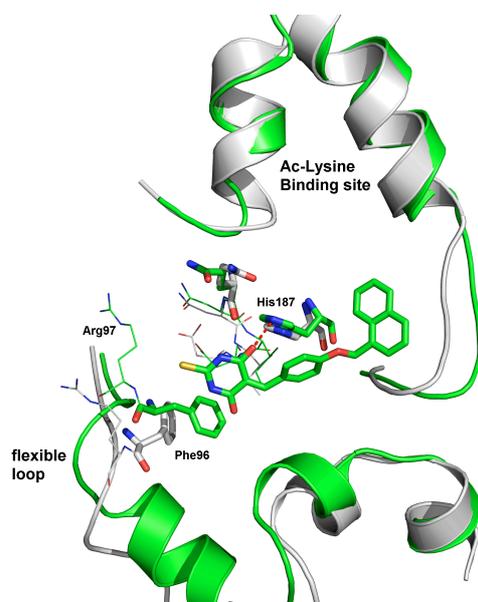
Figure 85: Superposition of human SIRT2 X-ray structure (white) and snapshot (green) taken from the last trajectory of the MD simulations. The inhibitor 5680998 is shown as green capped stick.
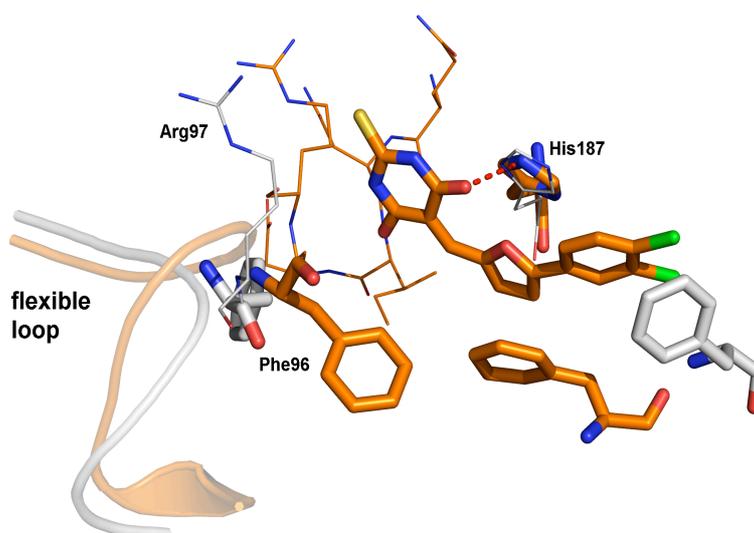
Figure 86: Superposition of human SIRT2 X-ray structure (white) and a snapshot taken from the last trajectory of MD simulations. The inhibitor 5545264 is shown as orange capped stick.

6.4 Binding Free Energy Prediction for Inactive Compounds

Some of the selected compounds were found to be inactive on human SIRT2 (Figure 87). MD simulations were run to check the stability of these complexes. Binding mode analysis showed that complexes were stable during simulations and hydrogen bond to Gln167 was observed (Figure 88). The RMSD of the ligands oscillates below 2Å for all three compounds (Figure 89), which is indicative of their stability in the nicotinamide subpocket. Visual inspection of the trajectory files showed that the binding of these compounds did not induce a shift in the flexible loop or the acetyl-lysine binding pocket, whereas significant fluctuations on these parts of the protein were observed while the active thiobarbiturate inhibitors bind (Figure 52, 57, 68, 85). To better understand the inactivity of these compounds on human SIRT2, binding free energy calculations were carried out using MM-PBSAand LIE approach.
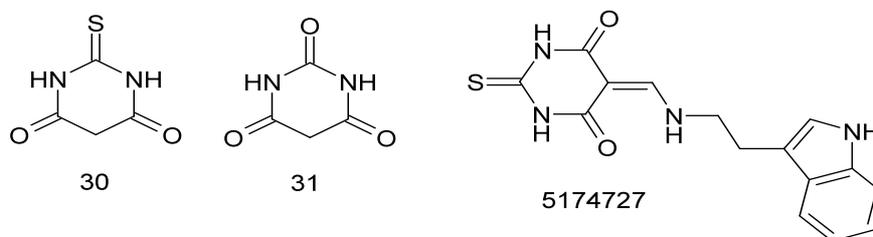
Figure 87: Inactive compounds.

Binding free energies of three inactive compounds were predicted using parameters obtained from the training set models. In case of the MM-PBSA approach, (Table 21) both the enthalpy model (ΔH_{pred}) and the binding free energy model (ΔG_{pred}) overestimated the binding affinities for compounds with lower inhibition values. Only separately calculated binding free energies (ΔG_{calc}) agreed well with the experimentally obtained values (Table 21). The interaction energy of compound 30 and 31 showed to be highly unfavourable (8.22 kcal/mol and 5.21 kcal/mol, respectively). The enthalpy of these two compounds was low (-5.55 kcal/mol and -9.34 kcal/mol), which suggests that the enthalpy values may not be sufficient to counterbalance the entropy effect (Table 21). In case of compound 5174727, the calculated binding affinity was not very favourable (-0.64 kcal/mol), which suggests unfavourable binding.

Table 21: Energy contributions to the free energy of binding of the three inactive compounds (30, 31 and 5174727) obtained by the MM-PBSAapproach, ΔE_{el} and ΔE_{vdw} are respectively the electrostatic and van der Waals energies of binding; ΔG_{el}: electrostatic contributions to the solvation free energy; ΔG_{nonel}: non-electrostatic contributions to solvation free energy; ΔH_{tot} is the enthalpy of binding, $T\Delta S_{tot}$ is the entropy of binding and ΔG_{calc} is the calculated binding free energy, ΔH_{pred} energies predicted based on the calculated enthalpy of binding, ΔG_{pred} energies predicted based on the binding free energy values.The active compound 5680998 is shown to compare the individual energy terms.

comp	ΔE_{el}	ΔE_{vdw}	ΔG_{el}	ΔG_{nonel}	ΔG_{sol}	ΔH_{tot}	ΔH_{pred}	$T\Delta S_{tot}$	ΔG_{calc}	ΔG_{pred}	$IC_{50}[\mu M]$
30	-6.88	-17.02	20.91	-2.55	18.36	-5.55	-5.07	-13.77	8.22	-3.91	Inactive
31	-4.63	-17.41	15.49	-2.78	12.71	-9.34	-5.46	-14.55	5.21	-4.51	Inactive
5174727	-21.08	-28.31	34.06	-4.79	29.27	-20.12	-6.58	-19.48	-0.64	-5.68	Inactive
5680998	-16.03	-43.68	31.05	-6.34	37.39	-28.66	-7.46	-18.25	-10.41	-7.63	2.3

The three inactive thiobarbiturate compounds were also tested using LIE models A and B (Table 22). Only model B correctly predicted the biological data for compounds 30 and 31. The obtained binding energies (-2.44 kcal/mol and -3.04 kcal/mol) are indicative of unfavourable binding. The binding affinity of compound 5174727 was correctly predicted (3.03 kcal/mol). These results suggest that LIE model B is sensitive enough to discriminate between active and inactive compounds. In the case of LIE model A, predicted biological values were highly overestimated in comparison to the experimental data. One reason for that may be the additional constant γ, which improved the correlation coefficient of training set compounds but did not account for inactive derivatives.

The detailed analysis of the electrostatic, van der Waals and solvation contributions to the binding can be used to understand the inactivity of these three compounds (Table 21). Upon binding of inactive compounds, the electrostatic energy ΔE_{el} is favourable in all cases, and electrostatic contribution of the solvation energy (ΔG_{el}) is disfavorable which altogether sum to disfavorable electrostatic contribution ($\Delta E_{el} + \Delta G_{el}$) to the enthalpy of binding by 14.03 kcal/mol, 10.86 kcal/mol and 12.98 kcal/mol for compounds 30, 31 and 5174727 respectively (Table 21). The van der Waals interaction energy (ΔE_{vdw}) associated with non-polar contributions to the solvation energy (ΔG_{nonel}) yielded a total vdW/hydrophobic energy ($\Delta E_{vdw} + \Delta G_{nonel}$) of -19.57 kcal/mol, -20.19 kcal/mol and -33.10 kcal/mol for compounds 30, 31 and 5174727 respectively (Table 21). The opposite of true is the active compound 5680998. The electrostatic contribution to solvation energy yield by (21.36 kcal/mol) and a total vdW/hydrophobic energy ($\Delta E_{vdw} + \Delta G_{nonel}$) showed to be higher (-50.02 kcal/mol). In all examples, the favourable vdW/hydrophobic energy compensates the disfavorable effects of electrostatic interactions at the binding interface, which sums to a favourable process binding

driven by vdw/hydrophobic forces in solution. As can be seen the vdW/hydrophobic energy of compound 5680998 is ~20kcal/mol and is more favourable than the energies of the inactive compounds which maybe one of the reasons why the binding free energy obtained from MM-PBSA method is disfavorable. As the compounds bind to the hydrophobic part of the human SIRT2 pocket, the vdW/hydrophobic energy should be more favourable than that observed for compounds 30, 31 and 5174727.

	Ligand-surrounding interactions (kcal/mol)				Predictions		
comp.	$\langle E^{vdw}\rangle_{bound}$	$\langle E^{vdw}\rangle_{free}$	$\langle E^{ele}\rangle_{bound}$	$\langle E^{ele}\rangle_{free}$	$\Delta G^{LIE}A$	$\Delta G^{LIE}B$	IC_{50}
30	-15.90	-6.11	-31.72	-25.35	-6.12	-2.44	Inactive
31	-17.36	-5.41	-28.36	-20.92	-6.55	-3.04	Inactive
5174727	-41.44	-27.14	-39.58	-30.73	-3.60	+3.03	Inactive

Table 22: Overview of the electrostatics (ΔE_{ele}) and van der Waals (ΔE_{vdw}) energies (kcal/mol) obtained for three inactive compounds, ($\Delta G^{LIE}A$) values predicted with a fitting parameter $\gamma \neq 0$, and ($\Delta G^{LIE}B$) with fitting parameter $\gamma=0$.
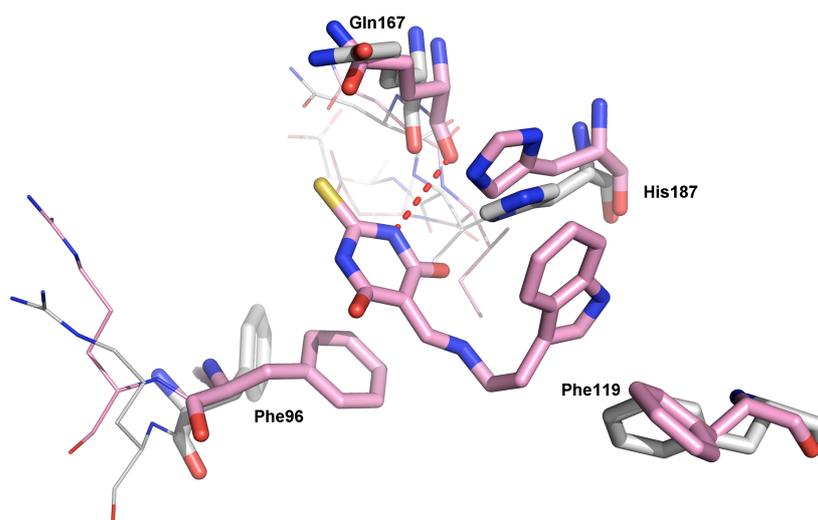
Figure 88: Superimposition of human SIRT2-Xray structure (white) and snapshot taken from the last trajectory of MD simulations. Inactive compound 5174727 is shown in magenta.
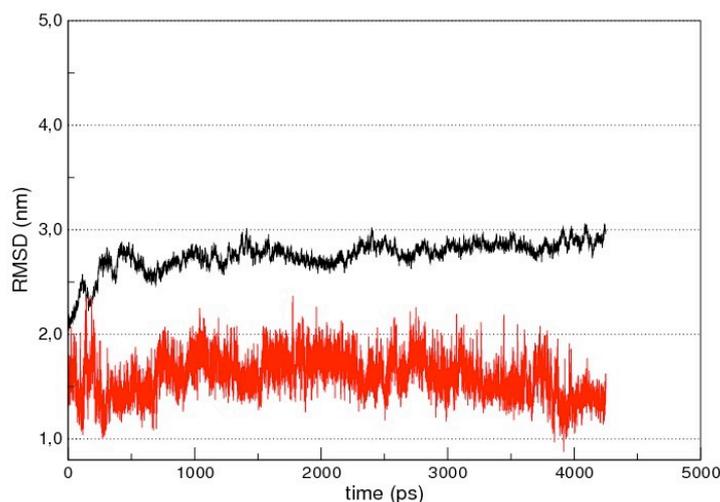
Figure 89: Root mean square deviations (RMSD) plot representing human SIRT2 (black) in complex with thiobarbiturate 5174727 (red line for the inactive inhibitor).

All three inactive compounds were calculated as neutral molecules. The two barbituric acids may occurred in deprotonated form under physiological conditions, and compound 5174727 as an amine exists mainly in the protonated form. However, the parameters obtained for the training set models from MM-PBSA and LIE were generated solely from neutral non-protonated compounds. Thus we could not use the charged state of the three compounds for binding affinity predictions. To test the influence of the protonation state, additional separate MM-PBSA calculations were carried out. The deprotonated babituric acids compounds 30, 31 (Figure 87) showed highly unfavourable binding free energies of 9.30 kcal/mol and 6.12 kcal/mol, respectively. Also, the binding free energy of the protnated form of 5174727 is positive (10.09 kcal/mol). These calculations clearly showed that the charged forms, which may exist under physiological condition, are not able to bind to SIRT2.

6.5 Conclusion

We demonstrated that LIE and MM-PBSA methods could be applied to accurately estimate the free energy of binding for a range of compounds with varying inhibition potencies. Different computational models were evaluated for the prediction of the biological data of compounds indentified through Virtual Screening or which were subsequently synthesized on the basis of the docking results. The MM-PBSA enthalpy model yielded a significant regression model (r^2=0.78). The model provided the correct ranking of the novel compounds identified through Virtual Screening and synthesis. The addition of an entropy term to the model decreased the correlation coefficient (r^2=0.46).

Two LIE models (A and B) were tested with the same data set of thiobarbiturates, and both LIE models yielded satisfactory free energy predictions considering their simplicity and short simulation time. Introducing a constant γ did not improve the predictivity of model A, as the correlation coefficient obtained for the test set was 0.23. The correlation coefficient of model B (r^2=0.49) was better than that of model A, which indicates a better predictive ability of the model. LIE model B was sensitive enough to correctly predict the ranking of inactive compounds, whereas model A highly overestimated the results. Overall, the predicted binding energies for the all 23 thiobarbiturate compounds using LIE equation and MM-PBSA method were in good agreement with the experimental IC_{50} values.

Chapter 7

7 Discussions and Outlook

Simulation time is an important factor in deciding the proper computational strategy for the prediction of the potency of a set of ligands. Static methods are fast, and only require a single step of minimization, whereas dynamic methods consider protein flexibility and solvation effects and are thus more computationally expensive. We used different binding free energy methods to study the binding of untested ligands and predict their biological activities. Multi-step Virtual Screening approaches were used to identify novel and potent sirtuin inhibitors from commercial compound libraries.

First, the static methods LR-MM-PBSA and LIECE were applied to the same training set of thiobarbiturate inhibitors (Figure 52, 65), in which only a single protein-inhibitor conformation derived from minimization was used to evaluate quantitative models. Both methods yielded poor statistical values (r^2=0.36 and r^2=0.30 for LR-MM-PBSA and LIECE respectively) because these methods do not account for movement of the flexible loop and acetyl-lysine binding tunnel, which appears to be an important step in the binding of ligands to human SIRT2.

We also used the dynamic LIE and MM-PBSA methods to predict binding free energies. When we developed the LIE models with 10 thiobarbiturate inhibitors, the best training set fit was evaluated with α=0.14, β=-0.12 and γ=-3.98 (r^2=0.74) for model A, and α=0.36, β=-0.17 and γ=0 (r^2=0.58) for model B. We were able to obtain good predictions for 23 test set compounds with both models, and model B also correctly predicted energies for three inactive ligands. The IC_{50} values of our training set were between 8.1-130μM and the experimental IC_{50} values for test set compounds showed that they are more active. For this reason it might be difficult to obtain good predictions using such training set, and the inclusion of compounds with IC_{50} values lower than 8.1μM will be necessary to improve these models.

The most significant advantage of LIE over MM-PBSA is the shorter simulation time. We initially pursued LIE calculation of binding affinities because of the shorter MD simulation required for LIE over that of MM-PBSA. We firstly generated snapshots between 400-500ps, but as we did not obtain good statistical models for training set compounds, simulation time was extended up to 1ns. This corresponds approximately to 7 h per ligand simulation; two

simulations were performed per ligand, which can be easily parallelized. For our 23 compounds of the test set we needed about 322 hours. This shows that the dynamic LIE application could not be applied to estimate binding affinities for thousands of compounds. In the case of metalloprotenase inhibitors, Sylte *et al*. did not find acceptable binding free energy until their MD simulations were extended to 5ns, which further exemplifies the potential weaknesses of short simulation times [186]. Alternatively, the 5ns of MD would be also enough time to generate reliable binding affinities using MM-PBSA.

Another weakness of the LIE method is that the results can be heavily influenced by the fitting parameters, and these parameters have been shown to depend on the system being studied and force field used. In many cases specific calibrations of the LIE equation have to be carried out to obtain reasonable binding energies. As an example the predicted binding free energies for thrombin inhibitors were obtained with $\alpha=0.328$, $\beta=0.180$ and a constant γ of -4.21 kcal/ (mol $\mathring{A}^2$) [187]. Gorse and Gready applied the standard LIE equation to series of N5-deazapterins to DHFR, and obtained a good fit with experimental data with $\alpha=-0.32$, $\beta=0.5$ and $\gamma=0$ [188]. The three fitting parameters obtained for thapsigargin-based inhibitors were $\alpha=0.072$, $\beta=-0.0004$ and $\gamma=1.228$ [189]. Recently Wang *et al*. used the LIE approach and included and extra entropy term in study of avidin-biotin system [190]. The entropy term involved the fluctuations of the interaction energy around its average. Here the LIE equation was solved in a fashion similar to that of QSAR models.

The major difficulty associated with MM-PBSA approach is the evaluation of the change of conformational entropy. Such calculations are computationally expensive, and the results are often inaccurate. One approach is to omit entropy calculations from MM-PBSA and use only enthalpy terms for predictions binding affinities. We found our MM-PBSA model of thiobarbiturate inhibitors without an entropy term gave better statistical results and predictions of active inhibitors. However, we found it necessary to use the entropy term to correctly distinguish between active and inactive compounds.

An additional advantage of MM-PBSA is that it does not require empirical parameters that are affected by the nature of the ligand-protein interaction, which makes MM-PBSA method better in dealing with ligands that differ significantly in their structural and chemical composition. The correlation between 15 splitomicin derivatives and 5 thiobarbiturates and experimental data was ($r^2=0.69$) for MM-PBSA, whereas the correlation for the LIE approach using the same data was much lower ($r^2=0.20$). Therefore, any future binding free energy

calculations or virtual screenings that will consider a wide variety of ligand scaffolds should be conducted using MM-PBSA, and not with LIE.

In the statistical analyses conducted for both LIE and MM-PBSA models, the calculated binding free energies were directly compared to experimentally measured IC_{50} values. IC_{50} and K_i values are related by a proportionality factor, and the relationship is not perfect [191-193]. The pK_i and ΔG form a strict linear correlation ($\Delta G = -RT\ln(K)$), however the correlation between pIC_{50} and ΔG is not expected to be linear. Our statistical models could therefore be greatly strengthened if they were based on K_i values, and not only IC_{50} values.

Chapter 8

8. Summary

NAD^+-dependent histone deacetylases (sirtuins) are enzymes that cleave acetyl groups from N-acetylated lysines of histones and non-histone proteins. SIRT2 proteins are conserved from bacteria to humans, and deacetylate numerous non-histone targets such as α-tubulin, myoD, p53 and FOXO. Their ability to deacetylate such a wide range substrate implicates them to play an important role in various biological processes, including DNA recombination, repair and longevity and transcriptional silencing. However, potent and subtype-selective inhibitors are needed to further analyze the function of human Sir2 enzymes. The main goal of this work was to gain insight into the molecular binding of inhibitors at human SIRT2, and to identify new compounds which represent interesting tools to analyze the therapeutic potential of sirtuin inhibitors.

We described two potential binding modes of NAD^+ to human SIRT2, including a productive and non-productive conformation. MD simulations showed a conformational transition of the flexible loop and substrate binding tunnel from an open to more closed conformation upon binding of NAD^+. MM-PBSA calculations were applied to investigate the stability of the NAD^+ binding mode and binding mechanism. Hydrogen bond analysis was applied in order to specify important hydrogen bonds and to select residues with the highest contribution to the binding. The same residues were found experimentally to be important in yeast Sir2.

We identified potent inhibitors of human SIRT2, namely β-phenylsplitomicin derivatives. Docking studies showed that the orientation of the β-phenyl group is important for compounds activity. Crystal water molecules found in the binding cavity of C-pocket significantly improved docking results, and were important in understanding the activity of *R*-enantiomers and inactivity of the *S*-enantiomers. MD simulations showed the stability of these compounds in the nicotinamide subpocket of human SIRT2. Using MM-PBSA approach, binding free energies were estimated and compared with experimental data. The method showed to be sensitive enough to correctly discriminate between active and inactive enantiomers.

Thiobarbiturate derivatives were also identified as novel inhibitors of human SIRT2. Virtual screening, docking and binding free energy calculations were used here to predict binding

mode and activities for a set of thiobarbiturate compounds. The MM-PBSA method reproduced the experimental data with an r^2=0.78, whereas the best LIE model gave a correlation coefficient of r^2=0.58. Both methods could correctly interpret the compounds with the best biological activities. These models provide a validation of the combination of docking, MD simulations and binding free energy calculations as a powerful tool in structure-based drug design.

Chapter 9

Computational Details

9.1 Docking Studies

Molecular Modeling Studies of human SIRT2

The published X-ray structure of human Sirt2 (PDB code: 1J8F) at 1.7Å resolution reflects three identical sub-domains each having 300 residues with identical sequence, namely domain-A, domain-B and domain-C [70]. The SIRT2 human type crystallizes as a trimmer, the three domains are identical thus for docking studies only one domain was considered. Docking of NAD^+ into the most likely binding sites on domain B was implemented by DOCK v6.1 (UCSF) suite of programs [108]. The waters and zinc ions were not included in docking studies. For docking studies, contributed force field parameters along with coordinates and partial atomic charges by Walker *et* al were used [192, 193].

Identification of SIRT2 Inhibitors

All calculations were performed on a Pentium IV 2.2 GHz based Linux cluster (20 CPUs). The molecular structures of the inhibitors were generated using the MOE modeling package (Chemical Computing Group). The structures were energy minimized using the MMFF94s force field and the conjugate gradient method until the default derivate convergence criterion of 0.001 kcal $(molx\text{Å})^{-1}$ was met. The crystal structure of human SIRT2 (PDB code: 1J8F) was taken from the Protein Data Bank. Docking of the inhibitors was carried out with the program GOLD 3.2 [109] and default settings were applied. Four co-crystallized water molecules, which can be observed in the nicotinamide binding pocket of the different SIRT2 monomers (A, B and C) were included for ligand docking. GOLD offers the possibility to replace or use water molecules as mediators for protein-ligand interactions (water toggle mode). All torsion angles in each inhibitor were allowed to rotate freely. The binding site was defined on Ile169 with radius of 15Å. GoldScore was chosen as fitness function. For each molecule, 10 docking runs were performed. The resulting solutions were clustered on the basis of the heavy atom RMSD values (1Å).

9.2 Molecular Dynamics Simulations

Molecular Modeling Studies of human SIRT2

107

Molecular dynamics (MD) were carried out using AMBER 9.0 and the AMBER1999SB force field [150]. The initial structure of human-type SIRT2 (sitruin) was obtained from crystal structure (PDB code 1J8F [70]. The ligand parameters were taken from general AMBER force field (GAFF) [194]. Atom types were assigned to the atoms of NAD^+ by the *antechamber* module of AMBER v9 [195], which were then saved in GAFF mol2 format file. Coordinates and partial atomic charges in the GAFF mol2 file of NAD^+ were replaced with those obtained from the docked NAD^+. The GAFF force field parameters for NAD^+ of were prepared by the *parmchk* module of AMBER v9 [150]. In the crystal structure of human SIRT2, each domain is associated with a divalent zinc ion coordinated to four cysteine side groups. The divalent zinc ion was handled by a cationic dummy atom (CaDA) approach of Pang *et al*. [196, 197], which treats the zinc ion as tetrahedron-shaped divalent cation with dummy atoms filling the tetrahedral corners. Parameters and libraries for the tetrahedral-zinc group and anionic cystein residues were obtained from Pang *et al* and were used as inputs for LEAP according to a procedure described by Pang Lab [198].

Preparation of the NAD^+ and SIRT2 complex, addition of counterions, solvation, and preparation of parameter/topology and coordinate files were all implemented in LEAP. Anionic cystein residues that coordinate the zinc divalent ion were given a residue name "CYM" and the Zn ion was marked as "ZNB" in the pdb files of the domain as described by Pang Lab [198]. The domain B human SIRT2 was combined by LEAP using AMBER1999SB force field [150] and parameters and libraries for CYM and ZNB residues defined by Pang et. al. [198]. The 10 Na^+ counter ions were added to neutralize the complex system. The complex molecule was solvated by putting together small units of TIP3 water boxes in dimensions of 18x18x18Å. The 11780 TIP3 water molecules were added to solvate the complex constituting a molecular dynamics (MD) system with a total of 40174 atoms (including water molecules, ions and the complex). The distance between the outer boundary of the octahedral solvent box and the solute surface was set to 10Å. A space of 0.4Å was used to set water molecules at the solvent boundary.

Relaxation, temperature equilibration and molecular dynamics routines were conducted for the complex molecule by the *sander* module of AMBER v9 [150]. The coordinates of Zn^{2+} and Na^+ cations, NAD^+ and water molecules in the starting complex structure were initially relaxed in three steps to remove bad close contacts. In the first step, the tetrahedron-shaped zinc divalent cations were relaxed through a short restrained minimization routine for 0.1 ps using a steepest descent minimization method with 1 fs time steps over 100 iterations, during which the atom coordinates for the solute (including amino acid residues and NAD^+) were

restrained to their initial coordinates with a force constant of 500 kcal/mol.Å. In the second step, NAD$^+$ and the zinc divalent cations were relaxed for 0.5 ps with 1 fs time steps over 500 iterations, during which the atom coordinates for the aminoacid residues of protein were restrained to the X-ray coordinates with a force constant of 500 kcal/mol.Å. In the final minimization step, restraints to atoms were removed and the complex system was relaxed for 1 ps with 1 fs time steps over 1000 iterations. The temperature of the relaxed system was then equilibrated at 300K through 20 ps of MD using 2 fs time steps over 10000 iterations. A constant volume periodic boundary was set to equilibrate the temperature of the system by the Langevin dynamics [199] using a collision frequency of 10 ps^{-1} and a velocity limit of 5 temperature units. During the temperature equilibration routine, the complex structure in the solvated system was restrained to its initial coordinates with a weak force constant of 10 kcal/mol.Å. The final coordinates of the temperature equilibration routine (after 20 ps) was then used to complete a 1000 ps (1.0 ns) molecular dynamics routine using 2 fs time steps through 500000 iterations, during which the temperature was kept at 300 K by the Langevin dynamics. The pressure of the solvated system was equilibrated at 1 bar at a certain density in a constant pressure periodic boundary by an isotropic pressure scaling method employing a pressure relaxation time of 2 ps. During the temperature equilibration and MD routines, a non-bonded cutoff distance of 9Å was applied to handle electrostatic interactions in periodic boxes by the Particle Mesh Ewald method [200] and SHAKE method [201] was applied to keep the bond lengths of protons attached to heteroatom constant. Coordinates and energy outputs for the relaxation and the molecular dynamics routines were saved every 250 iterations.

Identification of SIRT2 Inhibitors

Molecular dynamic computations were carried out using AMBER 9.0 and the AMBER 1999SB force field [150]. We focused MD simulations on inhibitors tested in our laboratory in the same biological in vitro assay. The initial structures of the SIRT2-inhibitor complexes were taken from the GOLD docking study. The ligand force field parameters were taken from the general amber force field (GAFF) [195], whereas AM1 ES atomic partial charges were assigned to the inhibitors. In the crystal structure of human SIRT2, each domain is associated with a divalent zinc ion coordinated to four anionic cysteine side groups. The divalent zinc ions were represented by the cationic dummy atom (CaDA) approach of Pang *et al.* as described in section 9.2.1. The SIRT2-inhibitor complexes were solvated in water

boxes (TIP3) with the dimensions 18x18x18 Å. Periodic boundary conditions were applied, resulting in a final system with dimensions of approximately 90x90x90 Å. The distance between the outer boundary of the octahedral solvent box and the solute surface was set to 10 Å. Parameter/topology and coordinates files for the neutralized/solvated system were prepared using LEAP module of AMBER. Eight sodium ions were added as counterions to neutralize the system. MD simulations were carried out using the same procedure like described in section 9.2.1.

9.3 MM-PBSA Calculations

The MM-PBSA method is characterized by the use of Poisson-Boltzmann (PB) model to compute the electrostatic component of the solvation free energy. The binding free energy of the protein-ligand complex is approximated by the equation (12).

$$\Delta G = \Delta H - T\Delta S \tag{12}$$

in which T is the temperature of the system at 300K. The binding free energy (ΔG) of the protein-ligand complex is computed as:

$$\Delta G = G_{complex} - [G_{protein} + G_{ligand}] \tag{13}$$

where $G_{complex}$ is the absolute free energy of the complex, $G_{protein}$ is absolute free energy of the protein, and G_{ligand} is the absolute free energy of the ligand. We extracted 100 snapshots (at time intervals of 2ps) for each species (complex, protein and ligand) from the last 200ps of the MD simulations of the complexes. The enthalpy term on equation (12) is dissected into subenergy terms:

$$H_{tot} = H_{gas} + G_{solv} \tag{14}$$

$$H_{gas} = E_{el} + E_{vdw} + E_{int} \tag{15}$$

where H_{gas} is the potential energy of the solute, which is determined as the sum of the can der Waals (E_{vdw}), electrostatic (E_{el}) and internal energies (E_{int}) in the gas phase by using SANDER module of AMBER [150]. G_{solv} is the solvation free energy for transferring the

solute from vacuum into solvent and is a sum of electrostatic (G_{el}), and non-electrostatic (hydrophobic) contributions (G_{nonel}) as shown in equation (16).

$$G_{solv} = G_{el} + G_{nonel} \qquad (16)$$

G_{el} in equation (16) was computed at 0.15 M salt concentration by the PBSA module of AMBER v9 by dividing implicitly solvated solute species into 0.4Å cubic grid points and summing up the electrostatic potentials computed at each grid point. Electrostatic potential $\varnothing_{(r)}$ at a grid point r that is not at the solvent-solute boundary was computed by a linear Poisson Boltzmann (PB) equation [160], which is a three-dimensional vector differential equation as in (17).

$$\nabla\,\varepsilon_{(r)} \nabla\,\varnothing_{(r)} \;=\; -\,4\,\pi \cdot \rho_{(r)} \qquad (17)$$

where $\varepsilon_{(r)}$ is the dielectric constant ($\varepsilon=1$ for the solute interior and $\varepsilon=80$ for implicit PB water) and $\rho_{(r)}$ is the charge density. The grid point potentials were then summed up for each atom i to yield atomic potentials $\varnothing_i$.

The absolute entropy was computed for each solute species by normal-mode analysis [160] integrated in the *nmode* module of AMBER v9. An ensemble of different conformations was extratced from the MD trajectories, and each snapshot was analyzed by applying the MM-PBSA method. The total entropy (S_{tot}), as formulated in equation (18) arose from changes in the degree of freedom translational (S_{trans}), rotational (S_{rot}), and vibrational (S_{vib}) of each species.

$$S_{tot} = S_{trans} + S_{rot} + S_{vib} \qquad (18)$$

Considering all absolute energy terms as given in equation (13), the binding free energy ΔG takes the following form:

$$\Delta G = [\Delta H_{gas} + \Delta G_{solv}] - T\Delta S_{tot} \qquad (19)$$

Parameter/topology files used in MM-PBSA computations were prepared for the complex, the protein, and the inhibitors using the LEAP module. Snapshots extracted from trajectories were pre-minimized in the gas phase by the SANDER model. Frequencies of the vibrational modes were computed at 300K for these minimized structures including all snapshots atoms and using a harmonic approximation of the energies.

Bibliography

[1]   C.H Waddington. The epigenotype, *Endeavour 1*, 18-20, 1942.

[2]   Jaenish, R. and Bird, A. Epigenetic regulation of gene expression: how the genome integrates intrinsic and environmental signals. *Nat.Genet.* 33, 245-254.

[3]   Bird, A. DNA methylation patterns and epigenetic memory. *Genes Dev.* 16, 6-21, 2002.

[4]   Jones, P. A. and Baylin, S. B. The fundamental role of epigenetic events in cancer. *Nat. Rev.* 3, 415-428, 2002.

[5]   Jinek, M., and Doudna, J., A three-dimensional view of the molecular machinery of RNA interface. *Nature* 457, 405-412, 2009.

[6]   Biel, M., Wascholowski V., Giannis, A., Epigenetics −An epicenter of gene regulation: histones and histone-modifying enzymes. *Angew. Chem. Int. Ed.* 44, 3186-3216, 2005.

[7]   Egger, G., Liang, G., Aparicio, A. and Jones, P.A. Epigenetics in human disease and prospects for epigenetic therapy. *Nature* 429, 457-463, 2004.

[8]   Berger, S. L., Histone modifications in transcriptional regulation. *Curr. Opin. Genet. Dev.* 12, 142, 2002.

[9]   Shiio, Y., Eisenman, R.A. Histone sumoylation is associated with transcriptional repression. *Proc. Natl. Acad. Sci.* 100, 13225-13230, 2003.

[10] Segal, E., Fondufe-Mittendorf, Y., Chen, L., Thaström, A. Ch., Field, Y., Moore, I., Ping, Ji. Wang, Z., and Widom, J., *Nature* 442, 772-778, 2006.

[11]   Jenuwein, T., Allis, C. D. Translating the histone code. *Science* 293, 1074-1080, 2001.

[12] Johnson, L., Cao, X. and Jacobsen, S. Interplay between two epigenetic marks. DNA methylation and histone H3 lysine 9 methylation. *Curr. Biol.* 12, 1360-1367, 2002.

[13] Bird, A. P., and Wolffe, A. P., Methylation-induced repression-belts, braces and chromatin. *Cell* 99, 451-454, 1999.

[14] Verdin, E., Dequiedt, F., Fischle, W., Frye, R., Marschall, B., North, B., Measurment of mammalian histone deacetylase activity. *Metchods Enzymol.* 377, 180-196, 2004.

[15] Kustatscher, G. Splicing regulates NAD metabolite binding to histone macroH2A. *Nat. Struct. Mol. Biol.* 12, 624-625, 2005.

[16] Stefan. S., and Jung, M., Chromatin Modifications as Targets for New Anticancer Drugs. *Archiv der Pharmazie*, 338, 347-357, 2005.

[17] Markus, B., Veit, W., and Anthanassios, G. Epigenetics –An Epicenter of Gene Regulation: Histones and Histone-Modifying Enzymes. *Angewandte Chemie International Edition.* 44, 3186-3216, 2005.

[18] Somoza, J. R., Skene, R. J., Katz, B. A., Mol, C., Ho, J. D., Jennings, A. J. Luong, C., Arvai, A. Buggy, J. J., Tari, L. W., Structural snapshots of human HDAC8 provide insights into the class I histone deacetylases. *Structure* 12, 1235-1334, 2004.

[19] Vannini, A., Volpari, C., Filocamo, G., Casavola, E. C., Brunetti, M., Renzoni, D., Chakravarty, P., Paolini C., De Francesco, R., Galinari, P., Steinkuhler, C., Di Marco, S., Crystal structure of a eukaryotic zinc-dependent histone deacetylase, human HDAC8, complexed with a hydroxamic acid inhibitor. *Proc. Natl. Acad. Sci. U.S.A* 11, 15064-15069, 2004.

[20] Brachmann, C. B., Sherman, J. M., Devine, S. E., Cameron, E. E., Pillus, L. and Boeke, J. D., The SIR2 gene family, conserved from bacteria to humans, functions in silencing, cell cycle progression, and chromosome stability. *Genes Dev.* 9, 2888-2902, 1995.

[21] Derbyshire, M. K., Weinstock, K. G., and Strathern, J. N. HST1, a new member of the SIR2 family of genes. *Yeast* 12, 631-640, 1996.

[22] Klar, A. J., Seymour, F. and Macleod, K. MAR1-A regulator of the HMa and HMα locus in Saccharomyces cerevisiae. *Genetics* 93, 37-50, 1979.

[23] Shore, D., Squire, M. and Nasmyth, K. A. Characterization of two genes required fort he position effect control of yeast mating-type genes. *EMBO J.* 3, 2817-2823, 1984.

[24] Moazed, D., Kistler, A., Axelrod, S., Rine, J., and Johnson, A. D. Silent information regulator protein complexes in *Saccharomycescerevisiae*: A SIR2/SIR4 complex and evidence for a regulatory domain in SIR4 that inhibits its interaction with SIR3. *Proc. Natl. Acad. Sci. USA,* 94, 2186–2191, 1997.

[25] Gottlieb, S. and Esposito, R. E. A new role of yeast transcriptional silencer gene, SIR2, in regulation of recombination in ribosomal DNA. *Cell* 56, 771-776, 1989.

[26] Aparicio, O. M., Billington, B. L., and Gottschling, D. E. Modifiers of position effect are shared between telomeric and silent mating-type loci on S.cerevisiae. *Cell* 66, 1279-1287, 1991.

[27] Michishita, E., Park, J. Y., Burneskis, J. M., Barrett, J. C., and Horikawa, J. Evolutionarily conserved and nonconserved cellular localizations and functions of human SIRT proteins. *Mol. Biol. Cell* 16, 4623-4635, 2005.

[28] Frye, R. A. Characterization of five human cDNAs with homology to the yeast SIR2 gene: Sir2- like proteins (sirtuins) metabolizes NAD and may have protein ADP-ribosyltransferase activity. *Biochem. Biophys. Red. Commun.* 260, 273-279, 1999.

[29] North, B. J., Marschall, B. L., Borra, M. T., Denu, J. M. and Verdin, E., The human Sir2 ortholog, SIRT2, is an NAD$^+$ -dependent tubulin deacetylase. *Mol. Cell* 11, 437-444, 2003.

[30] Vaziri, H., Dessain, S. K., NgEaton, E., Imai, S. I., Frye, R. A., Pandita, T. K., Guarente, L. and Weinberg, R. A., (2001) hSIR2 (SIRT1) functions as an NAD-dependent p53 deacetylase. *Cell* 107, 149-159.

[31] Haigis, M. C., Mostoslavsky, R., Haigis, K. M., Fahie, K., Christodoulou, D. C., Murphy, A. J., Valenzuela, D. M., Yancopoulos, G. D., Karow, M., Blander, G. et al. SIRT4 inhibits glutamate dehydrogenase and opposes the effects of calorie restriction in pancreatic β cells. *Cell* 126, 941-954, 2006.

[32] Liszt, G., Ford, E., Kurtev, M., and Guarente, L. Mouse Sir2 homolog SIRT6 is a nuclear ADP-ribosyltransferase. *J. Biol. Chem.* 280, 21313-21320, 2005.

[33] Jeong, J., Juhn, K., Lee, H., Kim, S., Min, B., Lee, K. M., Cho, M. H., Park, G. H., and Lee, K. H. SIRT1 promotes DNA repair activity and deacetylation of Ku70. *Exp. Mol. Med.* 39, 8-13, 2007.

[34] Aylon, Y., and Oren, M. Living with p53, dying of p53. *Cell* 130, 597-600, 2007.

[35] Picard, F., Kurtev, M., Chung, N., Topark-Ngarm, A., Senawong, T., Machado De Oliveira, R., Leid, M., McBurney, M. W. and Guarente, L. Sirt1 promotes fat mobilization in white adipocytes by repressing PPAR-gamma. *Nature* 429, 771-776, 2004.

[36] Li, X., Zhang, S., Blander, G., Tse, J. G., Krieger, M. and Guarente, L. SIRT1 deacetylates and positively regulates the nuclear receptor LXR. *Mol. Cell* 28, 9100-9106, 2007.

[37] Lavu, S., Boss, O., Elliott, P.J., and Lambert, P. D., Sirtuins-novel therapeutic targets to treat age-associated disease, *Nature Reviews* 7, 841-853, 2008.

[38] Li, X., Zhang, S., Blander, G., Tse, J. G., Krieger, M. and Guarente, L. SIRT1 deacetylates and positively regulates the nuclear receptor LXR. *Mol. Cell* 28, 9100-9106, 2007.

[39] Luo, J., Nikolaev, A. Y., Imai, S., Chen, D., Su, F., Shiloh, A., Guarente, L., and Gu, W., Negative control of p53 by Sir2alpha promotes cell survival under stress. *Cell* 107, 137-148, 2001.

[40]   Borra, M.T., Smith, B.C. and Denu, J.M. Mechanism of Human SIRT1 activation by resveratrol. *J. Biol.Chem.* 280, 17187-17195, 2005.

[41]   Dai, J. M., Wang, Z. Y.,Sun, D. C., Lin, R. X., and Wang, S. Q., SIRT1 interacts with p53 and suppresses p53-dependent transcriptional activity. *J. Cell Physiol.* 210, 161-166, 2007.

[42]   Afshar, G., Murnane, J. P., Characterization of human gene with sequence homology to Saccharomyces cerevisaie SIR2. *Gene*, 234, 161-168, 1999.

[43]   Nemoto, S., Fergusson, M. and Finkel, T., SIRT1 functionally interacts with the metabolic regulator and transcriptional coactivator PGC-1. *J. Biol. Chem.* 280, 16456-16460, 2005.

[44]   Yang, Y., Hou, H., Haller, E. M., Nicosia, S. V. and Bai, W. Suppresion of FOXO1 activity by FHL2 through SIRT1-mediated deacetylation. *EMBO J.* 24, 1021-1032, 2005.

[45]   Jing, E., Gesta, S., and Kahn, C. R., SIRT2 regulates adipocyte differentiation through FoxO1 acetylation/deacetylation. *Cell Metab.* 6, 105-114, 2007.

[46]   Wang, F., Nguyen, M., Qin, F. X.-F. and Tong, Q. SIRT2 deacetylates FOXO3a in response to oxidative stress and caloric restriction. *Aging Cell.* 6, 505-514, 2007.

[47]   Lin, S., Defossez, P. A., and Guarante, L. Requirement of NAD and SIR2 for life span extension by calorie restriction in Saccharomyces cerevisiae. *Science,* 289, 2126-2128, 2000.

[48]   Guarente, L., Calorie restriction and SIR2 genes: towards a mechanism. *Mech. Ageing. Dev.* 126, 923-928, 2005.

[49]   Kaebelin, M., Powers, R. W., Steffen, K. K.,Westman, E. A., Hu, D., Dang, N., Kerr, E. O., and Kennedy, B. K., Regulation of yeast replicative life span by TOR and Sch9 in response to nutrients. *Science* 310, 1193-1196, 2005.

[50]   Yamauchi, T., Kamon, J., Minokoshi, Y., Ito, Y., Waki, H., Uchida, S., Yamashita, S., Noda, M., Kita, S., Ueki, K., *et.al* Adiponection stimulates glucose utilization and fatty-acid oxidation by activating AMP-activated protein kinase. *Nat. Med.* 8, 1288-1295, 2002.

[51]   Michan, S., and Sinclair, D., Sirtuins in mammals: insights into their biological function. *Biochem. J.* 404, 1-13, 2007.

[52]   Outerio, T.F., Sirt2 inhibitors rescue α-synuclein-mediated toxicity in models of Parkinson's disease. *Science*, 317, 516-519, 2007.

[53]   Li, Y., Xu, W., McBurney, M. Q and Longo, V.D., SirT1 reducesd signalling and protects neurons. *Cell. Metab.* 8, 38-48, 2008.

[54] Wang, J. A local mechanism mediates NAD-dependent protection of axon degeneration. *J.Cell.Biol*. 170, 349-355, 2005.

[55] Shindler, K.S., Ventura, E., Rex, T.S., Elliot, P and Rostami, A. SIRT1 activiation confers neuroprotection in experimental optic neuritis. *Invest. Opthalmol. Vis. Sci*. 48, 3602-3609, 2007.

[56] Jin, Y.-H., Kim, D.-W., Beak, K.-H., Kang, B. Y., Yeo, C.-Y. and Lee, K.-Y. Sirt2 interacts with 14-3-3 beta/gamma and down-regulates the activity of p53. *Biochem. Biophys. Res. Commun*. 368, 690-695, 2008.

[57] Hallows, W.C., Lee, S. and Denu, J. M. Sirtuins deacetylate and activate mammalian acetyl-CoA synthetases. *Proc. Nat. Acad. Sci. U.S.A*. 103, 10230-10235, 2006.

[58] Schwer, B., Bunkenborg, J., Verdin, R. O., Andersen, J.S. and Verdin, E., Reversible lysine acetylation controls the activity of the mitochondrial enzyme acetyl-CoA synthetase 2. *Proc. Nat. Acad. Sci. U.S.A*. 103, 10224-10229, 2006.

[59] Ahuja, N., Schwer, B., Carobbio, S., Waltregny, D., North, B., Castronovo, V. Maechler, P., and Verdin, E Regulation of insulin secretion by SIRT4, a mitochondrial ADP-ribosyltransferase. *J. Biol. Chem*. 282, 33583-33592, 2007.

[60] Solomon, J.M., Pasupuleti, R., Xu, K., McDonagh, Y., Curtis, R., DiStefani, P. S. and Huber, L. J. Inhibition of SIRT1 catalytic activity increases p53 acetylation but does not alter cell survival following DNA damage. *Mol. Cell. Biol*. 26, 28-38, 2006.

[61] Michishita, E., McCord, R. A., Berber, E., Kioi, M., PadillaNash, H., Damian, M., Cheung, P., Kusumoto, R., Kawahara, T. L., Barrett, J. C., Chang, H. Y., Bohr, V. A., Ried, T., Gozani, O. and Chua, K.F., SIRT6 is a histone H3 lysine 9 deacetylase that modulates telomeric chromatin. *Nature*, 452. 492-496, 2008.

[62] Vakhrusheva, O., Smolka, C., Gajawada, P., Kostin, S.,Boettger, T., Kubin, T., Braun, T., and Bober, E. Sirt7 incerases stress resistance of cardiomyocytes and prevents apoptosis and inflamantory cardiomyopathy in mice. *Circ. Res*., 2008.

[63] Imai, S., Armstrong, C. M., Kaeberlein, M., Guarente, L. Transcriptional silencing and longevity protein Sir2 is an NAD-dependent histone deacetylase. *Nature,* 403, 795-800, 2000.

[64] Grubisha, O. Metabolite of SIR2 Reaction Modulates TRPM2 Ion Channel. *J.Biol.Chem*. 281, 146057-14065, 2006.

[65] Borra, M.T., Conserved Enzymatic Production and biological Effect of O-Acetyl-ADP-ribose by Silent Information Regulator 2-like NAD$^+$-dependent Deacetylases. *J.Biol.Chem*. 277, 12632-12641, 2002.

[66] Lee, S., Tong, L. and Denu, J.M. Quantification of endogenous sirtuin metabolite O-acetyl-ADP-ribose. *Anal.Biochem*. 383, 174-179, 2008.

[67] Buck, S.W., Gallo, C.M., and Smith, S., Diversity in the Sir2 family of protein deacetylases. *J. of Leukocyte Biology*, 75, 939-950, 2004.

[68] Avalos, J. L., Celic, I., Muhammad, S., Cosgrove, M. S., Boeke, J. D., Wolberger, C. Structure of a Sir2 enzyme bound to an acetylated p53 peptide. *Mol. Cell.* 10, 523-535, 2002.

[69] Min, J., Landry, J.,Sternglanz, R., Xu, R. M. Crystal structure of SIR2 homolog NAD complex. *Cell,* 105, 269-279, 2001.

[70] Finnin, M. S., Donigian, J. R., and Pavletich, N. P., Structure of the histone deacetylase SIRT2, *Nature*, 8, 621-625, 2001.

[71] Sanders, B. D., Zhao, K., Slama, J. T., Marmorstein, R. Structural basis for nicotinamide inhibition and base exchange in Sir2 enzymes. *Mol. Cell. 25*, 463-472, 2007.

[72] Landry, J., Sutton A., Tafrov, S. T., Heller, R. C., Stebbins, J., Pillus, L., Sternglanz, R., The silencing protein SIR2 and its homologs are NAD-dependent protein deacetylase. *Proc. Natl. Acad. Sci. USA*, 97, 5807-5811, 2000.

[73] Vaziri, H., Dessain, S.K., Ng Eaton, E., Imai, S.I., Frye, R. A., Pandita, T. K., Guarente, L., Weinberg, R. A., hSIR2 (SIRT1) functions as an NAD-dependent p53 deacetylase. *Cell,* 107, 149-159, 2001.

[74] Koch-Nolte F. K.S., Mueller-Dieckmann C., Weiss M.S. Mammalian ADP-ribosyltransferases and ADP-ribosylhydrolases. *Front Biosci.*13, 6716-6729, 2008.

[75] Bitterman, K.J. et al. Inhibition of Silencing and Accelerated Aging by Nicotinamide, a Putative Negative Regulator of Yeast Sir2 and Human SIRT1. *J. Biol. Chem.* 277, 45099-45107, 2002.

[76] Schmidt, M.T. Coenzyme Specificity of Sir2 Protein Deacetylase. *J.Biol.Chem.* 279, 40122-40129, 2004.

[77] Schemies, J., Uciechowska, U., Sippl, W., Jung, M. NAD$^+$ dependent histone deacetylases (sirtuins) as novel therapeutic target. *Med. Res. Rev.*, 2009.

[78] Milne, J.C., Lambert, P.D., Schenk, S., Carney, D.P., Smith, J.J., Westphal, C.H. Small molecule activators of SIRT1 as therapeutics for the treatment of type 2 diabetes. *Nature,* 450, 712-716, 2007.

[79] Yang, S.R., Chida, A.S., Bauter, M.R., Shafiq, N., Seweryniaak, K., Maggirwar, S.B., Kilty, I., Rahman, I. Cigarette smoke induces proinflammatory cytokine release by activation of NF-kappaB and posttranslational modifications of histone deacetylase in macrophages. *Am.J.Physiol. Lung. Cell Mol.Physiol.* 291, L46-L47, 2006.

[80] Posakony, J., Hirao, M., Stevens, S., Simon, J.A., Bedalov, A. Inhibitors of Sir2: Evaluation of Splitomicin Analogues. J.*Med.Chem.* 47, 2635-2644, 2004.

[81]   Trapp, J., Jochum, A., Meier, R., Saunders, L., Marschall, B., Kunick, C., Adenosine mimetics as inhibitors of NAD (+)- dependent histone deacetylase, from kinase to sirtuin inhibition. *J. Med.Chem.*, 49, 7307-16, 2006

[82]   Tervo, A.J., Kyrylenko, S., Niskanen, P., Salinen, A., Leppanen, J., Nyronen, T.H., Jarvinen, T., Poso, A. An in silico approach to discovering novel inhibitors of human sirtuin type 2. *J.Med.Chem.* 47, 6292-6298, 2004.

[83]   Landry, J., Slama, J.T., Sternglanz R. Role of NAD$^+$ in the deacetylase activity of the SIR2-like proteins. *Biochem. Biophys. Res. Commun.* 278, 685-690, 2000.

[84]   Suzuki, T., Imai, K., Nakagawa, H, Miyata, N. 2-Anilinobenzamides as SIRT inhibitors. *Chem.Med.Chem.* 1, 1059-1062, 2006.

[85]   Bedalov, A., Gatbonton, T., Irvine, W.P., Gottschling, D.E., Simon, J.A., Identification of a small molecule inhibitor of Sir2p. *Proc.Natl.Acad.Sci. USA*, 47, 2635-2644, 2004.

[86]   Grozinger, C.M., Chao, E.D., Blackwell, H.E., Moazed, D., Schreiber, S.L., Identyfication of class of small molecule inhibitors of the sirtuin family of NAD-dependent deacetylases by phenotypic screening. *J.Biol.Chem,* 276, 38837-38843, 2001.

[87]   Mai, A., Massa, S., Lavu, S., Pezzi, R., Simeoni, S., Ragno, R., Mariotti, F.R., Chiani, F., Camilloni, G., Sinclair, D.A. Design, synthesis, and biological evaluation of sirtinol analogues as class III histone protein deacetylase (sirtuin) inhibitors. *J.Med.Chem.* 48, 7789-7795, 2005.

[88]   Medda, F., Russell, R.J., Higgins, M., McCarthy, A.R., Campbell, J., Slawin, A.M., Lane, D.P., Lain, S., Westwood, N.J., Novel cambinol analogs as sirtuin inhibitors: Synthesis, biological evaluation, and rationalization of activity. *J. Med. Chem.,* 52, 2673-2682, 2009.

[89]   Heltweg, B., Trapp, J., Jung, M. In vitro assays for the determination of histone deacetylase activity. *Methods.* 36, 332-337, 2005.

[90]   Napper, A.D., Hixon, J., McDonagh, T., Keavey, K., Pons, J.F., Barker, J., Yau, W.T., Amouzegh, P., Flegg, A., Hamelin, E., Thomas, R. J., Kates, M., Jones, S., Navia, M.A., Saunders, J.O., DiStefano, P.S., Curtis, R., Discovery of indoles as potent and selective inhibitors of the deacetylase SIRT1. *J.Med.Chem*, 48, 8045-8054, 2005.

[91]   Solomon, J.M., Pasupuleti, R., Xu, L., McDonagh, T., Curtis, R., DiStefano, P.S., Huber, L.J. Inhibition of SIRT1 catalytic activity increases p53 acetylation but does not alter cell survival following DNA damage. *Mol.Cell.Biol.* 26, 28-38, 2006.

[92]   Voogd, T.E., Vansterkenburg, E.L, Wilting, J., Janssen, L.H. Recent research on the biological activity of suramin. *Pharmacol. Rev.* 45, 177-203,1993.

[93] Trapp, J., Meier, R., Hongwiset, D., Kassack, M. U., Sippl, W., Jung, M. Structure-activity studies on suramin analogues as inhibitors of NAD^+ -dependent histone deacetylases (sirtuins). *Chem.Med.Chem*. 2, 1419-1431, 2007.

[94] Tervo, A.J., Suuronen, T., Kyrylenko, S., Kuusisto, E., Kiviranta, P.H., Salminen, A., Leppanen, J., Poso A. Discovering inhibitors of human sirtuin type 2: Novel structural scaffolds. *J.Med.Chem.* 49, 7239-7241, 2006.

[95] Kim, D., Nguyen, M.D., Dobbin, M.M., Fischer, A., Sananbenesi, F., Rodgers, J.T., Delalle, I., Baur, J.A., Sui, G., Armour, S.M., Puigserver, P., Sinclair, D.A., Tsai, L.H. SIRT1 deacetylase protacts against neurodegeneration in models for Alzheimer's disease and amyotrophic lateral sclerosis. *EMBO J. 26,* 3169-3179, 2007.

[96] Parker, J.A, Arango, M.,Abderrahmane, S., Lambert, E., Tourette, C., Catoire, H., Neri, C. Resveratrol rescues mutant polyglutamine cytottoxicity in nematode and mammalian neurons. *Nat. Genet.* 37, 349-350, 2005.

[97] Nayagam, V.M., Wang, X., Tan, Y.C., Poulsen, A., Goh, K.C., Ng, T., Wang, H., Song, H.Y., Ni, B., Entzeroth, M., Stunkel, W. SIRT1 modulating compounds from high-throughout screening as anti-inflammatory and insulin-sensitiizing agents. *J.Biomol.Screen*. 11, 959-967, 2006.

[98] Saunders, L.R., Verdin E., Sirtuins: Critical regulators at the crossroads between cancer and aging. *Oncogene*, 26, 5489-5504, 2007.

[99] Lech, A. Molecular Modelling. *Principles and Application*. Prentice Hall, 2001.

[100] Höltje, H.D., Sippl, W., Rognan, D., and Folkers, G. *Molecular Modelling: Basic principles and applications*. Wiley-VCH, 2003.

[101] Blaney, J.M. and Dixon, J.S. A Good Ligand is hard to find: Automatic Docking Methods.*Perspect. Drug Disc. Des.,*15, 301, 1993.

[102] Kuntz, I.D., Structure-Based Strategies for Drug Design and Discovery. *Science,* 257, 1078, 1992.

[103] Oprea, T. I., and Marshall, G. R., Receptor-Based Prediction of Binding Affinities. Perspect. *Drug Discovery Des.,* 35, 1998.

[104] Tame, J.R.H. Scoring Functions: A View from the Bench. *J.Comput.-Aided Mol. Des.,* 13, 99, 1999.

[105] Rarey, M., Kramer, B., Lengauer, T., and Klebe, G. A fast flexible Docking Method using an Incremental Construction Algorithm. *J.Mol.Biol.*, 261, 470, 1996.

[106] Friesner, R.A., Banks, J.L., Murphy, R.B., Halgren, T., Klicic, H., Mainz, D., Repasky, M., Knoll, M., Shelley, M., Perry, J.K., Shaw, D.E., Francis, P and Shenkin, S. Glide: A New Approach for Rapid, Accurate Docking and Scoring. 1. Method and Assessment of Docking Accuracy. *J. Med. Chem.*, 47, 1739–1749, 2004.

[107] Goodsell, D.S., and Olson, A. J. Automated Docking of Substrates to Proteins by Simulated Annealing. Proteins: *Struct. Funct. Genet.* 8, 195, 1990.

[108] Kuntz, I. D., Blaney, J. M., Oatley, S.J., and Langridge, R.L. A Geomtric Approach to Macromolecule-Ligand Interactions. *J. Mol. Biol.,* 161, 269, 1982.

[109] Jones, G., Willett, P., Glen, R.C., and Leach, A.R. Development and Validation of Genetic Algorithm for Flexible Docking. *J. Mol. Biol.,* 161, 267, 1997.

[110] Weiner, S.J., Kollman, P.A., Case, D.A., Singh, U.C., Ghio, C., Alagona, G., Profeta, S., and Weiner, P. A New Force Field for Molecular Mechanical Simulation of Nucleic Acids and Proteins. *J.Am.Chem.Soc.* 106, 765, 1984.

[111] Shoichet, B. K., Leach, A. R., and Kuntz, I. D., Ligand Solvation in Molecular Docking. Proteins: *Struct.Funct.Genet.* 34, 4, 1999.

[112] Böhm, H. LUDI: Rule-Based Automatic Design of New Substituents for Enzyme Inhibitor Leads. *J. Comput.-Aided Mol. Des.,* 6, 593, 1992.

[113] Meng, E.C., Shoichet, B. K., and Kuntz, I .D. Automated Docking with Grid-Based Energy Evaluation. *J. Comput. Chem.* 13, 505, 1992.

[114] Meng, E.C, Kuntz, I. D., Abraham, D. J., and Kellogg, G. E. J. Evaluating Docked Complexes with the HINT Exponential Function and Empirical Atomic Hydrophobicities. *Comput.-Aided Mol. Des.* 8, 299, 1994.

[115] Gschwend, D.A. and Kuntz, I.D. Orientational Sampling and Rigid.Body Minimization in Molecular Docking Revisited- On the Fly Optimization and Degeneracy Removal. *J. Comput.-Aided Mol. Des.,* 10, 123, 1996.

[116] Jones, G., Willett, P., and Glen, R. C. A Genetic Algorithm for Flexible Molecular Overlay and Pharmacophore Elucidation. *Comput.-Aided Mol. Des.,* 9, 532, 1995.

[117] Horton, N., and Lewis, M. Calculation of the Free Energy of Association for Protein Complexes. *Protein Sci.,* 1, 169, 1992.

[118] Böhm, H.J., Prediction of Binding Constants of Protein Ligands-A fast method for the Prioritization of Hits Obtained from De Novo Design or 3D Database Search Programs. *J. Comput.-Aided Mol. Des.,* 12, 309, 1998.

[119] Eldridge, M.D., Murray, C.W., Auton, T. R., Paolini, G. V., and Mee, R.P. Empirical Scoring Functions. The Development of a Fast Empirical Scoring Function to Estimate the Binding Affinity of Lignads in Receptor Complexes. *J. Comput.-Aided Mol. Des.,* 11, 425, 1997.

[120] DeWitte, R.S., and Shakhnovich, E.J. SMoG: de novo Design Method Based on Simple, Fast, and Accurate Free Energy Estimates. *J. Am. Chem. Soc.,* 118, 11733, 1996.

[121] Gohlke, H., Hendlich, M., and Klebe, G. Knowledge-Based Scoring Function to Predict Protein-Ligand Interactions. *J. Mol. Biol.,* 295, 337, 2000.

[122] Jernigan, R. L., and Bahar, I. Structure-Derived Potentials and Protein Simulations. *Curr. Opin. Struct. Biol.,* 6, 195, 1996.

[123] Mitchell, J.B.O., Laskowski, R.A., Alex, A., and Thornton, J.M. BLEEP.Potential of Mean Force Describing Protein-Ligand Interactions. *J. Comput.Chem.,* 20, 1165, 1999.

[124] Muegge, I., and Martin, Y.C. A General and Fast Scoring Function for Protein-Ligand Interactions: A Simplified Potential Approach. *J. Med.Chem.,* 42, 791, 1999.

[125] Verkhivker, G., Appelt, K., Freer, S.T., and Villafranca, J. E. Empirical Free Energy Calculations of Ligand-Protein Crystallographic Complexes. *Protein Eng.,* 8, 677, 1995.

[126] Wallqvist, A., Jernigan, R.L., and Covell, D.G., A Preference-Based Free Energy Parametrization of Enzyme-Inhibitor Binding. Application to HIV-1-Protease Inhibitor Design. *Protein Sci.,* 4, 1881, 1995.

[127] Wallqvist, A., and Covell, D.G., Docking Enzyme-Inhibitor Complexes Using a Preference-Based Drug Design. *Proteins: Struct. Funct. Genet.* 25, 403, 1996.

[128] Dixon, J.S. Evaluation of the CASP2 Docking Section. *Proteins: Struct. Funct. Genet. Suppl.,* 1, 198, 1997.

[129] Goodford, P.J. A computational procedure for determining energetically favourable binding sites on biologically important macromolecules. *J.Med.Chem.* 28, 849-857, 1985.

[130] Jones, J.E. On the determination of molecular fields. II. From the equation of state of a gas. *Proceedings of the Royal Soc. of London*, 106A, 463-467, 1924.

[131] Wade, R.C. Molecular interaction fields, in 3D QSAR in Drug Design-Theory Methods and Applications. *ESCOM Science Pub*. 486-505, 1993.

[132] Wade, R.C, Clark, K.J., and Goodford, P.J. Further development of hydrogen-bond functions for use in determining energetically favourable binding sites on molecules of known structure. *J.Med.Chem*. 36, 140-147, 1993.

[133] Sippl, W., Contreras, J.M., Parrot, I. Structure-based 3D QSAR and design of novel acetylcholinesterase inhibitors. *J. Comput.-Aided Mol. Des.,* 15, 395-410, 2001.

[134] Wade, R.C. The use of molecular graphics in the design of anti-influenza agents. *Brit.J. of Pharm*, 95,588, 1988.

[135] Jendretzki, U.K., Elz, S., and Höltje, H.D. Computer aided molecular analysis of 5-HT2A agonists. *Pharma. and Pharmac. Letters*.3, 260-263, 1994.

[136] Walters, W.P. Virtual Screening-an overview. *Drug Discov. Today*, 3, 160-178, 1998.

[137] Waszkowycz, B. et.al. Large-scale virtual screening for discovery leads in postgenomic era. *IBM Systems J.* 40, 360-376, 2001.

[138] Miller, M.A. Chemical databases techniques in drug discovery. *Nat. Rev. Drug Discov.* 1, 220-227, 2002.

[139] Bajorath, J. Integration of virtual and high-throughput screening. *Nat. Rev. Drug Discov.* 1, 882-894, 2002.

[140] Sheridan, R.P., Rusinko, A., Nilakantan, R. And Vekataraghavan, R., Searching for pharmacophores in large coordinate data bases and its use in drug design. *Proc. Natl.Acad.Sci.* USA, 86, 8156-8159, 1989.

[141] Hopfinger, A. J., Reaka, A., Venkatarangan, P., Duca, J.S., and Wang, S. Construction of virtual high throughput screen by 4d-QSAR analysis: application to a combinatorial library of glucose inhibitors of glycogen phoshphorylase b. *J. Chem. Inf. Comput. Sci.* 39, 1151-1160, 1999.

[142] Wolber, G. And Langer, T. Ligandscout: 3-pharmacophore derived from protein boind ligands and theis use as virtual screening filters. *J. Chem. Inf. Model.* 45, 160-169, 2005.

[143] Schapira, M., Raaka, B., Samuels, H.H., and Abygyan, R. *BMC Struct. Biol.* 1, 2001.

[144] Schapira, M., Abagyan, R., and Totrov, M. Nuclear hormone receptor targeted virtual screening. *J. Med. Chem.* 46, 3045-3059, 2003.

[145] Grüneberg, S., Wendt, B. and Klebe, G. Angew. *Chem. Int. Ed.* 40, 389-393, 2001.

[146] Filikov, A.V., Mohan, V., Vickers, T.A., Griffey, R. H. Cook, P., Abagyan, R.A., and James, T.L. Identification of ligands for RNA targets via structure-based virtual screening: HIV-1 TAR. *J. Comp. Aided Mol. Des.*, 14, 593-610, 2000.

[147] Lipinski, C.A., Lombardo, F., Dominy, B. W., Feeney, P.J. Experimental and computational approaches to estimate solubility and permeability in drug discovery and development settings. *Adv. Drug Deliv. Rev.*, 23, 3-26, 1997.

[148] Alder, B.J. and Wainwright, T. E. Phase transition for a hard sphere system, *J.Chem.Phys.* 27, 1208, 1957.

[149] Kassell, B., Laskowski, M. The basic trypsin inhibitor of bovine pancreas. V. The disulfide linkages. *Biochem. Biophys. Res. Commun.* 20, 463–8, 1965.

[150] Case, D.A., Pearlamn, D.,A., Caldwell, J.W., Cheetham III, T.E., Wang, J., Ross, W.S., Simmerling, C.L., Darden, T.A., Merz, K. M., Stanton, R.V., Cheng, A.L., Vincent, J.J., Gohlke, H., Massova, I., Weiner, P.K., and Kollamn, P.A. AMBER 7, *University of California, San Fransisco*, 2002.

[151] Lindhl, E., Hess, B., and van der Spoel, D. GROMACS 3.0: A package for molecular simulation and trajectory analysis. *J.Mol.Med*. 7, 306-317, 2001.

[152] Brooks, B.R., Bruccoleri, R.E., Olafson, B.D., States, D.J., Swaminathan, S., and Karlpus, M. CHARMM: A program for macromolecular energy minimization and dynamics calculations. J.Comp.Chem. 4, 187-217, 1983.

[153] Cornell, W.D., Cieplak, P., Bayly, C. I., Gould, I. R., Merz, Jr., K.M., Ferguson, D. M., Spellmeyer, D. C., Fox, T., Caldwell, J. W, and Kollman, P.A. A Second Generation Force Field for the Simulation of Proteins, Nucleic Acids, and Organic Molecules. *J. Am. Chem. Soc*., 117, 5179-5197, 1995.

[154] Karplus, M., and McCammon, A. Molecular Dynamics Simulations of Biomolecules. *Nature*, 9 646-652, 2002.

[155] Beveridge, D.L. and DiCapua, F.M., Free Energy Via Molecular Simulation: Applications to Chemical and Biomolecular Systems, *Annu. Rev. Biophys*., 18 431-492,1989.

[156] Brooks, C.L. and Case, D.A. Simulations of Peptide Conformational Dynamics and Thermodynamics, *Chem. Rev*. 93: 2487-2502, 1993.

[157] Kollman, P., Free Energy Calculations: Applications to Chemical and Biochemical Phenomena, Chem. Rev. 93: 2395-2417, 1993.

[158] Gohlke, H., Klebe, G. Approaches to the description and prediction of the binding affinity of small –molecule ligands to macromolecular receptors. *Angew.Chem., Int. Ed*., 41, 2644-2676, 2002.

[159] Wang, J., Dixon, R., Kollman, P.A. Ranking ligand binding affinities with a vidin: A molecular dynamics-based interaction energy study. *Proteins, Struct. Funct.,* Genet., 34, 69-81, 1999.

[160] Kollman, P.A., Massova, I., Reyes, C., Kuhn, B., Huo, S., Chong, L., Lee, M., Lee, T., Duan, Y., Wang, W., Donini, O., Cieplak, P., Srinivasan, J., Case, D. A., Cheatham, T. E. Calculating structures and free energies of complex molecules: combining molecular mechanics and continuum models. Acc. Chem. Res., 33, 889-897, 2000.

[161] Hansson, T., Marelius, J., Aqvist, J., Ligand binding affinity prediction by linear interaction energy mehods. *J. Comput.-Aided. Mol. Des*., 12, 27-35, 1998.

[162] Srinivasan, J., Cheatham, T. E., Cieplak, P., Kollman, P. A. and Case, D. A. Continuum solvent studies of the stability of DNA, RNA, and phosphoramidate-DNA helices *J. Am. Chem. Soc*. 120, 9401-9409, 1998.

[163] Kuhn, B., Kollman, P.A. Binding of diverse set of ligands to avidin and streptavidin: an accurate quantitative prediction of their relative affinities by a combination of molecular mechanics and continuum solvent models. *J.Med.Chem*. 43, 3786-3791, 2000.

[164] Donini, O. A. Kollman, P. A., Calculation and prediction of binding free energies for the matrix metalloproteinases. *J.Med. Chem*. 43, 4180-4188, 2000.

[165] Wang, J., Morin, P., Wang, W., Kollman, P.A. Use of MM-PBSA in reproducing the binding free energies to HIV-1 RT of TIBO derivatives and predicting the binding mode to HIV-1 RT of efavirenz by docking and MM-PBSA- *J. Am. Chem. Soc*. 123, 5221-5230, 2001.

[166] Pearlman, D. A., Evaluating the Molecular Mechanics Poisson−Boltzmann Surface Area Free Energy Method Using a Congeneric Series of Ligands to p38 MAP Kinase., *J. Med. Chem.*, 48,7796–7807, 2005.

[167] Langen, J. Fritzemeier, K.H., Diekmann, S., Hillisch, A., Molecular Basis of the Interaction Specificity between the Human Glucocorticoid Receptor and Its Endogenous Steroid Ligand Cortisol. *Chem.Bio.Chem.,*6, 1110-1118, 2005.

[168] Carlsson, J., Boukharta, L., and Aqvist Johan. Combining Docking, Molekular Dynamics and Linear Interaction Energy Method to Predict Binding Modes and Affinities for Non-nucleoside Inhibitors to HIV-1 Reverse Transcriptase. *J. Med. Chem.,* 51, 2648-2656, 2008.

[169] Deborah, K., Hertzog, J., and Jorgensen, W.L. Binding Affinities for Sulfonamide Inhibitors with Human Thrombin Using Monte Carlo Simulations with a Linear Response Method. *J. Med. Chem.,* 40, 1539-1550, 1997.

[170] Lipzig, M.M, Laak, A. M, Jongejan, A., Vermeulen, N.P., Wamelink, M., Geerke, D., Meerman, J.H. Prediction of ligand binding affinity and orientation of xenoestrogens to the estrogen receptor by molecular dynamics simulations and the linear interaction energy method. *J Med Chem*. 12, 1018-30, 2004.

[171] Ljungberga, K., Mareliusa, J., Musilb, D., Svenssonc, P., and Johan Åqvist. Computational modelling of inhibitor binding to human thrombin. *Eu. J. of Pharma. Sci.*, 12, 441-446, 2001.

[172] Paulsen, M.D., Ornstein, R.L., MD, Binding free energy calculations for P450cam-substrate complexes. *Protein Eng.*, 9, 567–571, 1996.

[173] Luzhkov, V. B., Nilsson, J., Århem, J., and Åqvist, J., Computational modelling of the open-state K (v) 1.5 ion channel block by bupivacaine, *Biochim. Biophys. Acta* .1652, 35–51, 2003.

[174] Chang, J.H., Kim, H. C., Hwang, K.Y., Lee, J.W., Jackson, S. P., Bell, S.D., Cho, Y. Structural basis for the NAD-dependent deacetylase mechanism of Sir2. *J. Biol. Chem*. 277, 34489−34498, 2002.

[175] Zhao, K., Chai, X., Marmorstein, R., Structure of the yeast Hst2 histone deactylase in ternary complex with 2'-O-acetyl ADP ribose and histone peptide. *Structure*, 11, 1403-1411, 2003.

[176] Avalos, J. L. Celic, I. Muhammad, S. Cosgrove, M. S. Boeke, J. D. Wolberger, C. Structure of a Sir2 enzyme bound to an acetylated p53 peptide. *Mol. Cell.*,10, 523−535, 2002.

[177] Finni, M. S., Donigian, J. R., Paveltich, N.P., Structure of the histone deacetylase SIRT2. Nat. Struct. Biol., 8, 621, 2001.

[178] Tame, J. R. Scoring functions-The first 100 years. *J. Comput.-Aided. Mol. Des*. 19, 445-451, 2005.

[179] Neugebauer, R., Uciechowska, U., Meier, R., Hennig, H., Valkov, V., Verdin, E., Sippl, W. and Jung, M. Structure-Activity Studies on Splitomicin Derivatives as Sirtuin Inhibitors and Computational Prediction of Binding Mode. *J. Med. Chem.,* 51, 1203-1213, 2008.

[180] Molecular Operating Enviroment (MOE) 2006.8. Chemical Computing Group Inc., Montreal, Quebec, Canada, 2006.

[181] Omega, OpenEye Scientific Software; Santa Fe, NM, http://www.eyesopen.com.

[182] Sharp, K. A., Nicholls, A., Friedman, R. and Honig, B. Extracting hydrophobic free energies from experimental data: relationship to protein folding and theoretical models. *Biochem.* 30, 9686− 9697, 1991.

[183] Lovmar, M., Tenson, T., Ehrenberg, M. Kinetics of macrolide action to josamycin an erythromycin cases. *J. Biol. Chem.,* 279, 53506-53515, 2004.

[184] Otyepka, M., Kriz, Z., Koca, J., Dynamics and binding modes of free cdk2 and its two complexes with inhibitors studied by computer simulations. *J. Biol.Struct. Dyn.,* 20, 141-154, 2002.

[185] Yam, W. K., and Wahab, H.A. Molecular insights into 14-Membered Macrolides using MM-PBSA method. *J. Chem. Inf. Model.* 49, 1558-1567, 2009.

[186] Adekoya, O. A., Willassed, N.P., Sylte, I. Molecular insight into pseudolysin inhibition using the MM-PBSA and LIE methods. *J. Struct. Biol.* 153, 129-144, 2006.

[187] Lamb, M.L., Tirado-Rives, J., and Jorgensen, W. L. Estimation of the binding affinities of FKBP12 inhibitors using linear response method. *Bioorg. Med. Chem.* 7, 851, 1999.

[188] Hertzog, D.K., and Jorgensen, W.L. Binding affinities for sulfonamide inhibitors with human thrombin using Monte-Carlo simulations with a linear response method. *J. Med. Chem*. 40, 1539, 1997.

[189] Singh, P., Mhaka, A., Christensen, B., Jeffrey, J., Denmeade, S., and John T. Isaacs. Applying Linear Interaction Energy Method for Rational Design of Noncompetitive Allosteric Inhibitors of the Sarco- and Endoplasmic Reticulum Calcium-ATPase. *J. Med. Chem*. 48, 3005−3014, 2005.

[190] Wang, J. Dixon, R., and Kollman, P. A. Ranking ligand binding affinities with avidin: A molecular dynamics-based interaction energy study. *Proteins*, 34, 1999.

[191] Pearlman, D.A. and Charifson, P.S. Are Free Energy Calculations Useful in Practice? A Comparison with Rapid Scoring Functions for the p38 MAP Kinase Protein System. *J. Med. Chem*. 44, 3417–3423, 2001.

[192] Walker, R.C, de Souza, M.M., Mercer, I.P., Gould, I.R., Klug, D.R., Large and Fast Relaxations inside a Protein: Calculation and Measurement of Reorganization Energies in Alcohol Dehydrogenase. *J. Phys. Chem. B.*, 106(44), 11658-11665, 2002.

[193] Pavelites, J.J., Gao, J.L., Bash, P.A., Mackerell, A.D., Thermodynamic Insights into the Dynamic Switching of a Cyclodextrin in a Bistable Molecular Shuttle *J. Compt. Chem*. 18, 221, 1997.

[194] Wang, J., Wolf, J. W., Caldwell, P.A., Kollman, D. A. Case Development and testing of general amber force fields. *J. Comput. Chem*. 25, 1157-1174, 1999.

[195] Wang, J., Wang, W., Kollman, P. A., D. A. Case. Automatic atom type and bond type perception in molecular mechanical calculations. *J. Mol. Graph. Model.* 25, 247, 2006.

[196] Pang, Y. P., Novel zinc protein molecular dynamics simulations: Steps toward antiangiogenesis for canser treatment. *J. Mol. Model.* 5, 196-202, 1999.

[197] Pang, Y. P., Xu, K., Yazal, E., Prendergast, F. G., Successful molecular dynamics simulations of the zinc-bound farnesyltransferase using the cationic dummy atom approach. *Protein Sci.* 9, 1857-1865, 2000.

[198] http://mayoresearch.mayo.edu/mayo/research/camdl/zinc_protein.cfm

[199] Pastor, R. W., Brooks, B. R., Szabo, A. An anaylsis of the accuracy of Langevin and molecular dynamics algorithms. *Mol. Phys.* 65, 1409-1419, 1988.

[200] Darden, T., York, D., Pedersen, L., L. Particle mesh Ewald: an N log(N) method for Ewald sums. *J.Chem.Phys.* 98, 10089-10092, 1993.

[201] Hornak, V., Abel, R., Okur, A, Strockbine, A., Roitberg, C. Simmerling. Comparison of multiple Amber force fields and development of improved protein backbone parameters. *Proteins* 65, 712-725, 2006.

127

Appendix

Ac	acetylated
AD	Alzheimer's diseases
BPTI	bovine pancreatic trypsin inhibitor
BFE	binding free energy
CaDA	cationic dummy atom
CAMD	computer assisted molecular design
ele	electrostatic
et al.	et altera
FEP	free energy perturbation
GOLD	Genetic Optimisation for Ligand Docking
G_{el}	electrostatic contributions
G_{nonel}	non-electrostatic (hydrophobic) contributions
G	free energy of binding
G_{PBSA}	contribution to the solvation free energy
H	enthalpy of binding
HAT	Histone-Acetyltransferase
HDAC	Hisone-Deacetylase
HIV	Human immunode_ciency virus
IC_{50}	half maximal inhibitory concentration
LIE	Linear Interaction Energy
LRA	linear response approximation
MC	Monte Carlo
MD	molecular dynamics
MM	molecular mechanics
MM-GBSA	Molecular Mechanics-Generalized Born Surface Area
MM-PBSA	Molecular Mechanics Poisson-Boltzmann Surface Area
PD	Parkinson's diseases

PDB	Protein Data Bank
PME	Partial Mesh Ewald
RMSD	root mean square deviation [nm]
RMSE	root mean square of error
r^2	correlation coefficient
S	entropy of binding
SA	Surface Area
SSB	single-structure-based
TI	thermodynamic integration
vdW	van der Waals
VS	Virtual Screening
q$^2_{LOO}$	leave one out term
QSAR	quantitative structure-activity relationship
3D	three-dimensional

List of Publications

I. T. Pesnot, J. Kempter, J. Schemies, G. Pergolizzi, U. Uciechowska, W. Sippl, M. Jung, and G. K. Wagner.
Two-Step Synthesis of Novel, Bioactive Derivatives of the Ubiquitous Cofactor NAD^+.
J. Med. Chem. 2010, accepted.

II. M. Lawson, U. Uciechowska, J. Schemies, T. Rumpf, M. Jung and W. Sippl.
Inhibitors to understand molecular mechanisms of NAD^+-dependent deacetylases (sirtuins).
Biochim. Biophys. Acta. 2010, Jun 23. [Epub ahead of print]

III. K. Huber, J. Schemies, U. Uciechowska, J. M. Wagner, T. Rumpf, F. Lewrick, R. Süss, W. Sippl, M. Jung and F. Bracher.
Novel 3‑Arylidene- indolin- 2‑ones as inhibitors of NAD^+-dependent histone deacetylases (sirtuins).
J. Med. Chem. 2010, 53,1383- 1386.

IV. J. Schemies, U. Uciechowska, W. Sippl and M. Jung.
NAD^+ dependent histone deacetylases (sirtuins) as novel therapeutic target.
Med. Res. Rev., 2009, available online.

V. U. Uciechowska, J. Schemies, R. Neugebauer, E. Huda, M. Schmitt, R. Meier, E. Verdin, M. Jung, W. Sippl.
Thiobarbiturates as Sirtuin Inhibitors: Virtual Screening, Free Energy Calculations and Biological Testing.
Chem. Med. Chem., 2008, 3(12), 1965- 1976.

VI. R. C. Neugebauer, U. Uciechowska, R. Meier, H. Hruby, V. Valkov, E. Verdin, W. Sippl, and M. Jung.
Structure activity studies on splitomicin derivatives as sirtuin inhibitors and computational prediction of binding mode.
J. Med. Chem. 51, 1203- 1213, 20.

Curriculum Vitae

Personal Information

Name	Urszula Sylwia Uciechowska
Date of birth	October 12th 1981
Place of birth	Kielce, Poland

Education

2006-2010	PhD-Student of Prof. Dr. W. Sippl Institute of Pharmaceutical Chemistry Martin-Luther-Univeristy Halle-Wittenberg
08/2005-05/2006	Contract Research Assistant Molecular Networks, GmbH. Naegelsbachstrasse 25, 91052 Erlangen, Germany. Project: Analysis of the Cambridge Structural Database (CSD) and Macromolecular Structural Database (MSD) to validate derived torsion angle libraries in the CORINA and ROTATE software packages.
2004-2005	Master of Science thesis in the group of Prof. T.Clark Computer Chemie Centrum, Univeristy Erlangen-Nurember, Germany Project: Molecular Dynamics and Locally Enhanced Sampling Analysis and Conformationa Clustering of TrxA Peptide Fusion Constructs.
2000-2005	Study of Chemistry, Department of Chemistry, Wroclaw University of Technology, Poland.

Erklärung

Hiermit erkläre ich, dass ich die vorliegende Dissertationsschrift selbstständig und ohne fremde Hilfe angefertigt, keine anderen als die angegebenen Quellen und Hilfsmittel benutzt und die aus ihnen wörtlich oder inhaltlich entnommenen Stellen als solche kenntlich gemacht habe.
Die Arbeit wurde ausschließlich der Mathematisch-Naturwissenschaftlichen Fakultät der Martin-Luther-Universität Halle-Wittenberg vorgelegt und an keiner anderen Universität oder Hochschule weder im In- und Ausland zur Erlangung des Doktorgrades eingereicht.

Halle (Saale), den 13.12.2010